AGU PUBLICATIONS

Geochemistry, Geophysics, Geosystems

RESEARCH ARTICLE
10.1002/2014GC005283

Key Points:
- Arabia's present-day topography has been generated by Neogene mantle convection
- Longitudinal river profiles constrain the spatial and temporal uplift history
- This uplift history is corroborated by multiple independent constraints

Correspondence to:
J. W. P. Wilson,
jwpw2@cam.ac.uk

Citation:
Wilson, J. W. P., G. G. Roberts, M. J. Hoggard, and N. J. White (2014), Cenozoic epeirogeny of the Arabian Peninsula from drainage modeling, *Geochem. Geophys. Geosyst.*, *15*, 3723–3761, doi:10.1002/2014GC005283.

Received 5 FEB 2014
Accepted 19 AUG 2014
Accepted article online 27 AUG 2014
Published online 1 OCT 2014

Cenozoic epeirogeny of the Arabian Peninsula from drainage modeling

J. W. P. Wilson[1], G. G. Roberts[1,2], M. J. Hoggard[1], and N. J. White[1]

[1]Bullard Laboratories, Department of Earth Sciences, University of Cambridge, Cambridge, UK, [2]Now at Department of Earth Science and Engineering, Imperial College, London, UK

Abstract It is generally accepted that the Arabian Peninsula has been uplifted by subcrustal processes. Positive residual depth anomalies from oceanic crust in the Red Sea and in the Gulf of Aden suggest that a region surrounding this peninsula is dynamically supported. Admittance calculations, surface wave tomography studies, and receiver function analyses all imply that regional topography is generated and maintained by some combination of mantle convective circulation and lithospheric thickness changes. Despite these significant advances, the spatial and temporal uplift rate history of the Arabian Peninsula is not well known. Here we show that a regional uplift rate history can be obtained by jointly inverting 225 longitudinal river profiles that drain this peninsula. Our strategy assumes that shapes of individual river profiles are controlled by uplift rate history and moderated by erosional processes. We used local measurements of incision rate to calibrate the relevant erosional parameters. In our inverse algorithm, uplift rate is permitted to vary smoothly as a function of space and time but upstream drainage area remains invariant. We also assume that knickzone migration is not lithologically controlled. Implications of these important assumptions have been investigated. Our results suggest that the Arabian Peninsula underwent two phases of asymmetric uplift during the last 20–30 Ma at rates of 0.05–0.1 mm a^{-1}. The southwestern flank of the peninsula has been uplifted by 1.5–2.5 km. Regional stratigraphic constraints, the age and composition of volcanism, paleosol formation, incised peneplains, emergent marine terraces, and thermochronometric measurements corroborate our calculated patterns of uplift. Progressive development of three domal swells along the western margin of the peninsula is consistent with localized upwelling of hot asthenospheric mantle.

1. Introduction

The geomorphologic expression of the Afro-Arabian region is reminiscent of the well-known "basin and swell" morphology of Africa, which is usually accepted to be dynamically maintained by subcrustal processes (Figures 1 and 2) [*Holmes*, 1944; *Burke*, 1996; *Burke and Gunnell*, 2008]. This elongated region is situated at the northern termination of the East African system of domes and rifts. Its physiography and igneous history suggest that domal epeirogenic uplift is superimposed upon a rift architecture [*Almond*, 1986]. High topography along the western flank of the Arabian Peninsula is often referred to as the Western Arabian swell, although the pattern of volcanism and drainage suggests that this swell consists of three separate domes (Figure 1). The uplift history of these domes contains indirect information about the temporal and spatial evolution of subplate convective circulation.

Arabian stratigraphy suggests that, since cratonization, the Arabian shield had low relief until Late Mesozoic times [*Şengör*, 2001]. During Late Mesozoic and Early Cenozoic times, marine sedimentary rocks were deposited along the fringes of this shield (e.g., Usfan Formation) [*Brown*, 1970]. Thick lateritic weathering profiles, indicative of *in situ* weathering of basement, occur sporadically across the shield. These profiles are capped by basaltic flows as old as 30 Ma [*Brown*, 1970; *Brown et al*., 1989]. Regional uplift of these marine deposits and weathering profiles implies that the Western Arabian swell developed in Neogene times. The temporal variation of uplift within this $\sim$ 30 Ma period can be constrained in different ways. First, thermochronometric measurements are used to determine rates of denudation at spot locations [*Kohn and Eyal*, 1981; *Bohannon et al*., 1989; *Menzies et al*., 1997; *Feinstein et al*., 2013]. At present, these spot measurements are sparse and dominated by localities in Yemen. However, they consistently indicate two phases of cooling since Middle Eocene times with a post-25 Ma onset of rapid cooling [*Bohannon et al*., 1989; *Menzies et al*.,

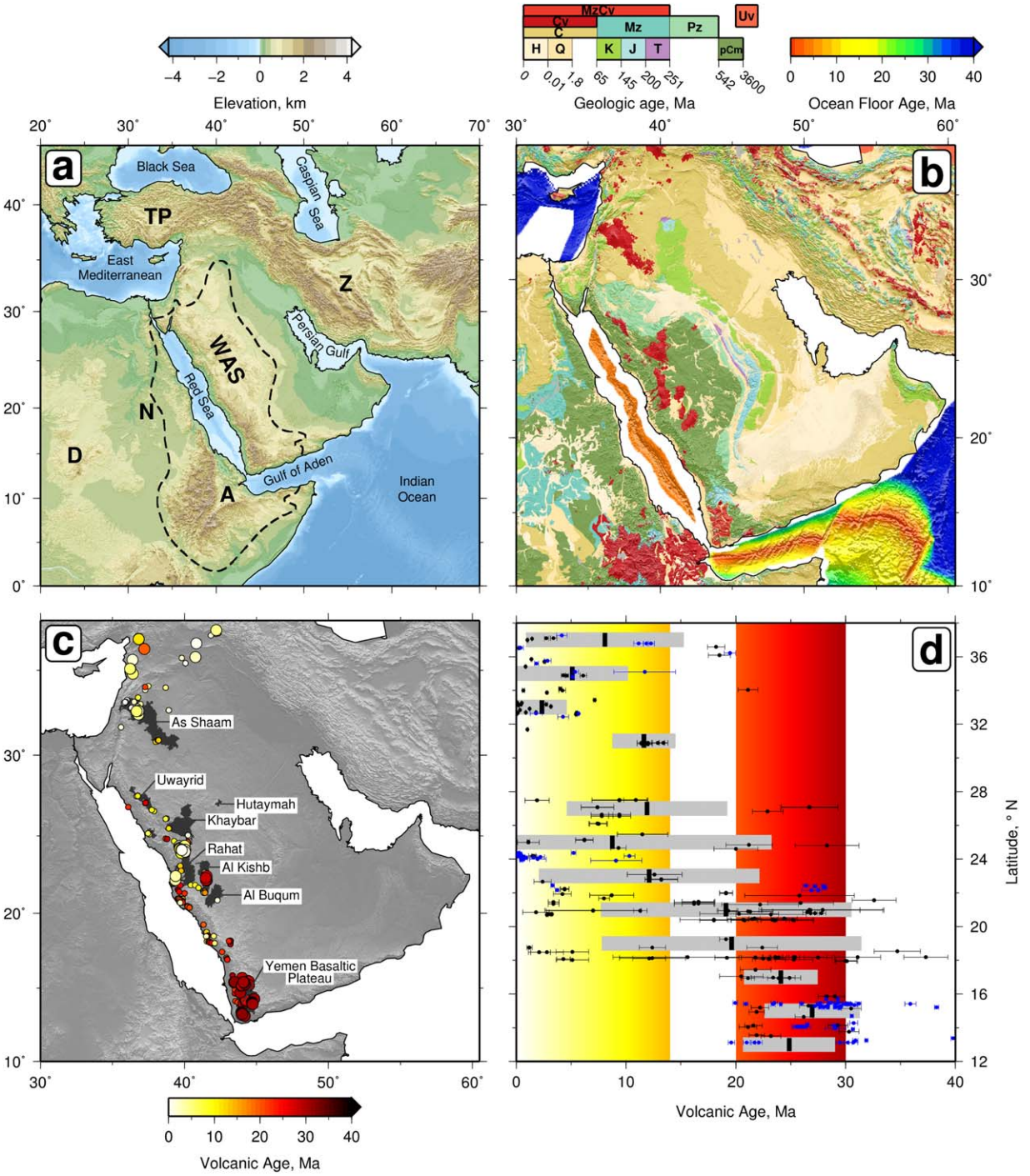

Figure 1. (a) Topographic map centered on Arabian Peninsula (from SRTM30_PLUS model) [*Becker*, 2009]. WAS = Western Arabian swell; TP = Turkish Plateau; Z = Zagros Mountains; N = Nubian dome; D = Dafur dome; A = Afar dome. Dashed line = outline of Afro-Arabian dome [*Camp and Roobol*, 1992]. (b) Geology of Arabian Peninsula [*Pollastro et al.*, 1998; *Muller et al.*, 2008]. (c) Spatial and temporal distribution of magmatism. Large circles = 113 $^{40}Ar/^{39}Ar$ ages [*Hussain and Bakor*, 1989; *Sebai et al.*, 1991; *Baker et al.*, 1996; *Coulié et al.*, 2003; *Riisager et al.*, 2005; *Krienitz et al.*, 2009; *Moufti et al.*, 2013]; small circles = 204 less reliable K-Ar ages [*Civetta et al.*, 1978; *Coleman et al.*, 1983; *Pallister*, 1987; *Capaldi et al.*, 1987; *Chisea et al.*, 1988; *Camp and Roobol*, 1989; *Brown et al.*, 1989; *du Bray et al.*, 1991; *Trifonov et al.*, 2010; *Al-Kwatil et al.*, 2012]. (d) Age of magmatism as function of latitude. Blue circles with error bars = 113 $^{40}Ar/^{39}Ar$ ages; black circles with error bars = 204 K-Ar ages; black/gray bars = mean ages in 2° bins with one σ; yellow/red strips = younger/older magmatic series [*Camp and Roobol*, 1992].

1997; *Pik et al.*, 2013]. Second, the geomorphology of an uplifted landscape provides qualitative indications of the temporal pattern of uplift. For example, youthful incision of the Euphrates and of rivers that drain Harrat Rahat emphasize the importance of Neogene epeirogenic uplift [*Demir et al.*, 2008].

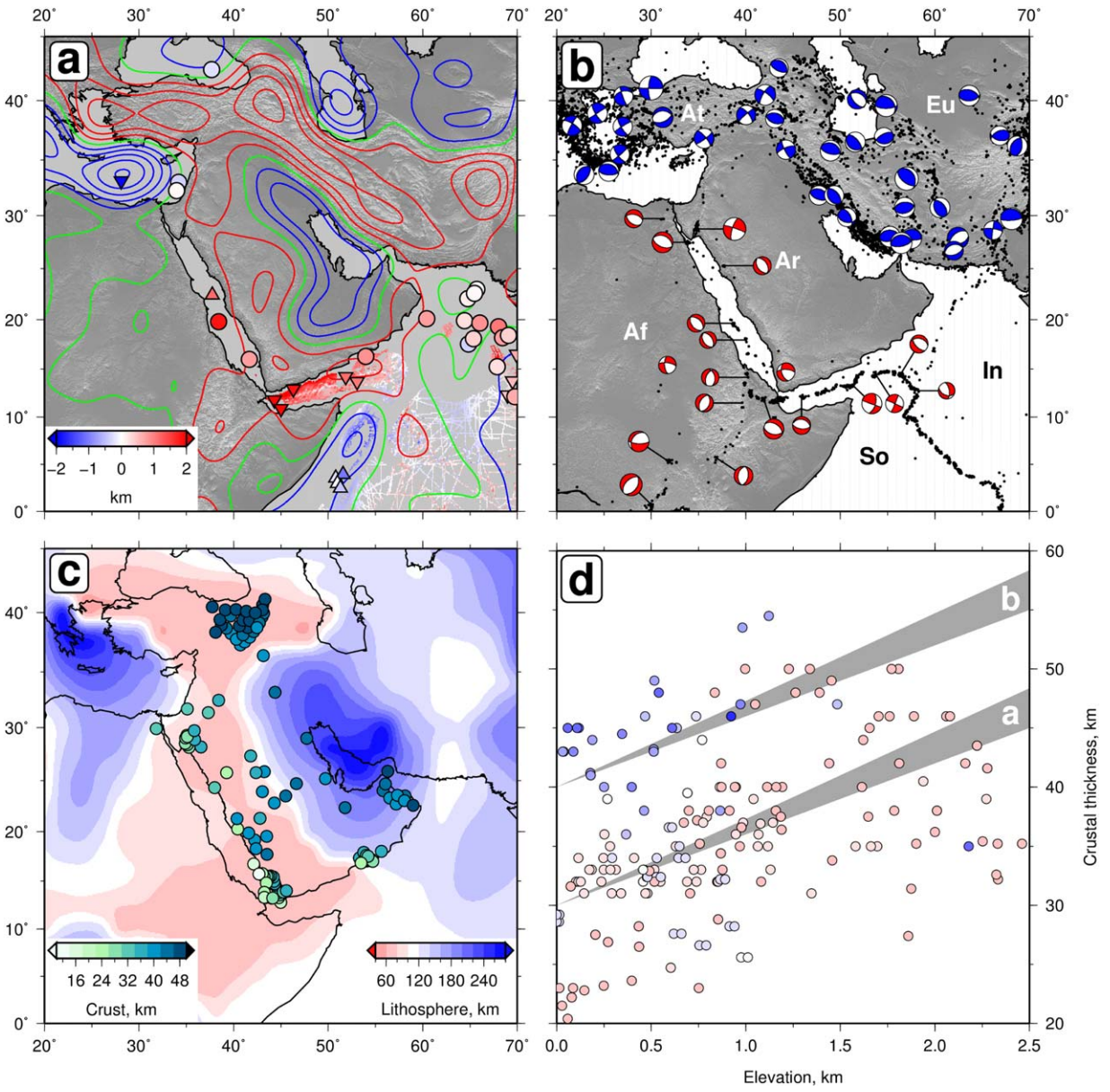

Figure 2. (a) Long wavelength (800–2500 km) free-air gravity map [*Tapley*, 2005]. Red = positive anomaly; blue = negative anomaly; green = zero value contour; contour interval = 15 mGal. Circles and upward/downward triangles = residual topographic estimates and lower/upper bounds obtained by analyzing 21 seismic reflection profiles and 3 wide-angle seismic refraction surveys [*Laughton and Tramontini*, 1969; *Izzeldin*, 1987; *Barton et al.*, 1990; *Egloff et al.*, 1991; *Ben-Avraham et al.*, 2002; *Netzeband et al.*, 2006; *Lucazeau et al.*, 2008; *Leroy et al.*, 2010; *Watremez et al.*, 2011; *Ligi et al.*, 2012]. Filigree of lines = residual topography calculated from ship-track bathymetry [*Winterbourne et al.*, 2014]. (b) Earthquake seismicity for 1964–1995 from EHB catalogue [*Engdahl et al.*, 1998]. Solid circles = earthquakes of magnitude $\geq$ 4.7; blue focal mechanisms from Centroid Moment Tensor catalogue (www.globalcmt.org); red focal mechanisms are constrained by body waveform modeling [*Craig et al.*, 2011]. Ar = Arabian Plate; Af = African Plate; So = Somalian Plate; In = Indian Plate; At = Anatolian Plate; Eu = Eurasian Plate. (c) Lithospheric thickness variation determined from surface wave tomographic model [*Fishwick*, 2010]. Circles = crustal thicknesses from receiver function analyses [*Zor et al.*, 2003; *Al-Damegh et al.*, 2005; *Hansen et al.*, 2007b; *Tiberi et al.*, 2007; *Gök et al.*, 2008; *Al-Hashmi et al.*, 2011; *Ahmed et al.*, 2013]. (d) Crustal and lithospheric thicknesses plotted as function of elevation. Gray bands = expected isostatic relationship between crustal thickness and elevation obtained by equalizing lithostatic pressure at base of 30 km (Figure 2a) and 40 km (Figure 2b) thick crust. Width of band reflects range of crustal density (i.e., 2.8 ± 0.05 Mg m^{-1}) with lithospheric mantle density is 3.3 Mg m^{-1}.

Here our principal objective is to show that the pattern of longitudinal river profiles which drain the Arabian Peninsula can be used to estimate temporal and spatial patterns of uplift. Key erosional parameters are calibrated using independent observations. We suggest that drainage patterns of the Arabian Peninsula contain important, albeit indirect, clues about uplift history that can be tested in different ways (e.g., incision rate records, thermochronometric measurements, magmatic histories, stratigraphic constraints).

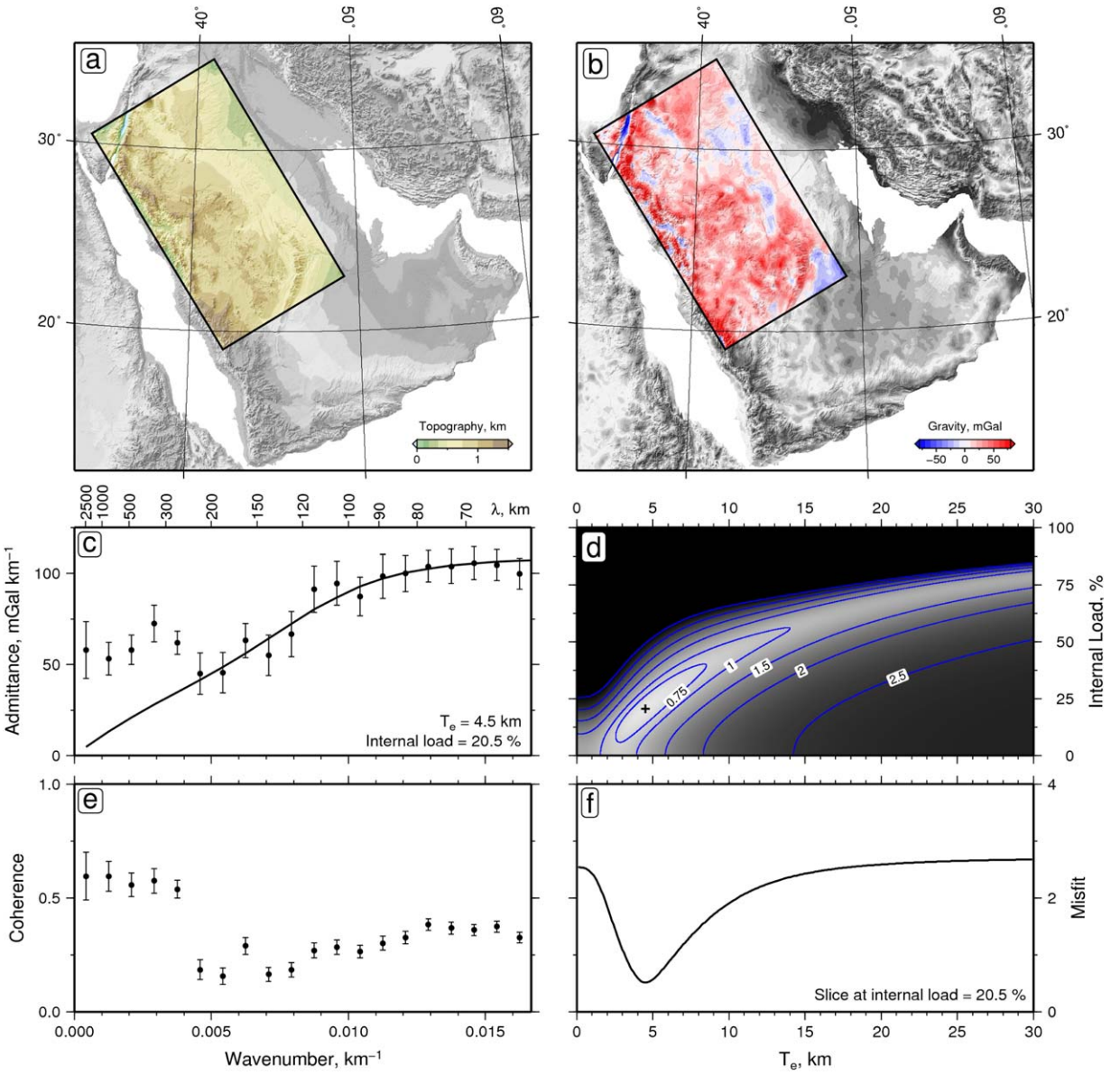

Figure 3. Admittance analysis of West Arabian Swell. (a) SRTM30_PLUS topography [*Becker*, 2009]. (b) Free-air gravity anomaly from EIGEN-6C3stat data set at 6 minute resolution [*Förste et al*., 2013]. (c) Admittance, *Z*, as function of wave number. Solid circles with error bars = observed values of *Z* with one σ uncertainties; solid line = values of *Z* calculated using elastic plate model with T_e=4.5 km for internal loading of 20.5% [*McKenzie*, 2003]. Crustal thickness = 38 km, upper crustal thickness = 10 km, upper crustal density = 2.6 Mg m^{-1}, lower crustal density between observed and calculated *Z* as function of T_e and internal load= 2.85 Mg m^{-1}. (d) Misfit between observed and calculated *Z* as function of T_e and internal loading with black cross at global minimum. (e) Coherence between free-air gravity and topography as function of wave number. (f) Slice through misfit space for internal loading of 20.5% with minimum at T_e=4.5 km. If minimum misfit value is doubled, T_e range is 3–6.5 km.

2. Geologic and Geophysical Evidence

A range of geologic and geophysical observations suggest that the Western Arabian swell is thermally and dynamically supported. First, pronounced topographic asymmetry exists on either side of the Red Sea basin. Its western flank is topographically subdued with an average elevation of $\sim$ 500 m whereas the Arabian flank is a broad undulating tableland with an average elevation of 1000–1500 m [*Camp and Roobol*, 1992; *Bohannon et al*., 1989].

Second, the age and composition of magmatism appear to have been controlled by adiabatic decompression of anomalously hot asthenosphere [*Camp and Roobol*, 1992]. Magmatism intrudes Precambrian basement through vent systems known as harrats. Radiometric age determinations from 317 localities suggest that there are two separate magmatic phases with evidence of younging from south to north (Figure 1)

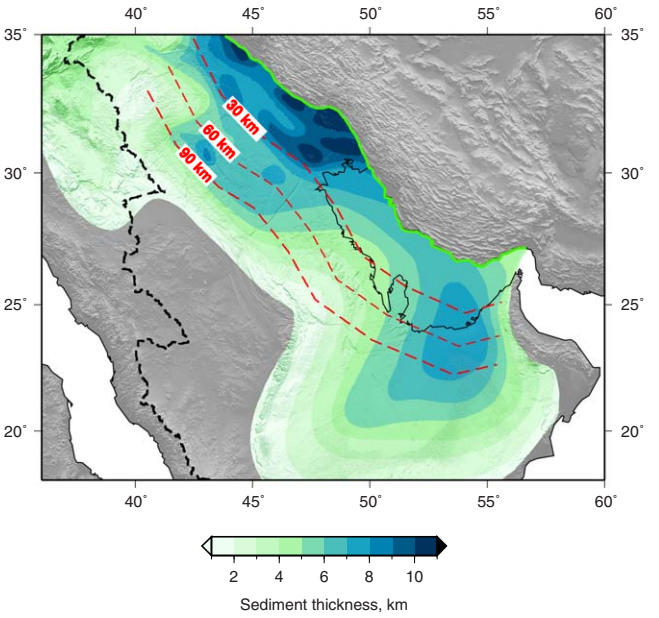

Figure 4. Flexural calculations. Blue/green/white colors = Cenozoic sedimentary isopach map [*Divins*, 2008]; dashed red lines = loci of flexural forebulge for T_e range of 30–90 km, assuming load is Zagros Mountains; dashed black line = drainage divide.

[*Civetta et al.*, 1978; *Coleman et al.*, 1983; *Pallister*, 1987; *Capaldi et al.*, 1987; *Chisea et al.*, 1988; *Hussain and Bakor*, 1989; *Camp and Roobol*, 1989; *Brown et al.*, 1989; *Sebai et al.*, 1991; *du Bray et al.*, 1991; *Baker et al.*, 1996; *Coulié et al.*, 2003; *Riisager et al.*, 2005; *Krienitz et al.*, 2009; *Trifonov et al.*, 2010; *Al-Kwatil et al.*, 2012; *Moufti et al.*, 2013]. An older (30–20 Ma) series is contemporaneous with Ethiopian flood basalts and is predominantly tholeiitic to transitional in composition [*Camp and Roobol*, 1992]. A younger (i.e., $<$ 12 Ma) series was emplaced along a linear vent system, known as the Makkah-Madinah-Nafud volcanic line. This series crops out oblique to the trend of the Red Sea but parallel to the crest of the Western Arabian swell [*Brown*, 1972; *Greenwood*, 1973; *Camp and Roobol*, 1989, 1992]. Its basaltic rocks are transitional to strongly alkalic in composition. The northward younging trend of Arabian magmatism has been used to argue that hot asthenosphere flowed beneath western Arabia [*Camp and Roobol*, 1992; *Ebinger and Sleep*, 1998; *Krienitz et al.*, 2009]. This inference is corroborated by the existence of a subplate low velocity zone [*Hadiouche and Zurn*, 1992; *Debayle et al.*, 2001; *Pasyanos and Nyblade*, 2007; *Sicilia et al.*, 2008; *Chang et al.*, 2011].

Thirdly, dynamic support of oceanic crust in the Red Sea and Gulf of Aden can be estimated by comparing measurements of water-loaded subsidence with an age-depth curve [*Crosby et al.*, 2006; *Winterbourne et al.*, 2009]. Residual bathymetry varies from + 0.75 to + 2.2 km (Figure 2a). Earthquake seismic activity is mostly confined to the edges of the Arabian plate. Focal plane mechanisms are consistent with horizontal extension across the Red Sea and Gulf of Aden, shortening along the Zagros fold and thrust belt, and strike-slip displacement along the Dead Sea fault [*Dziewonski et al.*, 1981; *Craig et al.*, 2011; *Ekström et al.*, 2012]. In the Red Sea, events of magnitude $>$ 4.7 rarely occur and bathymetry is smooth compared with the Gulf of Aden [*Engdahl et al.*, 1998]. These differences may reflect elevated mantle temperatures along the ridge axis. Onshore, structure of the shield is dominated by inactive, northwest-striking Neoproterozoic faults (e.g., the Najd fault system). Thus the teleseismic record indicates that regional uplift cannot be maintained by active faulting processes.

Fourthly, the crustal, lithospheric and sublithospheric structure beneath the Arabian Peninsula indicates that long wavelength topography is supported by density variations within the lithospheric and/or sublithospheric mantle [*Zor et al.*, 2003; *Al-Damegh et al.*, 2005; *Hansen et al.*, 2007b; *Tiberi et al.*, 2007; *Gök et al.*, 2008; *Al-Hashmi et al.*, 2011; *Ahmed et al.*, 2013]. Measurements of crustal thickness from seismic wide-angle surveys and from teleseismic receiver function analyses demonstrate that the crust is 20–38 km thick beneath the Western Arabian swell, where the average elevation is 1–1.5 km. These values contrast with $>$ 40 km thicknesses beneath the Arabian Platform where the average elevation is $\leq$ 0.5 km [*Al-Damegh et al.*, 2005; *Hansen et al.*, 2007b]. Elevation differences could be maintained by crustal isostasy if the crust beneath the Arabian Platform is considerably denser than that beneath the Western Arabian swell. Magmatic underplating is a popular mechanism, although it is more likely to have been important beneath volcanically active swells. Lack of correlation between crustal thickness and elevation measurements suggests that topography is at least partially supported by subcrustal density variations (Figure 2d). Isostatic constraints are corroborated by surface wave tomographic models which show that, compared to the Arabian platform, the lithosphere beneath western Arabia is not anomalously thick (Figure 2c) [*Fishwick*, 2010].

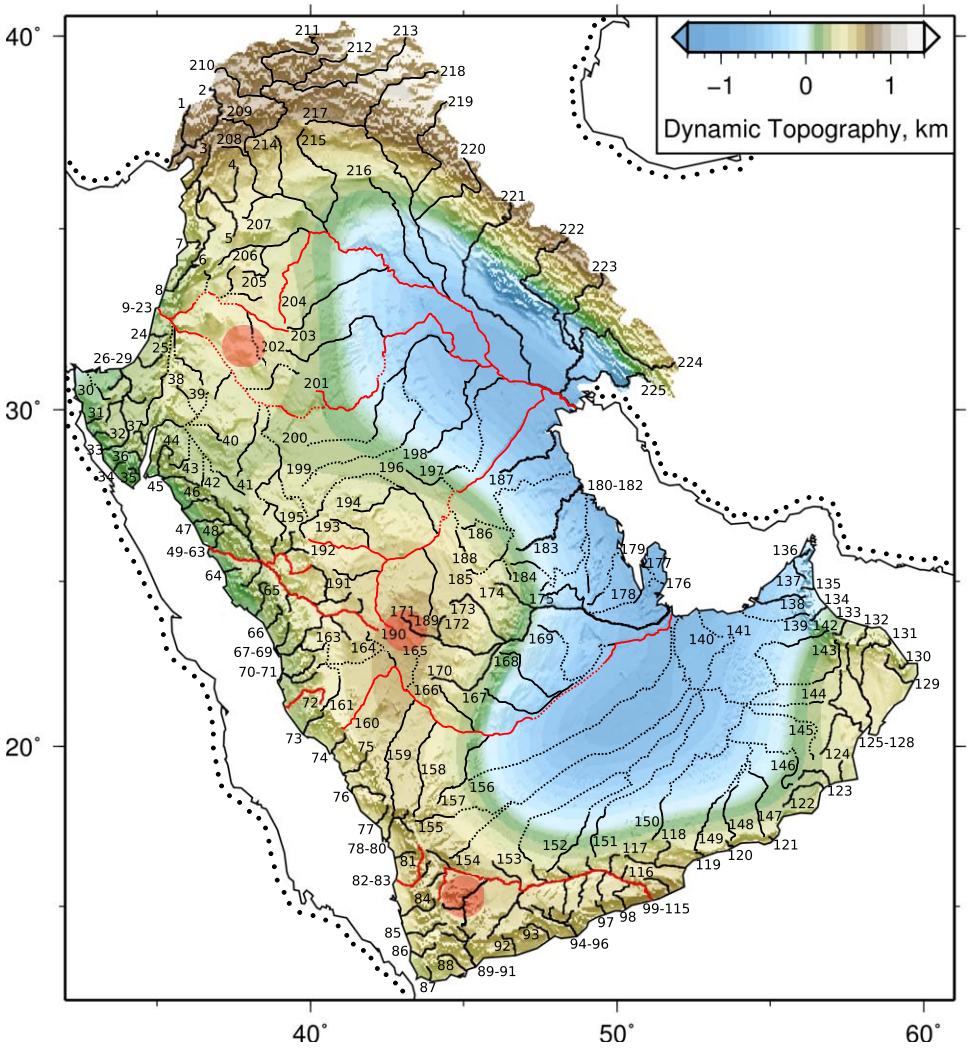

Figure 5. Present-day dynamic topography estimated from long wavelength (> 800 km) free-air gravity anomaly using $Z = 50$ mGal km^{-1}. Numbered lines = drainage extracted from SRTM data set (solid = verifiable drainage; dotted = ephemeral lakes/paleodrainage/internal drainage); red lines = river profiles from Figure 7; transparent red circles = loci of domal swells.

Finally, it is useful to examine the relationship between free-air gravity anomalies and topography [*McKenzie*, 1977]. The western Arabian Penisula has a long wavelength (∼ 1200 km) gravity anomaly with an amplitude of + 30 mGal. This anomaly yields a qualitative estimate of the amplitude and wavelength of convective support (Figure 2a). It is similar to magmatically active swells in East Africa which have 0.75–1 km of dynamic support [*McKenzie and Fairhead*, 1997]. Spectral analysis of the free-air gravity field and topography yields an admittance, Z, at wavelengths of > 2000 km of 58 ± 15 mGal km^{-1} (Figure 3). This value agrees with the signal expected for dynamic support by mantle convection on the continents ($Z \sim 50$ mGal km^{-1}) [*McKenzie*, 1994]. Thus onshore and offshore estimates of the present-day signal of dynamic topography broadly agree. The wavelength dependence of Z permits the elastic thickness, T_e, to be calculated by minimizing the misfit between observed and calculated admittance as a function of T_e [*McKenzie and Fairhead*, 1997]. We find that T_e of a region encompassing the Western Arabian swell is $4.5^{+2.0}_{-1.5}$km (Figure 3). Adjacent to the Persian Gulf, admittance analysis suggests that T_e is ∼ 30 km (D. *McKenzie*, and K. Priestley, The planform of convection beneath the Middle East equatorial and northern Africa, submitted to *Geophysical Journal International*, 2014). Thus long wavelength topography of the Arabian Peninsula and the locus of the principal drainage divide cannot be flexurally maintained (Figure 4). It has been suggested that the hinge line of the forebulge coincides with the western shoreline of the Persian Gulf where a series of paleo-marine terraces and shorelines have been uplifted by 125 m in the last 18 Ka [*Ridley and Seeley*,

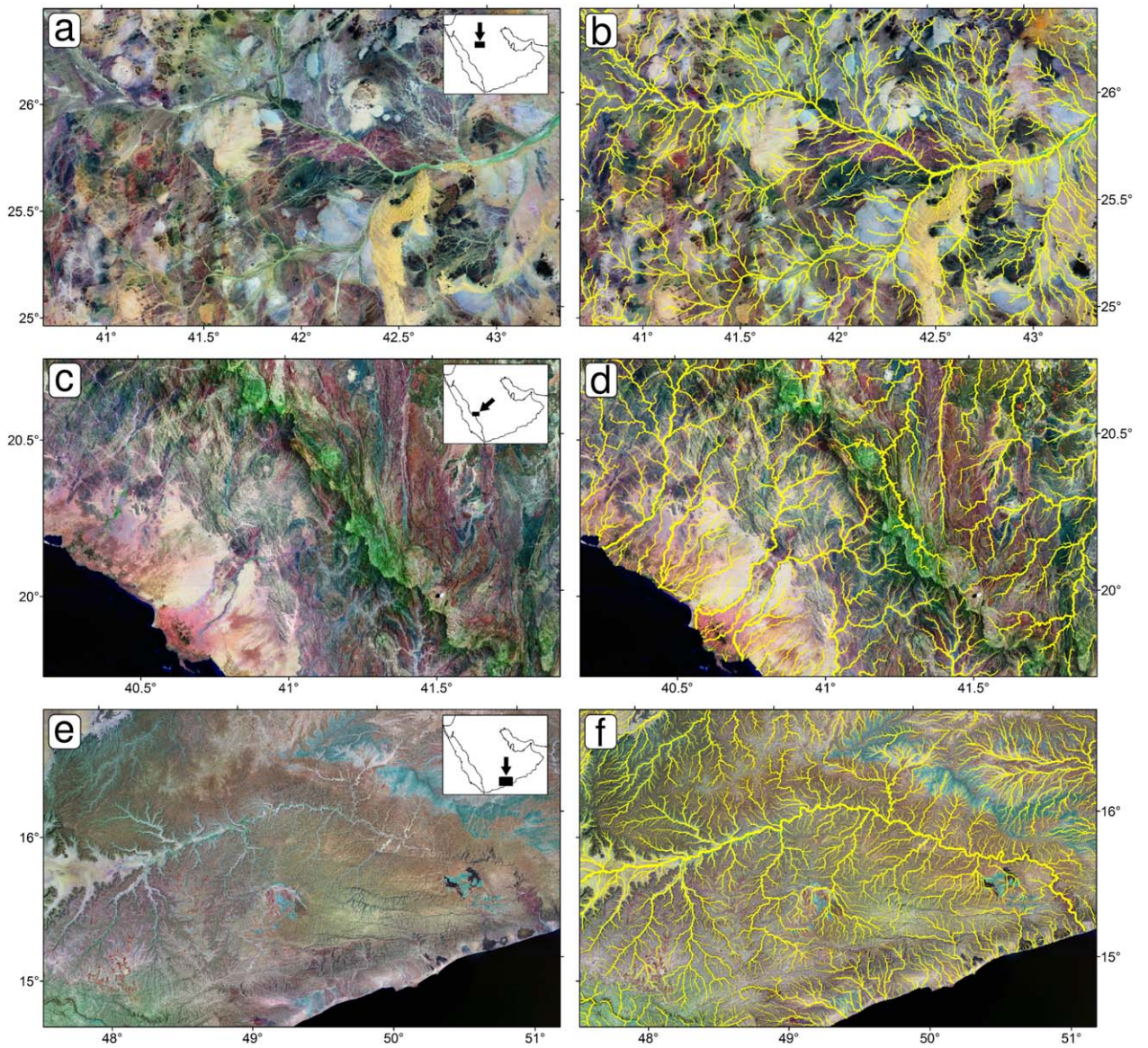

Figure 6. Comparison of recovered drainage with Landsat imagery (bands 2/4/7). (a) Karmat Khayan region with inset map. (b) Image overlain with recovered drainage (e.g., river profiles 190–193; Figure 6). (c, d) Red Sea escarpment (e.g., profile 74). (e, f) Wadi Masilah (e.g., profiles 99–115).

1979; *Wood et al*., 2012]. To the southeast, the Oman Mountains are uplifting by 2 mm a^{-1} whereas the northern tip of the Musandam Peninsula is subsiding by 6 mm a^{-1} which suggests that the putative hinge line is now closer to the Zagros Mountains.

3. Drainage

3.1. Longitudinal River Profiles

A digital elevation model of the Arabian Peninsula was generated using 3 arc second (90×90 m^2 resolution) Shuttle Radar Topographic Mission (SRTM) data [*Farr et al*., 2007]. First, we deleted anomalous spikes and sinks from this digital topography. Second, drainage networks were identified by calculating flow directions using the ArcGIS software package [*Tarboton*, 1997]. Finally, we extracted longitudinal river profiles (i.e., elevation as a function of distance along river) from these drainage networks (Figure 5). Away from deep and narrow channels, the vertical and horizontal resolution of this inventory is ±16 m and ±20 m, respectively [*Hancock et al*., 2006]. In regions with internal drainage, where paleolakes may have existed, horizontal accuracy deteriorates

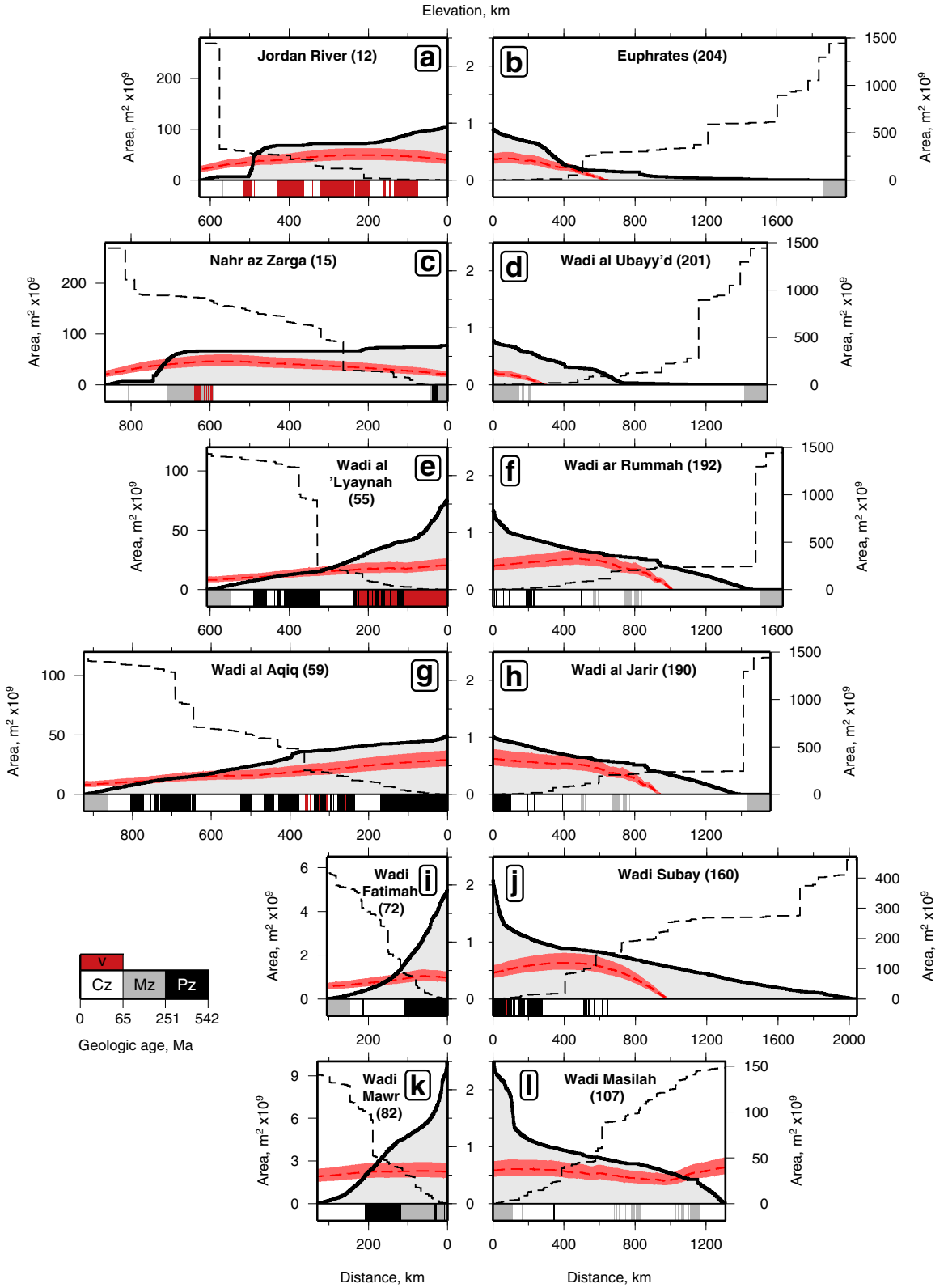

Figure 7. Selected river profiles that drain west into Red Sea (left) and east into Persian Gulf (right) (see Figure 5 for location). In each figure, solid line = recovered river profile; dashed line = upstream drainage area; bar code along base = lithologic variation along river bed where black (Pz) = Precambrian/Paleozoic rocks, gray (Mz) = Mesozoic rocks, white (Cz) = Cenozoic rocks, red (v) = igneous rocks [*Pollastro et al.*, 1998]; red dashed line with band = dynamic support estimated from long wavelength free-air gravity using $Z=50\pm10$ mGal km^{-1} (Figure 5).

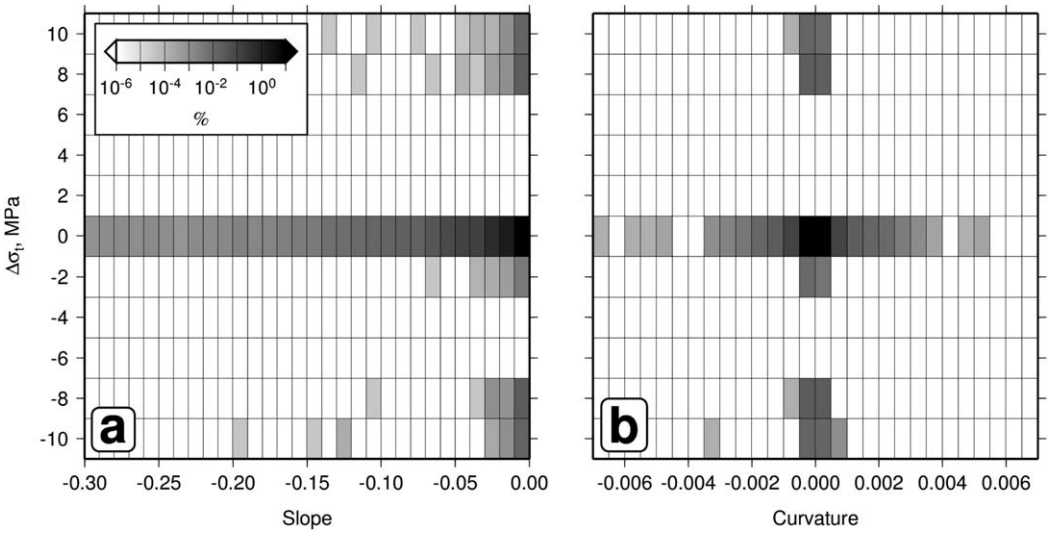

Figure 8. (a) Change in tensile strength estimated from lithologic variation, $\Delta\sigma_t$, plotted as function of river profile slope for Arabian drainage inventory (Appendix A). (b) $\Delta\sigma_t$ plotted as function of river profile curvature. Maximum values of $\Delta\sigma_t$ and slope were calculated within 5 km long moving window. Cell shading = percentage of data points which fall within given cell. At wavelengths $>$ 5 km, $<$ 10% of slope changes correlate with lithologic variations.

by many hundreds of meters. We have checked the fidelity of our digital drainage networks using Landsat and other satellite imagery (e.g., Figures 5 and 6). Details of the drainage inventory are provided in Appendix A.

3.2. Aridity and Drainage Recovery

The great deserts of Arabia—Rub' al-Khali, ad-Dahna, An Nafud—are amongst the largest on Earth. These sand seas are young physiographic features of the Arabian Peninsula whose climate has markedly changed in recent times. For example, vertebrate fauna and palynological data suggest that savannah conditions with widespread grassland prevailed until Late Miocene times [*Andrews et al*., 1978; *Hamilton et al*., 1978; *Whybrow*, 1987; *Whybrow and Hill*, 1999]. Sedimentary facies indicate that pluvial and humid conditions occurred during Late Miocene and Pliocene times [*Whybrow and McClure*, 1981]. Lateritic paleosol horizons that blanket Pliocene basaltic lava flows are also consistent with humid conditions [*Höltz et al*., 1978]. Aridity developed by Mid-Pleistocene times and was exacerbated during periods of high-latitude glaciation when coastal sabkhas were exposed at sea-level lowstands [*Edgell*, 2005; *Garzanti et al*., 2013]. This aridity enhanced production of sand and silt deposits, which were then blown inland to form deserts [*Edgell*, 2005].

Youthful desertification can mask ancient drainage networks (Figure 5). However, paleohydrological studies show that drainage networks derived by flow-routing algorithms often match paleo-drainage patterns inferred from false color composite Landsat imagery, from shuttle radar imagery (e.g., SIR-C/X-SAR), and from fieldwork observations [*Dabbagh et al*., 1997, 1998; *Crassard et al*., 2013]. It follows that our reconstructed drainage network honors these preserved paleo-drainage patterns. Regions with less adequate drainage recovery are usually of low relief and contain little direct information about uplift rate.

3.3. Knickzones and Knickpoints

Sets of river profiles that are orthogonal to the principal drainage divide have irregular, convex-upward, morphologies (Figure 7). Long wavelength (i.e., 10^2-10^3 km wide) knickzones separate regions of lower relief but many sharper ($<$ 10 km) knickpoints occur. Knickzones broadly correlate on either side of the drainage divide at 0.5–0.75 km elevation. Their loci correlate with changes in dynamic topography (Figure 7). Rivers draining the peninsula traverse different lithologies but apices of prominent knickzone do not generally coincide with lithologic contacts. Correlations between changes in tensile strength at lithologic contacts, $\Delta\sigma_t$, and loci of knickpoints/knickzones were investigated using *Sklar and Dietrich*'s [2001] methodology (Figure 8). Our results imply that, at wavelengths of $>$ 5 km, river profile slope and curvature weakly correlate with lithologic contrasts. Thus longer wavelength knickzones appear not to be lithologically maintained and may instead reflect temporal and spatial patterns of regional uplift.

3.4. Longevity of Drainage Networks and Divides

Long-term stability of the main drainage divide has been recognized [*Almond*, 1986]. For example, basaltic flows of Harrats Rahat, Ithnayn, Kura and Khaybar follow drainage patterns on either side of this drainage divide (Figure 9). K-Ar dates from the stratigraphically oldest flows (i.e., Shawahit basalt of Harrat Rahat) are 12–19 Ma [*Coleman et al*., 1983]. Further north at Harrats Ithnayn, Kura and Khaybar, K-Ar dating of the lowest flows yields 9–12 Ma [*Camp et al*., 1991]. These basaltic flows are separated by disconformable erosional surfaces that are characterized by a mature and incised dendritic drainage network [*Camp and Roobol*, 1989]. Basaltic flows of the Yemeni volcanic province also appear to follow present-day drainage patterns. These flows are 27–31 Ma which suggests that the overall drainage pattern of Arabia has remained roughly stable during Neogene times [*Baker et al*., 1996]. There is little reported evidence for large-scale drainage capture or for wholesale migration of drainage divides during this time interval. Furthermore, barbed drainage and wind gaps are generally absent from present-day drainage patterns on either side of the principal drainage divide (Figure 5). This divide is oriented at 25° oblique to the trend of the Red Sea but it is parallel to the expression of volcanic activity across the Western Arabian swell. This correspondence suggests that drainage asymmetry developed in response to the spatial configuration of dynamic support which is manifest by three domal swells (Figure 5).

4. Calculating Uplift Histories

4.1. Inverse Modeling

River profiles can be used to calculate smooth spatial and temporal patterns of uplift rate, provided that key erosional parameters are independently calibrated [*Pritchard et al*., 2009; *Roberts and White*, 2010; *Hartley et al*., 2011; *Roberts et al*., 2012a, 2000b]. The rate of change of elevation (i.e., surface uplift), *dz/dt*, along a river profile may be described by

$$\frac{\partial z}{\partial t} = U(x,t) + E(x,t), \tag{1}$$

where U is uplift rate, E is erosion rate, and x is distance along a given river profile [*Rosenbloom and Anderson*, 1994; *Whipple and Tucker*, 1999]. This ansatz equation assumes that the shape of a river profile is controlled by U but moderated by E. In order to extract information about U from observed river profiles, it is usually assumed that E is controlled by integrated discharge, which varies as a function of upstream drainage area, A, and time, t, so that

$$E(x,t) = -vA^m \left(\frac{\partial z}{\partial x}\right)^n + \kappa \frac{\partial^2 z}{\partial x^2}, \tag{2}$$

where n and m can exert significant controls on the concavity of a given profile [*Whipple and Tucker*, 1999]. A^m acts as a proxy for integrated discharge at any position x along a river [*Hack*, 1957; *Whipple and Tucker*, 2002]. The value of n is much debated [*Berlin and Anderson*, 2007]. m typically varies between 0.35 and 0.6, although values as low as 0.1 have been reported [*Tucker and Whipple*, 2002; *Schoenbohm et al*., 2004]. If $n = 1$ and $m = 0$, then v is, by definition, the advective (i.e., knickpoint) velocity. If $n \neq 1$ and $m > 0$, v becomes a nonlinear function of upstream drainage area. Together, v, m and n control the value of the advective term that governs the transient form of a river profile. This term represents the detachment-limited component of erosion [*Whipple and Tucker*, 1999]. Downwearing caused by transport-limited erosion can be approximated using "erosional diffusivity" which is represented by κ [*Whipple and Tucker*, 1999, 2002].

Equations (1) and (2) imply that if the shape of a river profile is known, it should be possible to extract uplift rate histories as a function of time, $U(t)$, by inversion. To invert for U, *Roberts and White* [2010] devised a trial function, with appropriate penalties, that measures differences between observed and calculated river profiles for varying U. In the one-dimensional problem, this trial function is minimized by systematically varying U as a function of time alone. The aim is to calculate a smooth temporal distribution of U that yields a best-fitting synthetic river profile. The efficacy of this approach strongly depends on independently calibrated values of the four erosional parameters.

Crosby and Whipple [2006b] suggested that knickpoint retreat velocities vary by up to 5 orders of magnitude (i.e., $1–10^4$ cm a^{-1}). Within the advective term, v and m are the most important constants, since their values

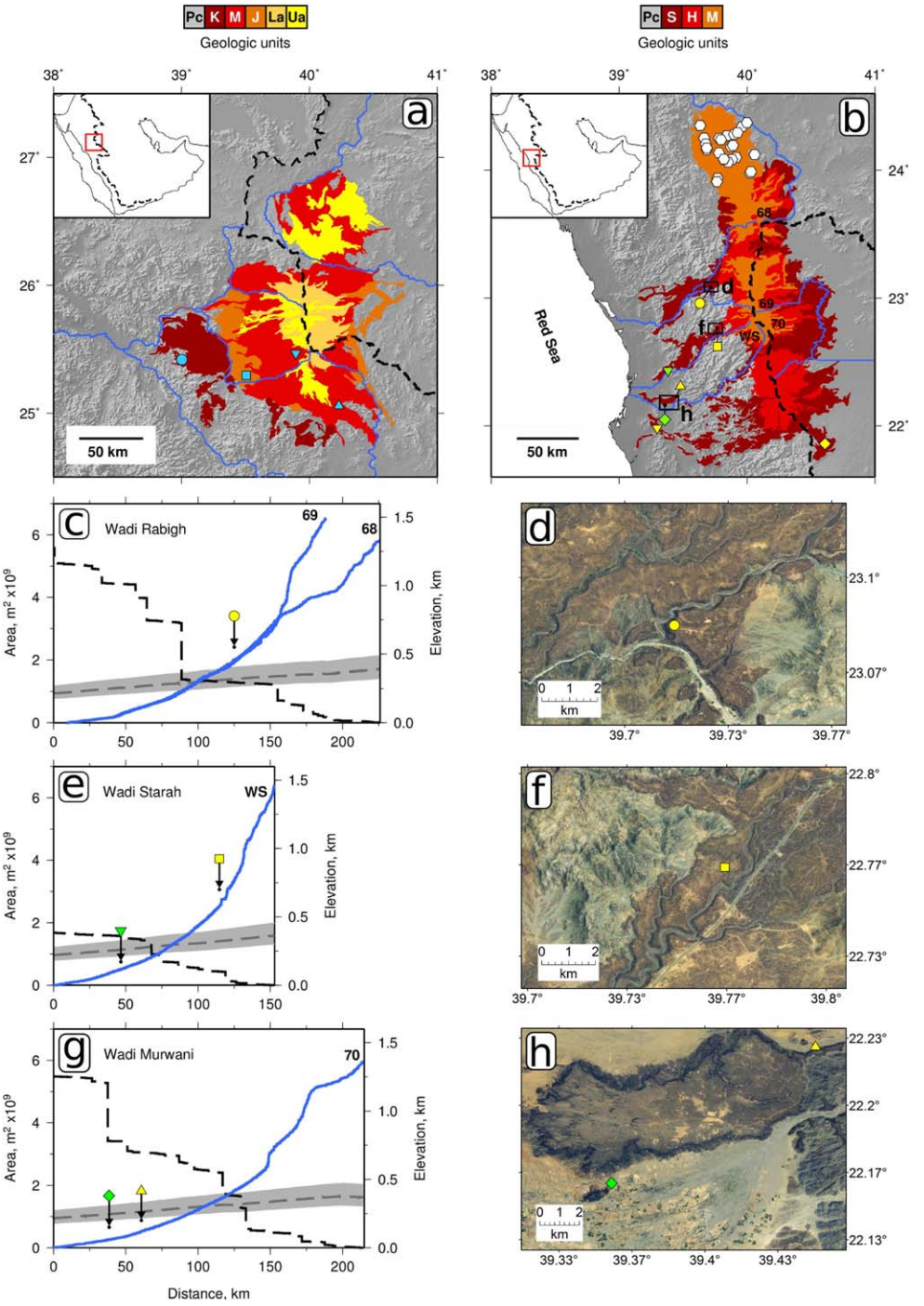

Figure 9. (a) Geologic map of Harrat Khaybar, Ithnayan, and Kura volcanic fields [*Camp et al.*, 1991]. Dark red shading = Kura basalt; red = Mukrash basalt; orange = Jarad basalt; tan = Lower Abyad basalt; yellow = upper Abyad basalt [after *Camp et al.*, 1991]; gray = Precambrian basement; blue circle/square/upward triangle/downward triangle = 11.5 ± 2.3 Ma/4.18 Ma/2.84 Ma/1.1 ± 0.3 Ma, respectively (K-Ar ages from *Coleman et al.* [1983]); dashed line = drainage divide; thin blue lines = river profiles. (b) Geologic map of Harrat Rahat [*Camp and Roobol*, 1989]. Dark red shading = Shawahit basalt; red = Hammah basalt; orange = Madinah basalt [after *Camp and Roobol*, 1989]; gray = Precambrian basement; yellow diamond/square/circle/downward triangle/upward triangle = 19.1 ± 6 Ma/13.2 ± 1.5 Ma/12.6 ± 2.5 Ma/8.7 ± 2 Ma/4.4 ± 0.4 Ma, respectively (K-Ar ages from *Coleman et al.* [1983]); green diamond/triangle = 3.73 ± 0.16 Ma/3.3 ± 0.17 Ma, respectively ($^{40}Ar/^{39}Ar$ ages from *Hussain and Bakor* [1989]); white circles = 0.5–10.31 Ma ($^{40}Ar/^{36}Ar$ ages from *Moufti et al.* [2013]); dashed line = drainage divide. (c) Wadi Rabigh river profiles. Blue lines = river profiles; dashed line = upstream drainage area; gray band = dynamic support calculated from long wavelength free-air gravity using $Z = 50 \pm 10$ mGal km^{-1}; yellow circle = present-day elevation of dated lava flow. (d) Satellite image of Wadi Rabigh showing river channel and lava flows. Dark red/brown shading = lava flows; light brown = basement rocks; yellow circle = dated flow. (e, f) Wadi Starah profile. Yellow square/green triangle = dated flows; (g, h) Wadi Murwani profile. Yellow triangle/green diamond = dated flows.

have a direct bearing upon knickpoint retreat velocity. v and m trade off negatively with each other [*Roberts and White*, 2010]. Previous calibration studies suggest that values of v and m might geographically vary. For the Colorado Plateau, $v \approx 4.16 \times 10^4$ $(2.78 \times 10^{-12})^m$ and so if $m = 0.2$, $v = 203\ \mathrm{m}^{0.6}\ \mathrm{Ma}^{-1}$ [*Roberts et al.*, 2012b]. In contrast, $v \approx 2445 \exp(-20m)$ for Australia and so if $m = 0.2$, $v = 45\ \mathrm{m}^{0.6}\ \mathrm{Ma}^{-1}$ [*Czarnota et al.*, 2013]. The inter and intra-continental variations of v and m are not well known. Our pragmatic approach emphasizes the importance of testing the extent to which locally estimated values can be reasonably extrapolated across a single continent.

4.2. Landscape Response Time

If $\kappa = 0$ and $n = 1$, the time taken for a knickzone emplaced at the coastline to propagate upstream, τ_G, is approximated by

$$\tau_G = \int_0^x \frac{dx}{vA^m} \approx \sum_{i=1}^{x} \frac{\triangle xi}{vA_i^m}. \tag{3}$$

In Figure 10, τ_G is plotted for the Arabian Peninsula. τ_G varies on either side of the main drainage divide since west-draining catchments are shorter "tape recorders" of uplift (i.e., 25–75 Ma) compared with east-draining catchments ($\sim$ 150 Ma). This east-west disparity is a function of asymmetry in catchment size and river length. The response time of west-draining catchments also increases from south to north along the principal drainage divide. This increase matches the change in orientation of this divide from northwest-southeast (i.e., parallel to Red Sea) to approximately north-south (i.e., parallel to northern end of Western Arabian swell; Figure 10).

4.3. Erosional Calibration

Independent geologic and geophysical constraints are used to constrain a local trade-off relationship between v and m. Half-way down the Red Sea at Harrat Rahat, radiometrically dated lava flows are incised by wadis draining to the southwest (Figure 9) [*Coleman et al.*, 1983; *Hussain and Bakor*, 1989]. It is straightforward to measure the horizontal displacement, x, between the height of these flows, which represent the paleo-river profile, and the present-day river channels. *Roberts et al.* [2012b] and *Czarnota et al.* [2013] used a similar approach to estimate v-m relationships in Africa and Australia, respectively. At Harrat Rahat, the horizontal component of the average vertical incision is $dx/dt = 9.678 \pm 0.39\ \mathrm{mm\ a}^{-1}$ where the upstream drainage area $A = 3.416 \times 10^9\ \mathrm{m}^2$. If $\kappa = 0$ and $n = 1$, $dx/dt \sim vA^m$ which yields a trade-off relationship between v and m (Figure 11). For example, if $m = 0.2$ we obtain $v = 120 \pm 5$ and if m varies between 0.02 and 0.5, v decreases from 6239 to 0.1656.

4.4. Uplift as Function of Time

Our objective is to determine uplift rate histories by inverting sets of river profiles. Given a trade-off relationship between v and m, how well can observed river profiles be fitted and how reliable are calculated uplift histories? We tackle this problem by determining uplift histories for westward draining river profiles that are short compared to the length scale over which uplift occurs. These profiles are amenable to one-dimensional inverse modeling where uplift varies as a function of time alone (i.e., block uplift with upstream knickzone propagation from the river mouth).

We extracted uplift rate histories using the inverse approach of *Roberts and White* [2010]. In each case, uplift rate is systematically varied in order to find a smooth distribution of U that minimizes the misfit between observed and calculated profiles. In our starting model, $U(t) = 0$ and $z(x) = 0$. Different values of erosional parameters affect both residual misfit and, more importantly, calculated uplift histories. The sensitivity of our results to changes in advective erosional parameters was investigated by inverse modeling of Wadi Starah from Harrat Rahat where local incision measurements exist. In Figures 12a–12g, we show the results of covarying m and v for $n = 1$, which accords with the previously calibrated trade-off relationship. Residual misfit, χ^2, between observed and calculated river profiles is minimized when $m = 0.2$ for which $v = 120\ \mathrm{m}^{0.6}\ \mathrm{Ma}^{-1}$. This value for m falls within the published range [*Schoenbohm et al.*, 2004]. Increasing m while covarying v tends to displace the uplift history back in time.

A systematic sweep through v-m-n space was carried out by allowing v, m and n to covary between $0.1-10^3$, 0–1, and 0–2 (Figures 12h–12n). A three-dimensional sweep of repeated inverse models reveals a weak positive trade off between m and n for different values of v. Residual misfit in the direction of

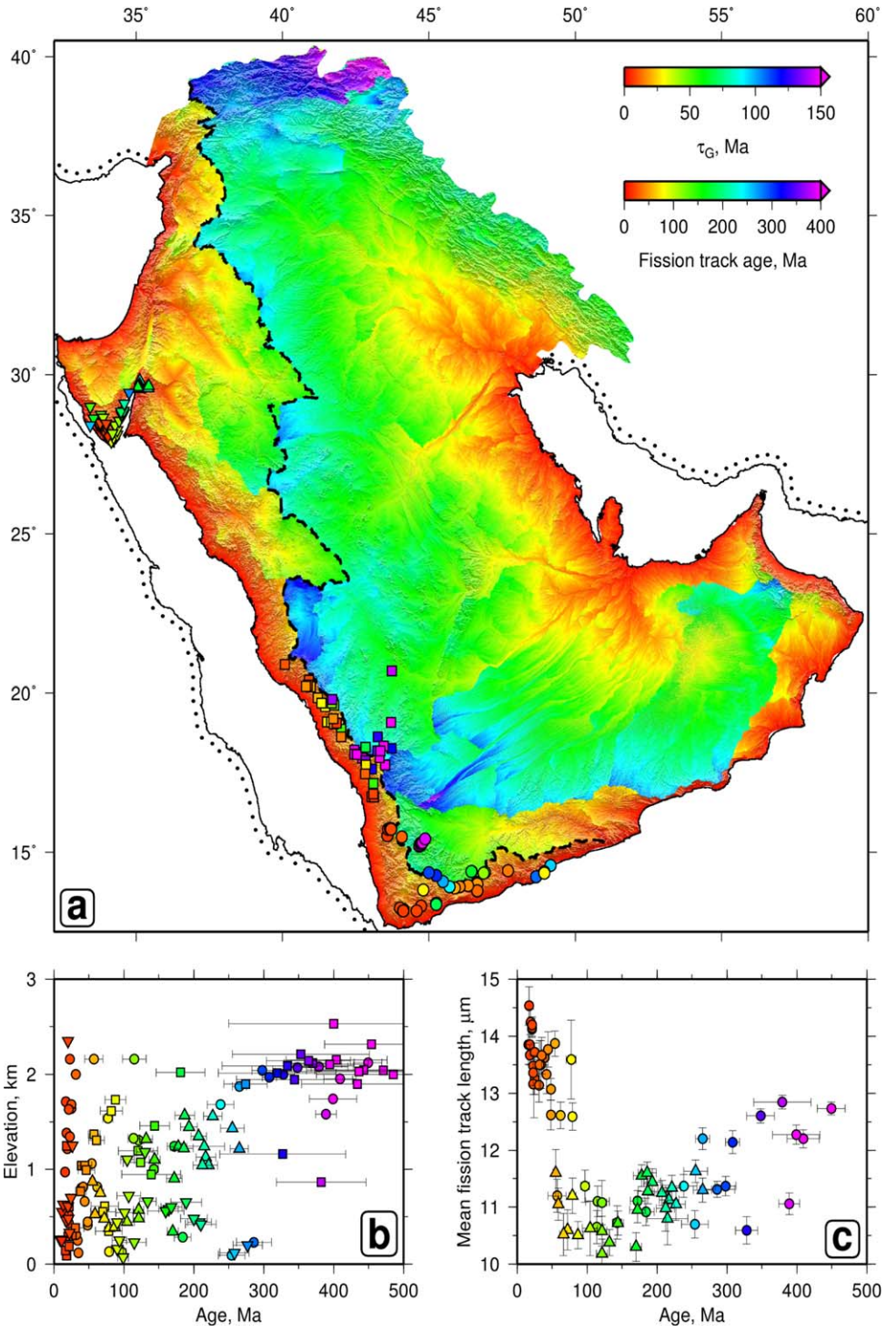

Figure 10. (a) Map of landscape response time and fission track data. τ_G calculated from digital topographic model using equation (3). Dashed line = drainage divide; upward triangles = fission track data from *Feinstein et al*. [2013]; downward triangles = *Kohn and Eyal* [1981]; squares = *Bohannon et al*. [1989]; circles = *Menzies et al*. [1997]. (b) Elevation as function of Fission track age. (c) Mean fission track length as function of fission track age.

covariance suggests that there is a global minimum at $n = 1$ (Figure 12n). More critically, if n deviates from 1 in either direction, the resultant uplift rate histories violate regional stratigraphic constraints. These results corroborate one-dimensional studies of African and Australian river profiles which show that when $n \neq 1$, residual misfits between predicted and observed profiles become unacceptably large [*Roberts et al*., 2012a;

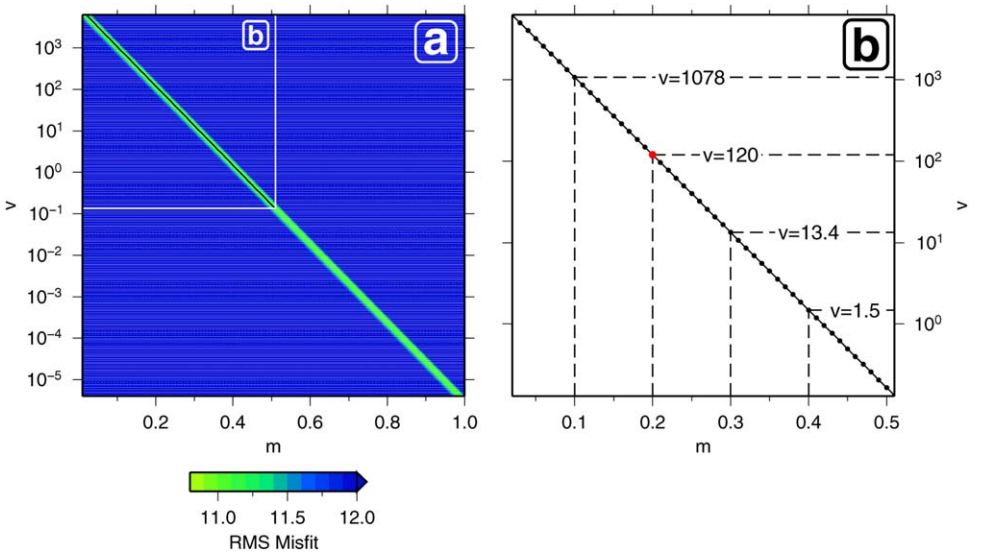

Figure 11. Calibration of erosional parameters. (a) Misfit between observed and calculated rates of incision (i.e., dx/dt) as function of m and v. White box = expanded plot. (b) Expanded plot showing trade-off between m and v. Black circles = loci of m and v values used for inverse modeling of Wadis Starah, Murwani, and Rabigh (Figure 12); red circle = locus of global minimum along m and v trade-off for Wadi Starah.

Czarnota et al., 2013]. A continent-wide analysis of Africa in which n varies between 0 and 2 shows that 710 river profiles can only be simultaneously fitted for $n = 1$ [*Paul et al*., 2014].

If $n > 1$, shock waves can develop so that a steeper reach of a river overtakes a less steep reach which propagates upstream at a slower velocity. *Pritchard et al*. [2009] showed that a shock can form within the domain $0 \leq x \leq L$ where L is the length of a river profile if, and only if,

$$\left(\frac{n-1}{n}\right)\frac{dU}{dt} > (n-m)v_{\circ}^{1/n}L^{m/n-1}[U(t)]^{2-1/n} \tag{4}$$

at some stage during uplift where vA^m is approximated by $v_{\circ}x^m$. If a shock forms, the river erases part of its history and the reconstructed record will contain a gap [*Pritchard et al*., 2009]. *Pritchard et al*. [2009] and *Roberts et al*. [2012a] suggested that n is ~1 since there is not, as yet, unambiguous observational evidence that supports shock behavior of knickzones.

In contrast, κ can vary by many orders of magnitude (e.g., 1–10^7 m^2 Ma^{-1}) without affecting our results (Figures 12o–12u). This insensitivity reflects the fact that river profiles are sampled every 10–20 km which means that the minimum resolvable value of κ is 10^7 m^2 Ma^{-1}. This value is greater than published estimates which suggests that erosional "diffusivity" can be neglected [*Roberts et al*., 2012a]. Upstream drainage area can also vary substantially without significantly affecting our results (Figures 12v–12ab). This insensitivity is a direct consequence of m being a fractional power and suggests that solutions are not unduly sensitive to putative river capture events, drainage divide migration, and/or uncertainties in estimating present-day upstream drainage area. Uncertainty in the length of a river profile is more important. At many coastlines, the shelf break lies within 50 km of the coast and the extent of estuaries and coastal plains can vary substantially between high and low-stands of sea level. We dissect this problem by varying the length of Wadi Starah between −20 and + 50 km (Figures 12ac–12ai). As expected, residual misfit is not affected but the peak of uplift rate is shifted by up to ±5 Ma.

A two-fold strategy is used to test whether locally calibrated values of v and m yield independently verifiable results elsewhere. v and m may vary between different continents, within a continent, or even within a single drainage catchment. It is also possible that v and m vary through geologic time. In the absence of tangible measurements, it is useful to explore parsimonious models that minimize misfit between observed and predicted river profiles. First, we modeled four river profiles that drain Harrat Rahat using the previously determined trade-off relationship between v and m (i.e., $v = 9.678 \times 10^3 (3.4164018 \times 10^9)^{-m}$). A *Monte Carlo* inverse approach helps to explore how uncertainties in the values of v, m, n and κ map into calculated uplift

rate histories. All four profiles are fitted using a primary phase of uplift that commenced at 25 ±5 Ma. The peak uplift rate of 0.1 ± 0.05 mm a^{-1} occurred at ~15 Ma. There is evidence for a secondary phase of uplift at 10 ±3 Ma with a peak uplift rate of 0.05 ± 0.03 mm a^{-1}. The calculated present-day uplift rate is ~0.01 mm a^{-1}.

Calculated histories can be checked using a combination of local and regional observations (Figure 13). Uplifted marine strata and laterite deposits are suggestive of a low-lying landscape between 50 and 30 Ma. At the coastline, radiometric dating of emergent Plio-Pleistocene marine terraces implies an uplift rate of 0.02 ±0.01 mm yr^{-1} [*Dawood et al*., 2013]. Finally, thermochronometric analyses suggest that rapid cooling and denudation started at 20–25 Ma [*Bohannon et al*., 1989]. The agreement between our calculated uplift rate histories and these independent constraints is encouraging.

The validity of using invariant erosional constants is widely debated. The key issue concerns the trade-off relationship between v and m which directly scales uplift rate history. We can explore the validity of extrapolating a locally calibrated relationship between v and m. We have chosen three Yemeni profiles from the southern end of the Arabian Peninsula (Figure 14). These river profiles are short compared to the length scale over which uplift occurs and, once again, are amenable to one-dimensional inverse modeling where uplift rate varies as a function of time alone. The same range of values of v, m, n and κ were used to calculate uplift rate histories. These profiles are fitted using uplift histories which imply that Yemeni topography is youthful. Uplift commenced at 30 ±5 Ma, reaching an uplift rate peak of 0.1–0.3 mm a^{-1} at ~ 25 Ma. Once again, there is evidence for two phases of uplift with a second, smaller uplift rate peak at 10–15 Ma. The present-day uplift rate is ~ 0.02 mm a^{-1}.

Local stratigraphic observations help to corroborate these results. Between 50 and 35 Ma, submarine conditions prevailed across Yemen [*Al-Subbary et al*., 1998; *Al-Qayim et al*., 2005]. Uplifted outliers of strata from Twaliah Group provide a minimum average estimate of uplift. These estimates are corroborated by thermochronometric analyses which show that rapid cooling and exhumation commenced at 20–25 Ma [*Menzies et al*., 1997]. Eruption and later erosion of basaltic lava flows coincide with the onset and peak of calculated uplift [*Baker et al*., 1996; *Riisager et al*., 2005]. Thus geologically meaningful uplift rate histories of regions, separated by ~ 2000 km, are obtained using a single trade-off relationship between v and m. It remains to be determined whether this relationship holds across the rest of the peninsula. To test this possibility, many river profiles are modeled by allowing uplift rate to vary as a function of both time and space [*Roberts et al*., 2012a].

4.5. Uplift as Function of Time and Space

Spatial and temporal patterns of uplift rate are determined by simultaneously inverting river profiles which flow in different directions. We first define a grid of X × Y × T vertices. These vertices are spatial and temporal nodes at which uplift rate is permitted to smoothly vary. We prescribe a coarse grid spacing where $\Delta x = \Delta y = 300$km and a time scale of 50 Ma with a time step of $\Delta t = 2.5$ Ma. A starting distribution of uplift rate history is chosen. For simplicity, we use a flat plane upon which a grid of uplift rate values is set to zero, although it is important to emphasize that alternative initial landscapes can be used. Three lines of evidence support this, the simplest, starting model. First, there is fragmentary evidence that Eocene marine limestones fringed the Western Arabian swell (Figures 14a and 17c) [*Madden et al*., 1980; *Kluyver et al*., 1981; *Madden et al*., 1995; *Al-Subbary et al*., 1998; *Taj*, 2013]. Second, remnants of Cretaceous-Paleogene laterites, saprolite and bauxites, suggestive of low topographic gradient, sporadically crop out [*Chapman*, 1978; *Brown et al*., 1989; *Salpeteur and Sebir*, 1989]. Finally, this period of topographic quiescence was interrupted by regional magmatism that commenced at ~ 30 Ma. This abrupt switch is associated with subsequent incison and erosion of basaltic lava flows [*Coleman et al*., 1983; *Camp and Roobol*, 1989; *Baker et al*., 1996].

For simplicity, we assume that $v = 120$ and $m = 0.2$ which honor the trade-off relationship (Figure 11). Different combinations of v and m can be chosen without adversely affecting our results provided that this trade-off relationship is obeyed. Once again, it is important to explore, at least in the first instance, the predictive power of a parsimonious model. What features can be expected to be resolved by a smooth model? Figure 15 presents the model null space (i.e., maximum resolvable age of knickzones that are input at any position within the drainage network). This null space is constrained by values of τ_G along each river in the downstream direction using equation (3). Resolvable age decreases upstream from mouths of rivers. Figures 15b–15e summarize resolvable ages for different loci across the Arabian Peninsula. Thus we expect to

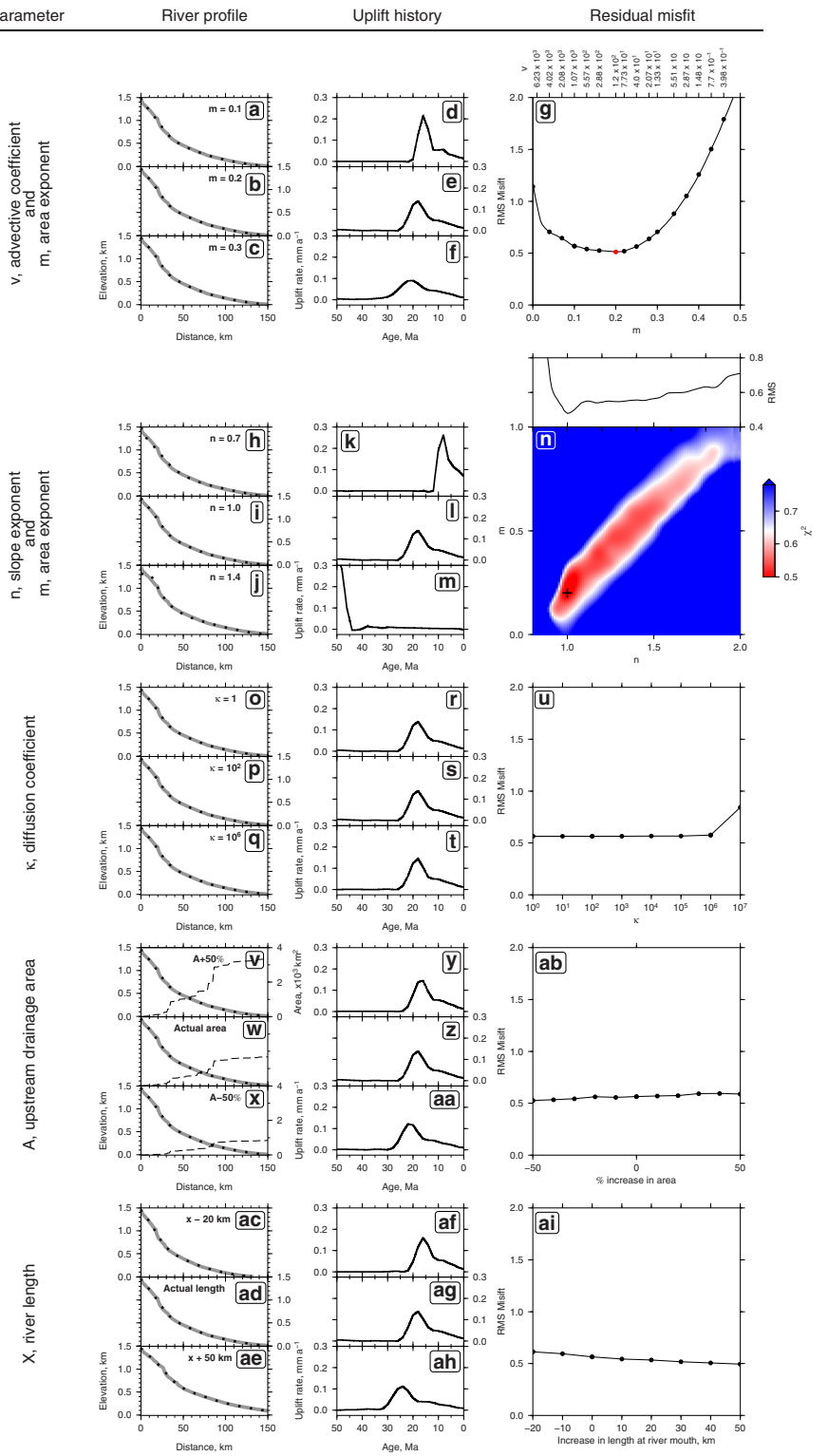

Figure 12. Variation of erosional parameters for Wadi Starah profile. (a–g) Covariation of m and v at $n = 1$. Three left-hand plots: gray lines = observed river profile; black dotted lines = predicted river profiles for $m = 0.1$, 0.2, and 0.3. Three central plots: calculated uplift rate histories. Right-hand plot: residual misfit plotted as function of m for changing values of v. Red circle = global minimum at $m = 0.2$ and $v = 120$. (h–n) Covariation of n, m and v. Plots organized as before. Colored contour plot of residual misfit as function of n, m and v. (o–u) Variation of κ by 7 orders of magnitude. (v–ab) Variation of A between $0.5A$ and $1.5A$. (ac–ai) Variation of river profile lengthing by −20 to + 50 km at river mouth.

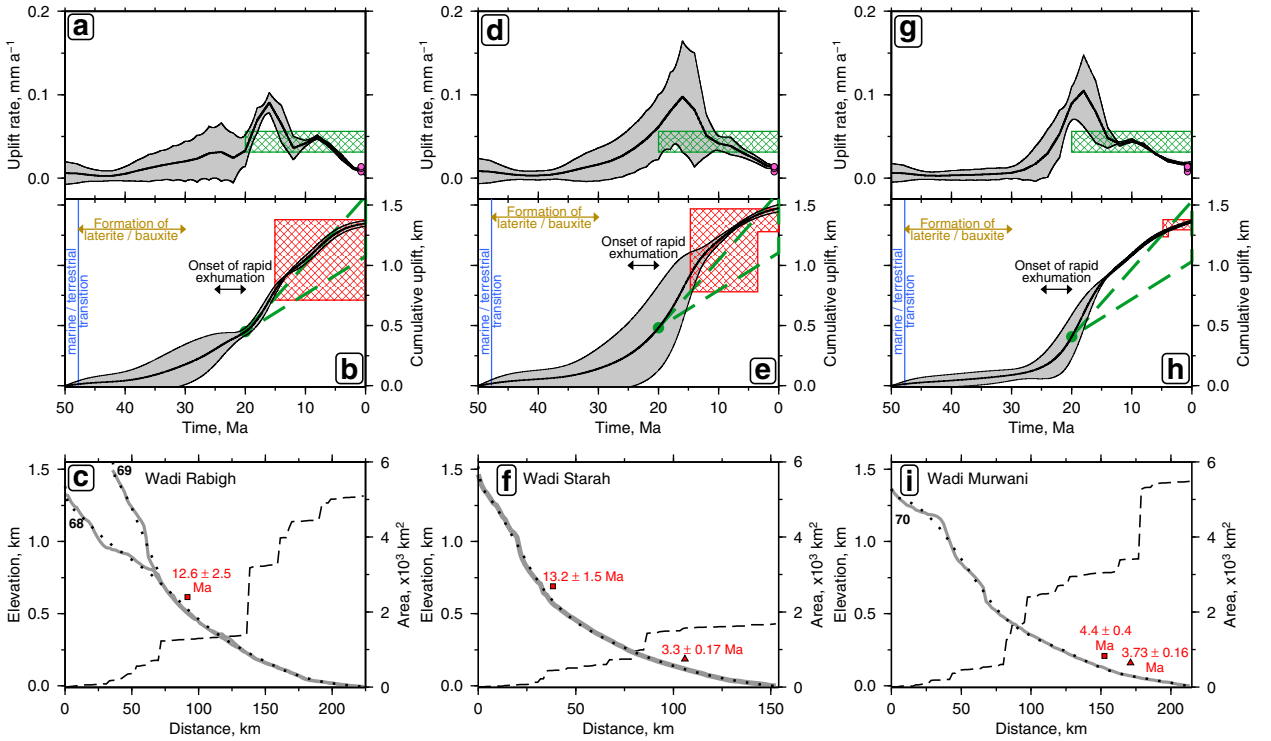

Figure 13. Inverse modeling of profiles from Wadis Rabigh, Starah, and Murwani. Each profile was inverted 50 times with erosional parameters assigned values within ranges ($2\times10^2 \le \kappa \le 5\times10^2$, $0.133 \le v \le 6239$, $0.02 \le m \le 0.51$, $1 \le n \le 1.05$). (a) Solid line with gray band = uplift rate history and one σ uncertainty from varying erosional parameters that yield best fit with profile; pink circles and error bars = present-day uplift rates from U/Th dating of emergent marine terraces [*Dawood et al.*, 2013]; green hatched area = uplift rate calculated from estimates of denudation rate [*Bohannon et al.*, 1989]. (b) Solid line and gray band = cumulative uplift history and one σ uncertainty (i.e., $\int_0^t Udt$); red polygon = minimum uplift from height of basalt flows [*Coleman et al.*, 1983; *Hussain and Bakor*, 1989]; black arrow = onset of rapid cooling from apatite fission track measurements [*Bohannon et al.*, 1989; *Menzies et al.*, 1997]; brown arrow = paleosol formation whose cessation is marked by age of oldest overlying basalt [*Coleman et al.*, 1983]; blue line = marine/terrestrial transition [*Şengör*, 2001]; dashed green line and circle = uplift calculated from estimates of denuation [*Bohannon et al.*, 1989]. (c) Gray numbered lines = observed Wadi Rabigh profiles; dashed line = upstream drainage area; dotted lines = best-fitting calculated profiles from inverse modeling; red squares = present-day elevation of K-Ar dates from lava flows [*Coleman et al.*, 1983]; red triangles = $^{40}Ar/^{39}Ar$ dates from lava flows [*Hussain and Bakor*, 1989]. (d–f) Inverse modeling of Wadi Starah profile. (g–i) Inverse modeling of Wadi Murwani profile.

resolve uplift histories back to at least 50 Ma. Smooth distributions of *U(x,y,t)* that minimize the misfit between observed and calculated river profiles can be now sought within this timespan.

We jointly inverted 225 river profiles as a function of uplift rate history over 50 Ma. The residual misfit, χ^2, between all observed and calculated river profiles decreases from 24 to 4.6 during optimization. Figure 16 shows observed and calculated river profiles from four major catchments where χ^2 is 2.5–5.9. The largest residual misfits occur for the internally draining Jordan catchment (e.g., Figure 16d). Other discrepancies are partly a consequence of the coarse grid spacing. Our algorithm is not designed to fit the shortest wavelength elevation changes caused by sharp (i.e., lithologically controlled) knickpoints. Nevertheless, height discrepancies between observed and predicted profiles throughout the Arabian Peninsula are rarely more than several hundred meters (Figure 16b).

A cumulative uplift history of the Arabian Peninsula (i.e., $\int_0^t U(x,y,t)dt$) is presented (Figure 17). This history suggests that the western Arabian Peninsula experienced significant regional uplift during the last 25–30 Ma at a rate of up to ~0.1 mm a^{-1}. Earliest uplift occurred in Yemen where two discrete phases of uplift at 30–25 and 15–10 Ma are predicted. Our model suggests that topographic growth migrated northward with younger uplift of the Sinai Peninsula. This shift is consistent with the location and age of three principal centers of magmatism (Figure 1) [*Camp and Roobol*, 1992]. Differences between present-day cumulative uplift and a surface envelope fitted to the loci of drainage divides are small (compare Figures 17k–17l). This match indicates that we can resolve the main features of landscape growth.

An ability to fit large numbers of river profiles using an uplift history that smoothly varies through time and space is surprising. It suggests that drainage inventories have systematic distributions of knickzones which

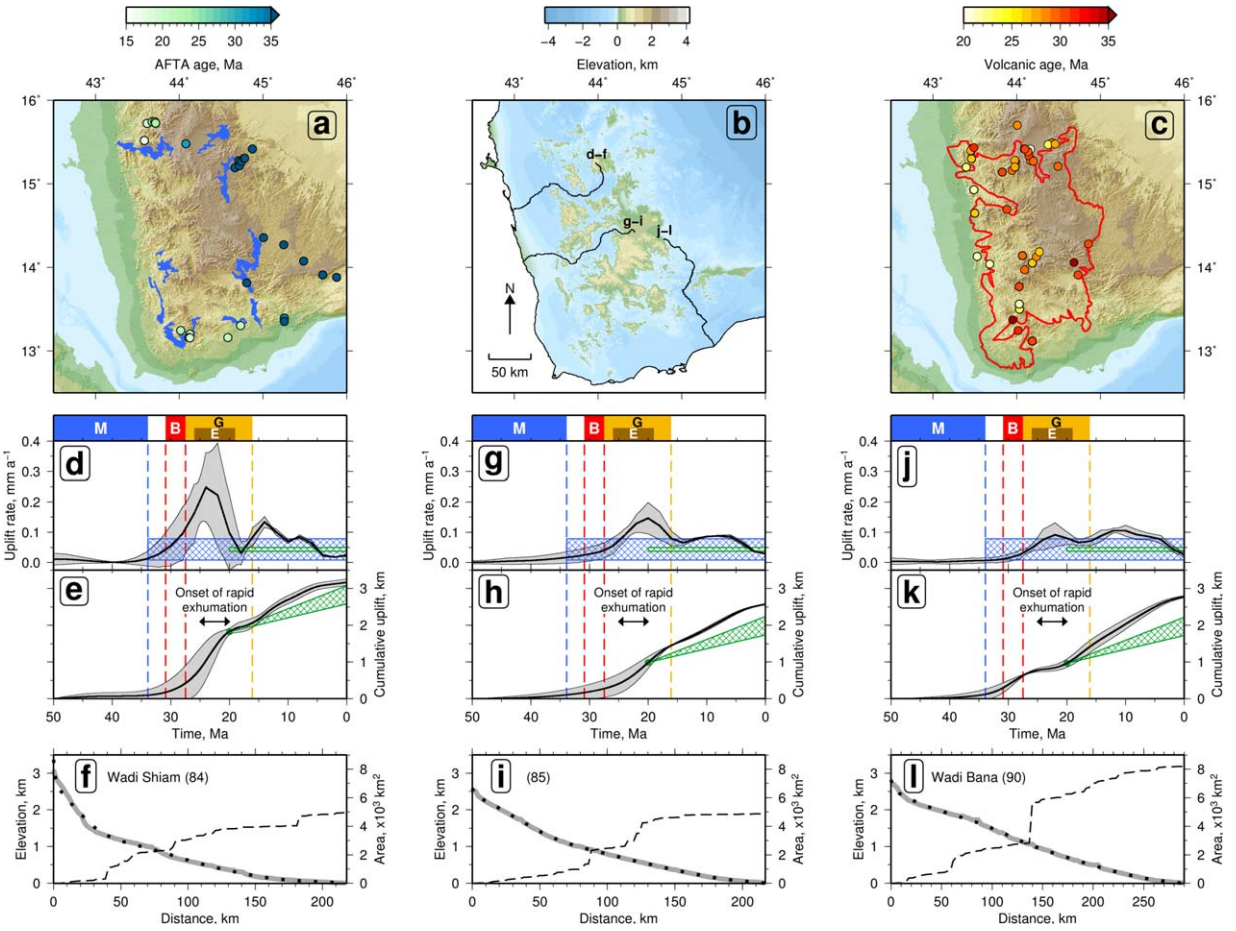

Figure 14. Inverse modeling of Yemeni profiles compared with independent geologic constraints. (a) Topographic map centered on Yemeni basaltic province; blue polygons = outcrop of shallow marine sedimentary rocks of Twailah Group [*Al-Subbary et al.*, 1998]; colored circles = apatite fission track ages [*Menzies et al.*, 1997]. (b) Paleo-elevation map at > 34 Ma; solid lines = modeled river profiles. (c) Topographic map centered on Yemeni basaltic province; red line delimits basalt outcrop; colored circles = $^{40}Ar/^{39}Ar$ ages [*Baker et al.*, 1996; *Riisager et al.*, 2005]. (d–l) Inverse modeling of profiles. Each was inverted 50 times with erosional parameters assigned values within ranges ($2\times10^2 \le \kappa \le 5\times10^2$, $0.133 \le v \le 6239$, $0.02 \le m \le 0.51$, $1 \le n \le 1.05$). (d–f) Wadi Shiam. Top; color bar and dashed lines = independent uplift estimates; M = marine fauna of Twailah Group [*Al-Subbary et al.*, 1998]; B = eruption of basalts [*Baker et al.*, 1996; *Riisager et al.*, 2005]; G = granitic intrusions [*Menzies et al.*, 1997]; E = erosion of basaltic flows [*Menzies et al.*, 1997]. Solid line and gray band = uplift rate history with one σ uncertainty from varying erosional parameters that yields best fit between observed and calculated profiles; blue polygon = average uplift rate from elevation of Eocene marine sedimentary rocks; green polygon = average uplift rate determined from denudation rates [*Menzies et al.*, 1997]. Middle: solid line and gray band = cumulative uplift history with one σ uncertainty (i.e., $\int_0^t Udt$); green polygon = uplift calculated from estimates of denudation [*Menzies et al.*, 1997]; black arrow = onset of rapid cooling from apatite fission track measurements [*Menzies et al.*, 1997]. Bottom: gray line = observed river profile; dashed line = upstream drainage area; dotted line = best-fitting calculated river profile. (g–i) Inverse modeling of profile 85. (j–l) Inverse modeling of Wadi Bana profile.

reflect a coordinated, albeit nonlinear, response to regional uplift. Short (< 500 km) profiles draining westward into the Red Sea are often irregularly shaped with prominent knickzones since uplift events were inserted at or close to sea level. The upstream reaches of longer (> 1200 km) profiles draining eastward into the Persian Gulf are also disequilibrated. This observation is consistent with insertion of uplift events into the upper parts of these catchments (i.e., not at the coastline). In other words, east and west-draining catchments respond in different ways to asymmetric uplift. This coherent response enables the inverse algorithm to simultaneously fit substantial drainage inventories with smooth uplift rate histories.

Continuing subsidence of the Persian Gulf implies that mouths of rivers draining into this depression could have originated at the Straits of Hormuz [*Sarnthein*, 1972; *Uchupi et al.*, 1999]. Sand provenance studies suggest that the gulf was exposed during Pleistocene lowstands [*Garzanti et al.*, 2013]. It is straightforward to investigate the implications of possible increases in drainage area(s) and river length(s). In Figures 12a–12i, we showed that changes in river length do affect our results, albeit in a minor way, when uplift varies as a function of time alone. We can also test the effect of extending the lengths of all rivers to their putative lowstand positions. This modified drainage inventory is then inverted (Figure 18b). The resultant uplift history does not significantly alter our principal conclusions.

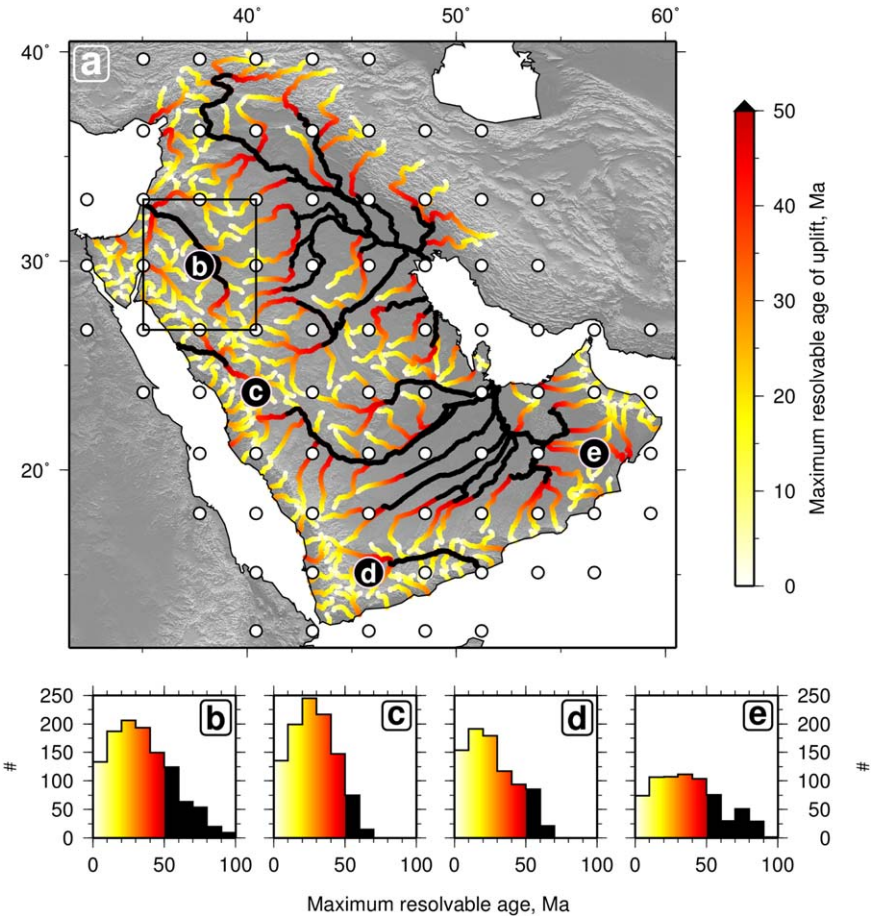

Figure 15. Spatial distribution of maximum resolvable age of notional uplift event. (a) Colored network = values of τ_G along individual river channels; white circles = $U(x, y)$ grid vertices. (b–e) Histograms of maximum resolvable ages within four boxes adjacent to vertices b–e.

Our approach is predicated upon the existence of spatial and temporal patterns of incision across the Arabian Peninsula. These patterns can be reconstructed from our calculated history (Figure 19). At successive time steps, river profiles are calculated for the last 50 Ma. Areal differences between current and previous profiles represent the volume of material removed. We conclude that Arabian rivers have been incised over this period of time, which implies that uplift rate histories are resolvable. *Paul et al.* [2014] have shown that incision history can be used to estimate cumulative sedimentary flux.

4.6. Precipitation

Equation (2) assumes that discharge does not vary with time. Average discharge along a river profile is regarded as a function of upstream drainage area alone. Instantaneous discharge is a function of temporal and spatial changes in precipitation. Since equation (1) has an integral solution, average (i.e., integrated) discharge may be more significant than instantaneous discharge. Unfortunately, we do not know how average discharge varies on geologic time scales.

At the present day, mean annual rainfall across Arabia is about 120 mm a^{-1}, varying from 40 to 80 mm a^{-1} in Rub Al-Khali to >150 mm a^{-1} in Yemen [*Fleitmann et al.*, 2011; *Almazouri et al.*, 2012]. Present-day aridity of the peninsula contrasts dramatically with elevated precipitation rates inferred for the Holocene and Pleistocene pluvial periods using $\delta^{18}O$ records from stalagmites (e.g., >300–350 mm yr^{-1}) [*Fleitmann et al.*, 2011]. These speleologic records show that precipitation is strongly modulated by orbital precession [*Cheng et al.*, 2009]. Offshore, terrigenous dust records from marine sedimentary rocks in the Gulf of Aden have been used to reconstruct Pleistocene precipitation rates [*Clemens and Prell*, 2003]. These records also demonstrate that precessionally driven changes in high summer insolation set the pacing for humid-arid cyclicity.

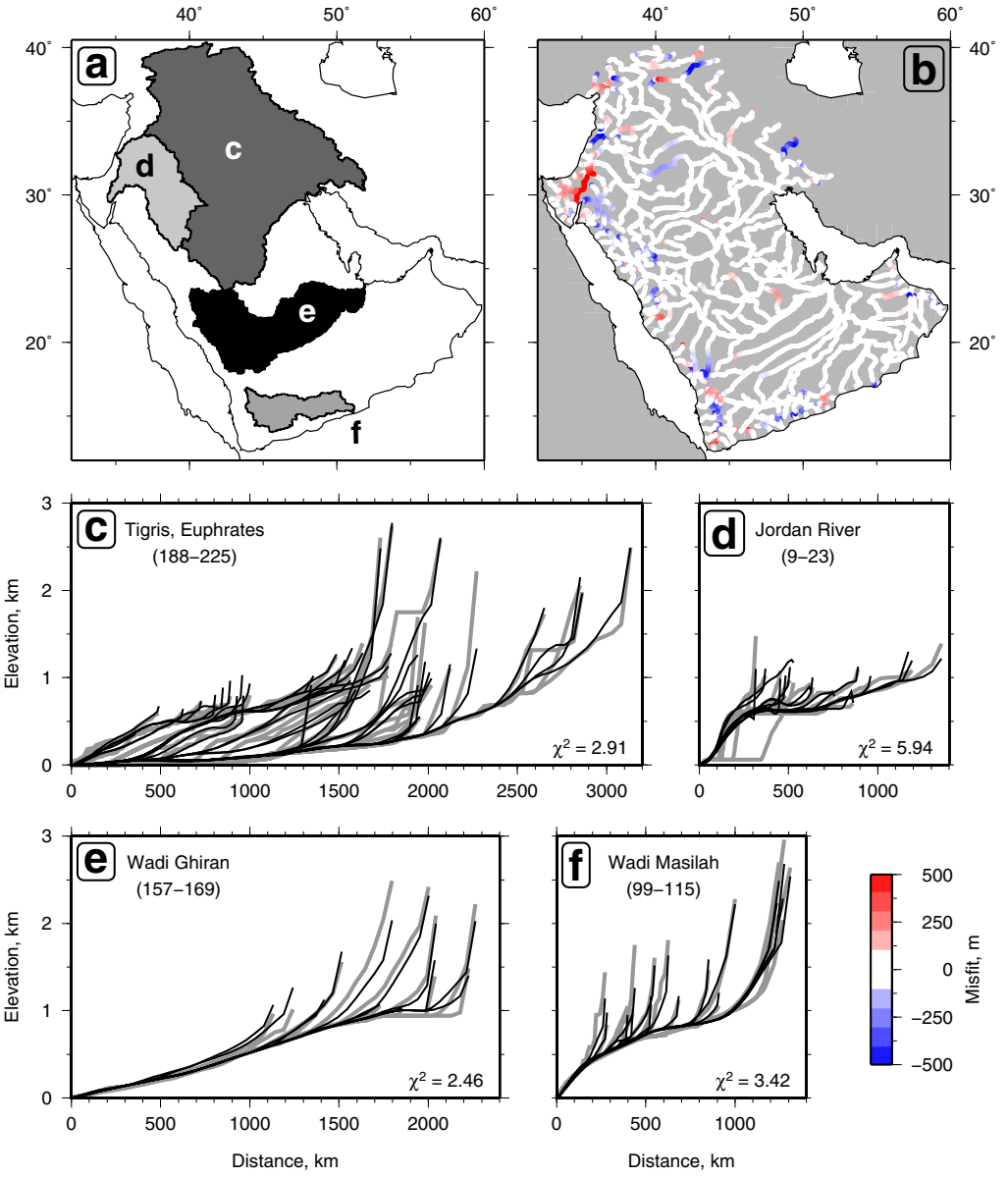

Figure 16. Observed and calculated profiles. (a) Four principal catchments of Arabian Peninsula. (b) Spatial variation of residual misfit between observed and calculated profiles (scale at bottom right-hand side). (c–f) Gray/black lines = observed/calculated profiles.

Reconstruction of Late Cretaceous paleolatitude suggests that the Arabian plate sat close to the equator [*Parish et al.*, 1982]. At this time, high levels of rainfall occurred across Arabia, attributable to surrounding warm waters of the Tethyan Ocean [*Parish et al.*, 1982; *Maley*, 1996]. Northward drift of the plate during Cenozoic times repositioned it within a band of tropical atmospheric circulation. By Middle Eocene times, the plate was close to its present location and thick layers of laterite accumulated under humid tropical conditions [*Bohannon*, 1987; *Tardy et al.*, 1991]. During Miocene times, vertebrate fauna and palynological evidence suggest Arabia had a warm, humid climate with seasonal rainfall [*Whybrow and McClure*, 1981]. Continent-scale changes in precipitation occurred during Late Neogene times which have been attributed both to a decrease in atmospheric CO_2 and to the onset of icehouse-greenhouse conditions [*Cerling et al.*, 1997; *Demenocal*, 2004]. It is speculated that regional uplift triggered reorganization of atmospheric circulation, engendering aridification of northeast Africa [*Sepulchre et al.*, 2006].

These incomplete and qualitative precipitation records cannot easily be used to quantify temporal and spatial changes in discharge across the peninsula. However, they form a useful basis for investigating how

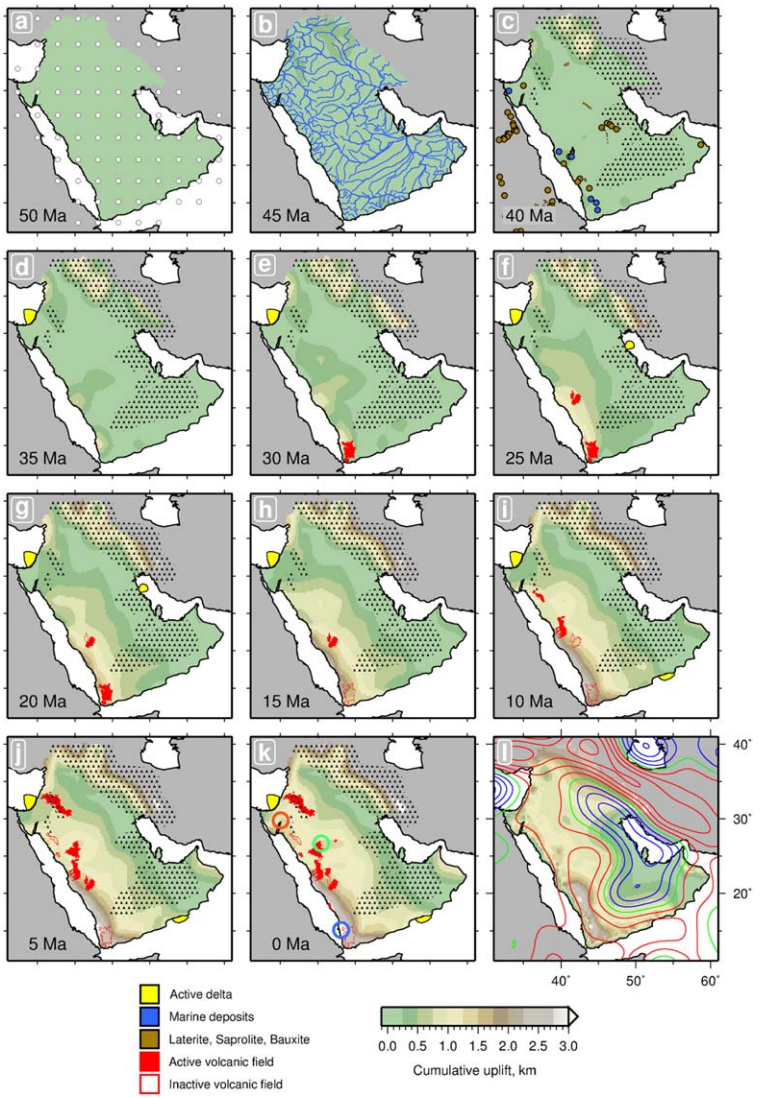

Figure 17. Calculated cumulative uplift (i.e., $\int_0^t Udt$) as function of space and time from 50 Ma to present day. (a) Circles = spatial distribution of grid points. (b) blue network = 225 rivers used in this study. (c) brown circles/polygons = loci of laterite/saprolite/bauxite deposits [*Abdulkader*, 1979; *Hopson et al*., 1981; *Schmidt et al*., 1983; *Bohannon*, 1987; *Pallister*, 1987; *Bohannon et al*., 1989; *Roger et al*., 1989; *Gow and Lozej*, 1993; *Drury et al*., 1994; *Collenette and Grainger*, 1994; *Alsharhan and Nasir*, 1996; *Schwarz and Germann*, 1999; *Babalola et al*., 2003; *Al-Bassam*, 2005]; blue circles = loci of marine deposits [*Madden et al*., 1995; *Al-Subbary et al*., 1998; *Farouk and Faris*, 2012; *Taj*, 2013]; dotted pattern = regions where calculated uplift rate history may be unreliable (poor drainage recovery). (e–k) Solid red polygons = active volcanic fields (i.e., harrats); open red polygons = inactive volcanic fields; colored circles = nodes at which uplift history is shown in Figure 23; yellow patches = clastic deltaic deposits [*Şengör*, 2001; *Bache et al*., 2011; *Steinberg et al*., 2011]. (l) Surface draped over loci of drainage divides contoured using continuous curvature method [*Smith and Wessel*, 1990]. Red/blue/green contours = positive/negative/zero contours at 250 m intervals of dynamic topography calculated by dividing long wavelength free-air gravity by $Z = 50$ mGal km^{-1}.

different periodicities and amplitudes of precipitation rate potentially affect our results. Following *Roe et al*. [2002] and *Wu et al*. [2006], equation (2) is recast as

$$E(x,t) = -v_\circ Q^m \frac{\partial z}{\partial x} \tag{5}$$

where $Q(x,t) = p(t) \times A(x)$ is discharge as a function of time and distance along a river, and $p(t)$ is the rate of precipitation. We will assume that

$$p(t) = p_\circ + S \sin(2\pi\omega t), \tag{6}$$

where ω is frequency, $p_\circ$ and S are constants whose values are chosen to ensure that $p(t) \geq 0$ (i.e., $p_\circ \geq S$). In Figure 20, we have inverted three river profiles from the Harrat Rahat region to investigate how different

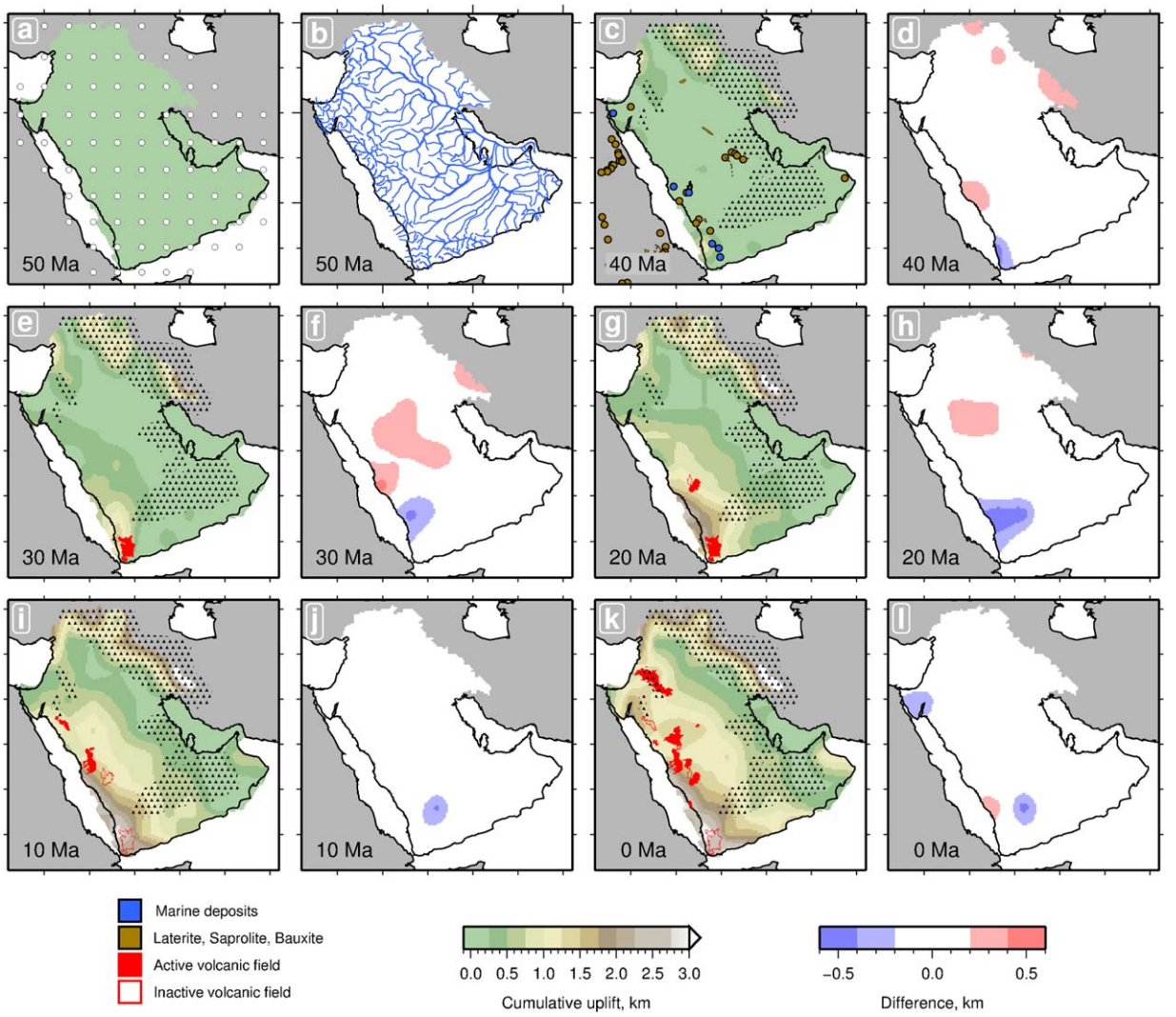

Figure 18. Calculated cumulative uplift for lowstand drainage network (i.e., $\int_0^t U(x,y,t)dt$) as function of space and time from 50 Ma to present day. (c) blue circles = loci of marine deposits [*Madden et al.*, 1995; *Al-Subbary et al.*, 1998; *Farouk and Faris*, 2012; *Taj*, 2013]; brown circles = loci of laterite/saprolite/bauxite deposits [*Abdulkader*, 1979; *Hopson et al.*, 1981; *Schmidt et al.*, 1983; *Bohannon*, 1987; *Pallister*, 1987; *Bohannon et al.*, 1989; *Roger et al.*, 1989; *Gow and Lozej*, 1993; *Drury et al.*, 1994; *Collenette and Grainger*, 1994; *Alsharhan and Nasir*, 1996; *Schwarz and Germann*, 1999; *Babalola et al.*, 2003; *Al-Bassam*, 2005]; dotted pattern = regions where recovered uplift history may be less reliable. (e, g, i, k) Solid red polygons = active volcanic fields; open red polygons = inactive volcanic fields. (b) Rivers have been lengthened out to Straits of Hormuz to simulate low stand of sea level. (d, f, h, j, l) Difference between cumulative uplift histories shown here and in Figure 17.

histories of precipitation affect one-dimensional uplift rate histories. In each case, $v_\circ$ was chosen to ensure that $vA^m \approx v_\circ Q^m$ when $p(t)=p_\circ$. Precipitation rates vary from 0 to 12000 mm a^{-1} with periods which range from 0.1 to 30 Ma. These values were chosen to reflect the likely range of post-Eocene precipitation rates, including present-day extrema [*Feakins and Demenocal*, 2008; *Fleitmann et al.*, 2011; *Milliman and Farnsworth*, 2011]. Recovered uplift histories are essentially identical if precipitation varies with periods of < 1 Ma. Thus orbital forcing of arid-humid cyclicity does not significantly affect our calculated uplift histories. Longer period precipitation changes are more influential since knickzone retreat velocities can be affected for longer durations. For example, in a dry-wet-dry precipitation cycle, lasting 50 Ma, observed and predicted profiles agree but peak uplift rate is shifted backward. In a wet-dry-wet cycle, peak uplift rate is shifted forward. These time shifts are small given large excursions of precipitation. Similar results are obtained when different precipitation models were used to invert the whole drainage inventory as a function of space and time (Figure 21).

5. Regional Tests

Our results predict the spatial and temporal pattern of regional uplift in regions far from the calibration location at Harrat Rahat (Figure 17). These locally derived erosional parameters were tested using

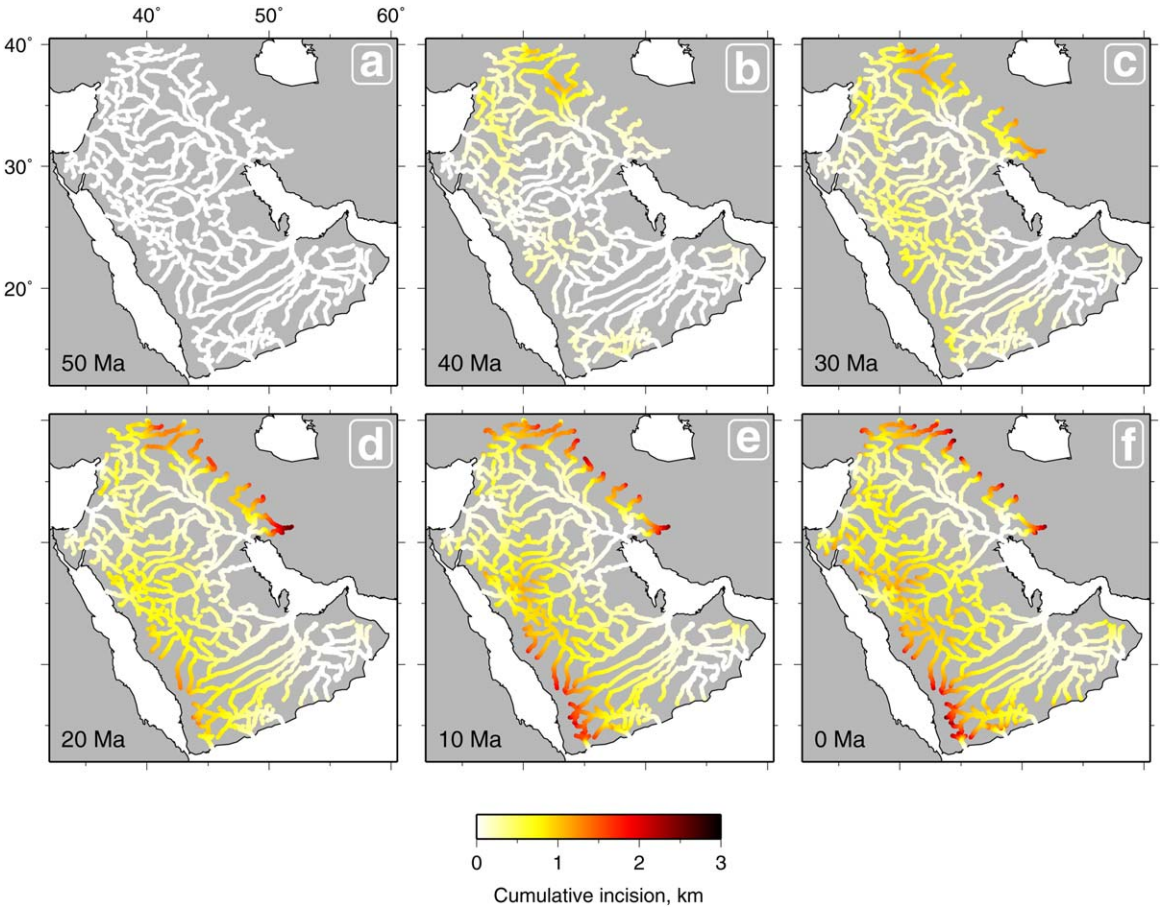

Figure 19. Calculated cumulative incision of Arabian drainage network between 50 Ma and present day.

stratigraphic constraints at the southern end of the peninsula. Here we compare our predictions with a range of more distal geologic and geophysical observations. These comparisons are important independent tests.

5.1. Quaternary Uplift Rates

The Red Sea coastal plain is characterized by emergent marine terraces at elevations of 6–30 m [*Brown et al.*, 1989]. Between 13 and 23° N, an emergent coral reef at ~ 3 m elevation has yielded a $^{230}Th/^{234}U$ age of 135 ka [*Brown et al.*, 1989]. At Rabigh, reef deposits at 2.5–3.3 m elevation have $^{230}Th/^{234}U$ ages of 212–235 ka [*Dawood et al.*, 2013]. Narrow, deep-water channels (i.e., sharms) penetrate at right angles into the coastline between Jeddah and the Gulf of Aqaba (i.e., 22–28°N). A raised terrace incised by these sharms occurs at an elevation of ~ 12 m and has a $^{230}Th/^{234}U$ age of 146 ka [*Goldberg and Yaron*, 1978]. Collectively, these observations suggest that the coastal plain is being uplifted at rates of ~ 0.02–0.08 mm a^{-1}.

Figure 22 summarizes a catalogue of 190 uplift rates compiled from published ^{14}C and $^{239}Th/^{243}U$ dates of emergent marine terraces [*McClure and Vita-Finzi*, 1982; *Behairy*, 1983; *Purser and Höltz*, 1988; *Dullo*, 1990; *Hoang and Taviani*, 1991; *Gvirtzman et al.*, 1992; *El Moursi et al.*, 1994; *Plaziat et al.*, 1995; *Bosworth and Taviani*, 1996; *Hoang et al.*, 1996; *El Asmar*, 1997; *Carbone et al.*, 1998; *Dullo and Montaggioni*, 1998; *Walter et al.*, 2000; *Vita-Finzi*, 2001; *Hoorn and Cremaschi*, 2004; *Pirazzoli et al.*, 2004; *Plaziat et al.*, 2008; *Buffler et al.*, 2010; *Lambeck et al.*, 2011; *Leroy et al.*, 2012; *Wood et al.*, 2012; *Dawood et al.*, 2013]. This compilation includes terraces that formed during marine isotope stage 5e, when sea level may have been 4–6 m higher than its present-day value [*Chappell and Shackleton*, 1986; *Zhu et al.*, 1993; *Lambeck and Chappell*, 2001; *Shackleton et al.*, 2003]. Critically, elevation of these coeval terraces varies along the coastline which implies that uplift rate is not constant (Figure 22d). Modern rates of uplift are typically 0.1–0.4 mm a^{-1}, consistent with our calculated rates (Figure 22e). Rates decrease from south to north along the Red Sea, corresponding

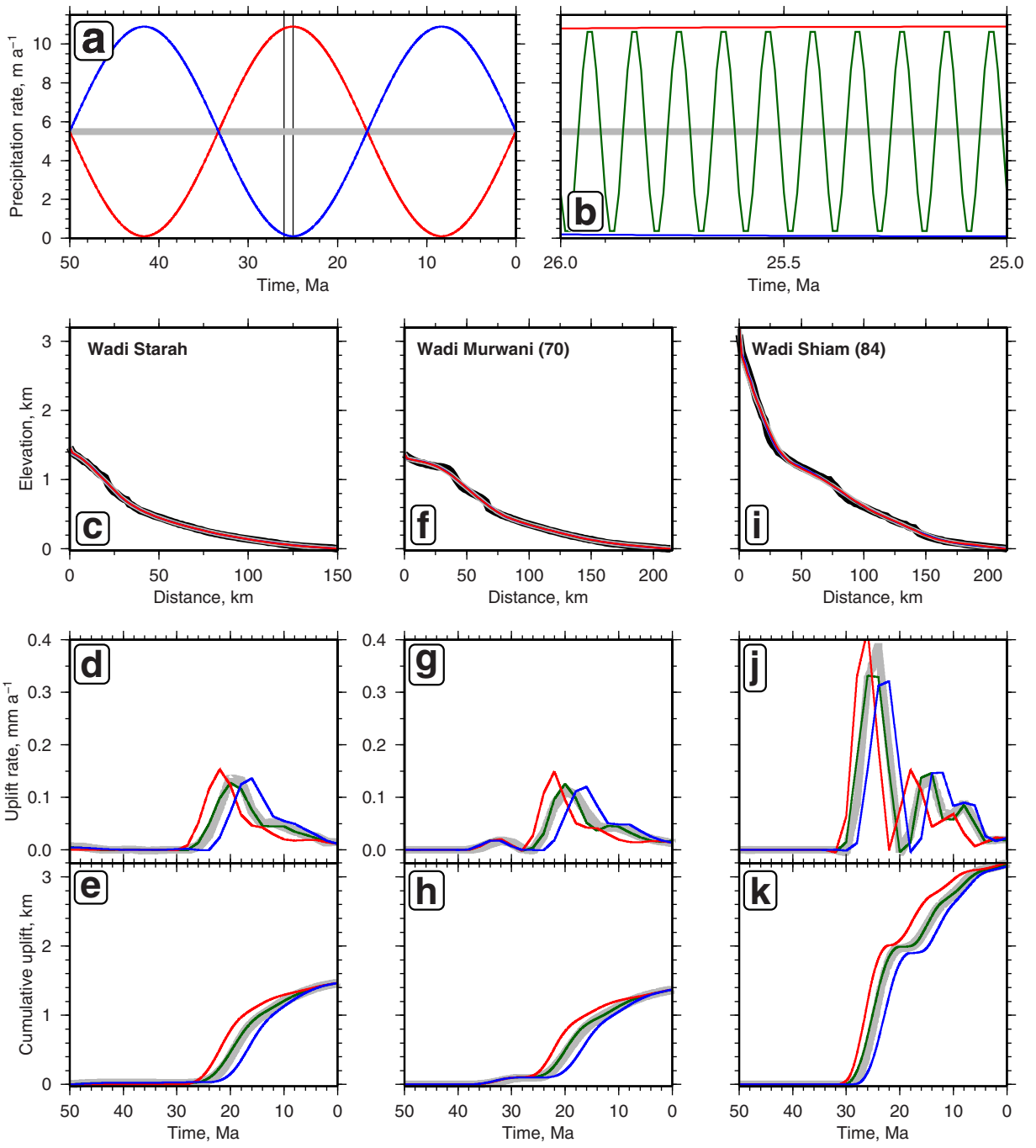

Figure 20. One-dimensional precipitation tests. (a, b) Precipitation rate as function of time; blue line = wet-dry-wet cycle with frequency of 0.03 Ma^{-1}; red line = dry-wet-dry cycle with frequency of 0.03 Ma^{-1}; green line = cycle with frequency of 0.1 Ma^{-1}; gray band = constant precipitation model. (c) Wadi Starah profile. Black line = observed profile; red/blue/green/gray lines = best-fitting calculated profiles for four precipitation models shown in Figures 20a and 20b. (d) Gray band = calculated uplift rate history for constant precipitation model; red/green/blue lines = calculated uplift rate history where color corresponds to precipitation models shown in Figures 20a and 20b. (e) Gray band = calculated cumulative uplift history for constant precipitation model; red/green/blue lines = calculated cumulative uplift histories where color corresponds to precipitation models shown in Figures 20a and 20b. (f–h) Inverse modeling of Wadi Murwani with varying precipitation rate. (i–k) Inverse modeling of Wadi Shaim with varying precipitaton rate.

with a gradual deviation of the main drainage divide away from the coastline. Thus uplift rate is greatest proximal to the continental drainage divide.

5.2. Stratigraphic and Geomorphic Observations

The coastal plain merges eastward into an erosional pediment that culminates in the Red Sea escarpment. This escarpment rises to elevations of 2.6 km and cuts into rims of the great interior plateaux (Figure 6c).

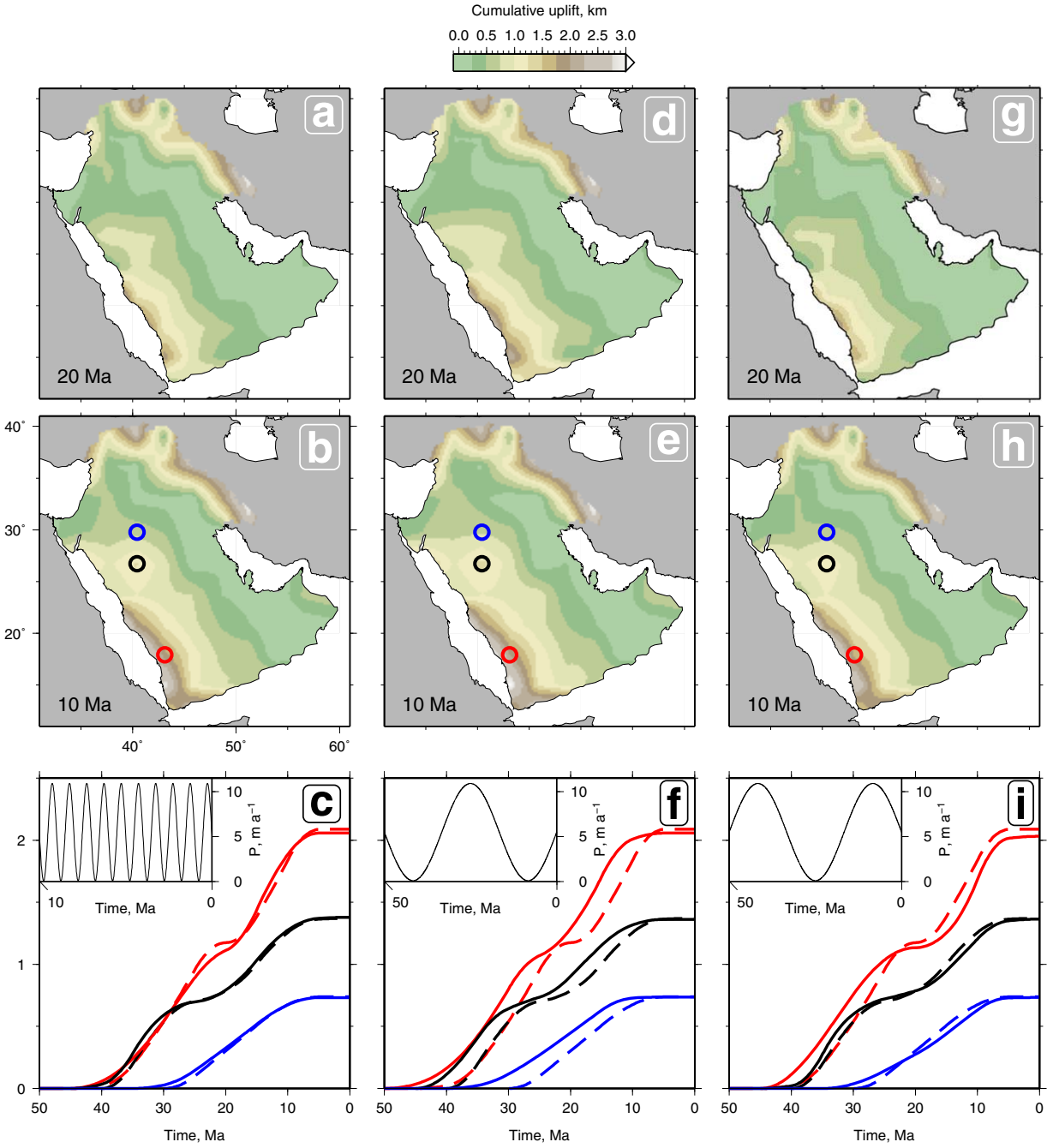

Figure 21. Two-dimensional precipitation tests. (a, b) Calculated cumulative uplift histories at 20 and 10 Ma for which precipitation rate varies with frequency of 1 Ma^{-1}. Histories at blue/black/red nodes shown below. (c) Comparison between cumulative uplift histories at each colored node. Solid lines = varying precipitation model; dashed lines = constant precipitation model; inset shows variation in precipitation. (d–f) Dry-wet-dry preciptation model with frequency of 0.03 Ma^{-1}. (g–i) Wet-dry-wet precipitation model with frequency of 0.03 Ma^{-1}.

The distribution and morphology of these plateaux place limits on the history of uplift. The Najd or central Arabian peneplain is a mature, low relief surface that developed on top of the Precambrian shield [*Brown and Jackson*, 1960; *Chapman*, 1978; *Brown et al.*, 1989; *Salpeteur and Sebir*, 1989]. Cretaceous laterites were eroded during exhumation of this peneplain and sparse evidence for these deposits is preserved beneath basaltic rocks (e.g., Harrat As Sirat where basalts overlie $\sim$ 1000 km^2 of saprolitic deposits). Many of these deeply incised and dissected deposits are $\sim$ 30 Ma (Figure 17c) [*Coleman et al.*, 1983].

Young marine deposits of the Usfan and Umm Himar Formations rest unconformably on basement rocks [*Brown et al.*, 1989; *Madden et al.*, 1995]. These shallow water limestones are Middle Eocene vestiges of the

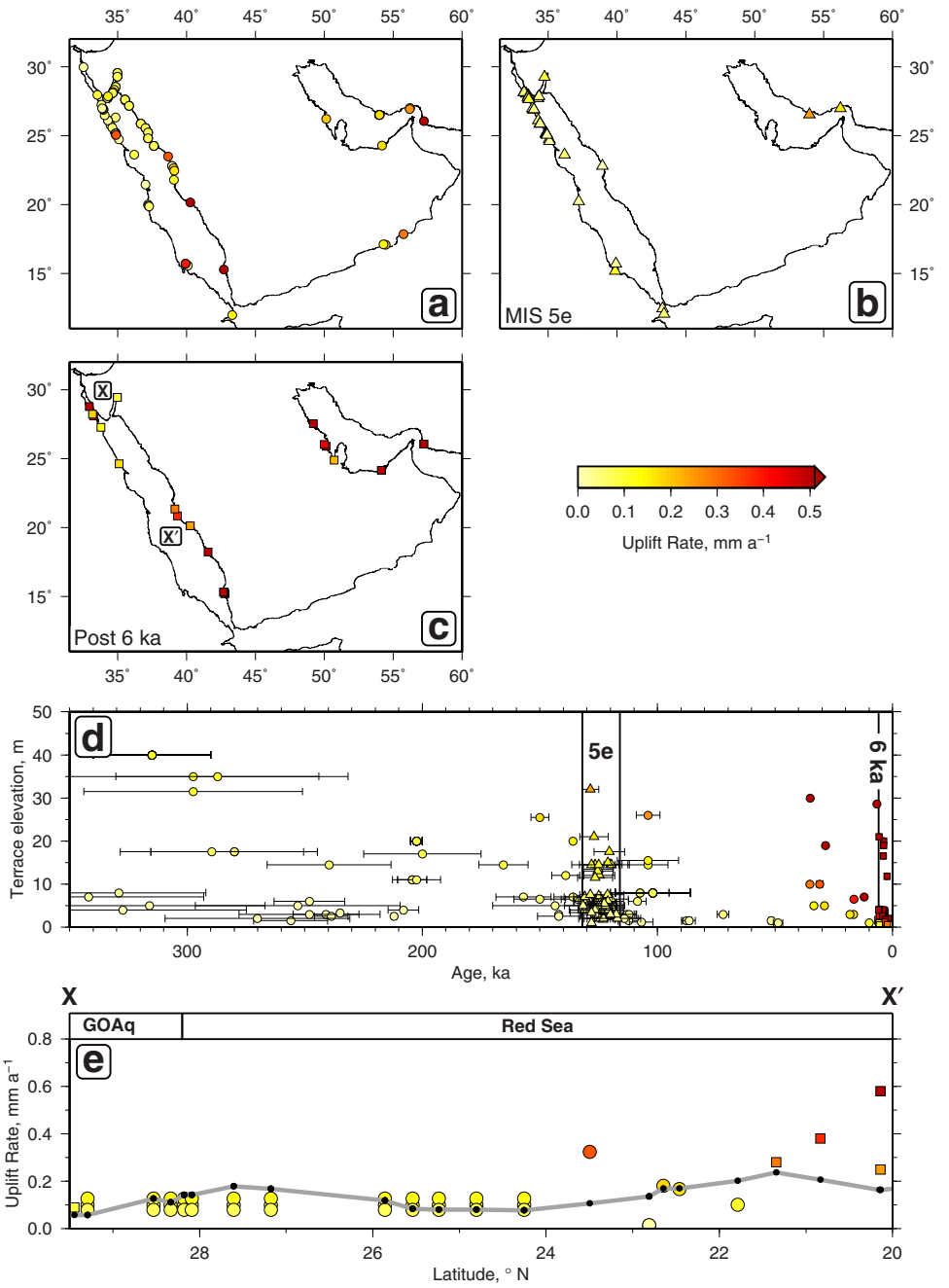

Figure 22. Uplift rates from marine terraces. (a) Circles = uplift rates of terraces formed during intermediate sea-level stands (i.e., not post-6 ka or marine isotope stage 5e). (b) Triangles = uplift rates of terraces formed during marine isotope stage (MIS) 5e. (c) Squares = uplift rates of terraces formed since stabilization of sea level at 6 ka. (d) Terrace elevation as function of age. Vertical lines = MIS 5e and 6 ka; Circles/triangles/squares as before. (e) Uplift rate as function of latitude (see Figure 22a for location). Circles/squares as before; gray line and circles = calculated uplift rate from inverse modeling of drainage.

Tethyan Ocean [*Kluyver et al.*, 1981]. Paleontologic evidence suggests a Paleocene to Middle Eocene age for the Usfan Formation. This estimate is supported by K-Ar ages of 43.7 ± 1 Ma and 56.4 ± 1.2 Ma obtained from glauconitic deposits [*Brown et al.*, 1989]. Vertebrate fossils (e.g., sharks, rays, fish, turtles) from the Umm Himar Formation yield Middle Paleocene ages [*Madden et al.*, 1980, 1995]. Late Oligocene basaltic flows with K-Ar ages of 27.8 ± 1.4 and 26.6 ± 1.3 Ma overlie this formation [*Arno et al.*, 1980]. In western Yemen, a Paleogene sandstone of the Twailah Group known as the Medj-zir Formation is reported to contain rare benthic foraminifera and gastropods (*Orbitulina discoidea*, *Tarebia* and *Coptostylus*) [*Al-Subbary et al.*, 1998; *Al-Qayim et al.*, 2005]. 10–30 m thick ferruginous paleosols overlie the Medj-zir Formation. These

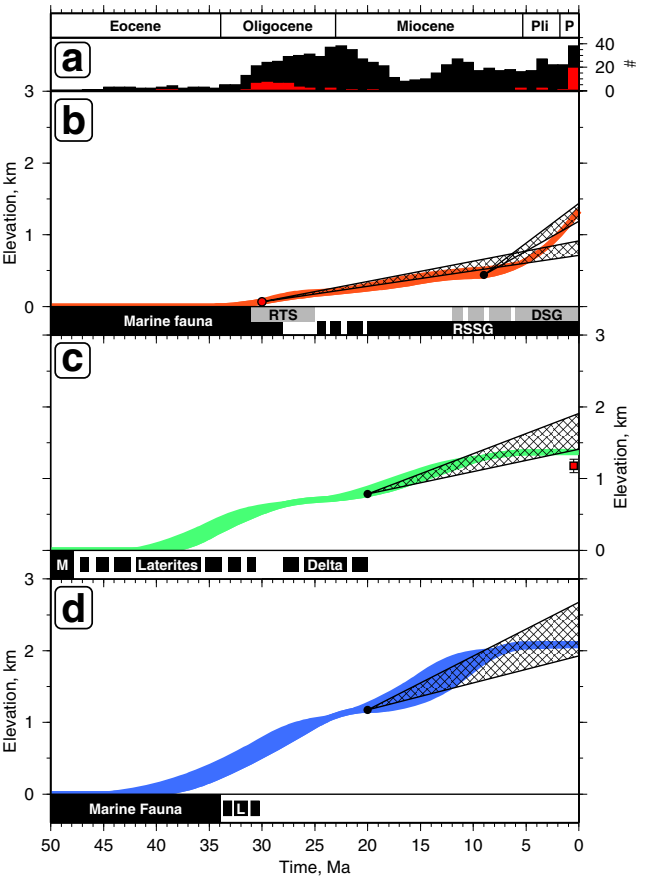

Figure 23. Comparison between calculated cumulative uplift histories and independent constraints at three locations shown on Figure 17k. (a) Magmatism. Red bars = $^{40}Ar/^{39}Ar$ ages [*Hussain and Bakor*, 1989; *Sebai et al.*, 1991; *Baker et al.*, 1996; *Coulié et al.*, 2003; *Krienitz et al.*, 2009; *Moufti et al.*, 2013; *Riisager et al.*, 2005]; black bars = K-Ar ages [*Civetta et al.*, 1978; *Coleman et al.*, 1983; *Pallister*, 1987; *Capaldi et al.*, 1987; *Chisea et al.*, 1988; *Camp and Roobol*, 1989; *Brown et al.*, 1989; *du Bray et al.*, 1991; *Trifonov et al.*, 2010; *Al-Kwatil et al.*, 2012]. (b) Sinai where orange band = calculated cumulative uplift history (width reflects long period variation of precipitation rate); black circle/hatching = uplift estimated from denudation measurements [*Kohn and Eyal*, 1981]; red circle/black hatching = uplift estimated from denudation measurements [*Feinstein et al.*, 2013]; age range of marine fauna from Thebes Formation [*Garfunkel*, 1988; *Farouk and Faris*, 2012]; RTS/RSSG/DSG = regional truncation surface/Red Sea Supergroup/Dead Sea Group [*Avni et al.*, 2012]. (c) Western Arabian Swell where green band = calculated cumulative uplift history; black hatching = uplift estimated from denudation measurements [*Bohannon et al.*, 1989]; red square with error bar = air-loaded residual topography from adjacent Red Sea; M = marine fauna of Usfan and Umm Himar formations [*Kluyver et al.*, 1981; *Madden et al.*, 1995; *Şengör*, 2001; *Taj*, 2013]; cessation of laterites constrained by age of oldest overlying basalt [*Coleman et al.*, 1983]; appearance of the Ahwaz delta [*Şengör*, 2001]. (d) Yemen where blue band = cumulative uplift history; black hatching = uplift estimated from denudation measurements [*Menzies et al.*, 1997]; age range of marine fauna from Twailah Group [*Al-Subbary et al.*, 1998].

stratal relationships suggest that a significant period of low-relief exposure (e.g., > 1 Ma) followed marine deposition [*Kraus and Brown*, 1986; *Wright*, 1994; *Al-Subbary et al.*, 1998]. Lava flows from the Yemeni volcanic group conformably overlie these paleosol horizons [*Baker et al.*, 1996].

The development of widespread incision can also be constrained. First, iron-rich terrestrial units of the Oligocene to Early Miocene Shumashi Formation and Jizan Group suggest when erosion of saprolitic layers overlying the stable Precambrian shield began. These units do not contain Precambrian detritus [*Brown et al.*, 1989]. However, chaotic boulder conglomerates of the Early to Middle Miocene Bathan Formation contain Precambrian clasts, suggesting that lateritic layers had largely been stripped away by this time [*Hadley and Fleck*, 1980; *Brown et al.*, 1989]. Second, there is evidence that 12 Ma lava flows were deposited within thalwegs of paleochannels that drained Harrat Rahat. Their existence implies that active incision had commenced (Figure 9).

Following the pioneering observations of *Quennell* [1959], *Avni et al.* [2012] showed that a regional truncation surface developed during Oligocene times at the northern end of the Arabian Peninsula. This surface was uplifted to form the Egma Plateau. From 65 to 40 Ma, the most significant post-Jurassic marine transgression occurred. This regional stability was interrupted between 37 and 20 Ma when the Afro-Arabian dome developed, uplifting the Levantine margin. A phase of regional uplift is manifest by erosion of Upper Eocene marine sequences that were overlain by conglomerate rocks. Incised paleo-valleys cut into the resultant Oligocene peneplain and were filled with clastic deposits. For example, the Red Sea Supergroup consists of polymictic conglomerate deposits which contain clasts derived from Eocene strata down to Precambrian crystalline basement [*Avni et al.*, 2012]. Early Miocene fluvial deposits were deposited within 500–1000 m wide, and 40–50 m deep, paleovalleys that incised the regional truncation surface. These stratigraphic observations show that this region was uplifted in two phases. The first phase occurred in Oligocene times and generated the regional truncation surface. The second phase occurred during Miocene times when the regional truncation surface was uplifted and incised.

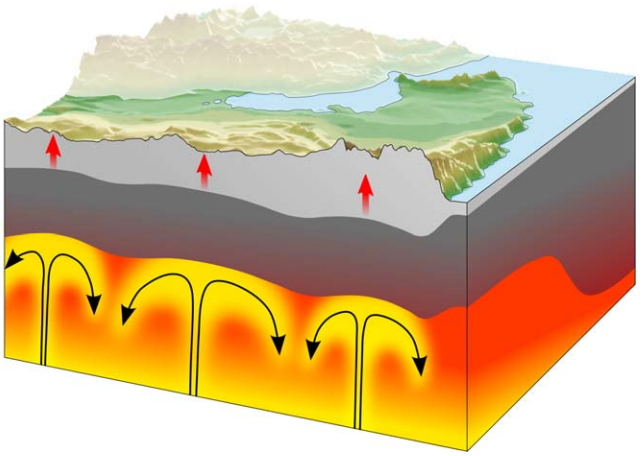

Figure 24. Cartoon of lithosphere and asthenosphere beneath Arabia. Green/brown shading = perspective topography of Arabian Peninsula; light gray shading = crust; dark gray shading = lithospheric mantle; red/yellow shading = asthenosphere with convective upwellings.

Finally, our results suggest that the Oman Mountains and Musandam Peninsula along the southwest flank of the Persian Gulf became emergent about 20 Ma (Figure 17). *Searle et al*. [2014] summarize stratigraphic observations which demonstrate that this region was shallow marine from 65 to 35 Ma. They suggest that the Oman Mountains were uplifted during Late Oligocene to Early Miocene times. A similar uplift history is inferred for the Musandam Peninsula, although geomorphic evidence from drowned terraces suggests that the tip of this peninsula resubmerged during Quaternary times. In summary, regional stratigraphic and geomorphic evidence helps to independently verify the main features of our predicted uplift history at locations far from the area used for calibration.

5.3. Magmatism

The distribution, age and composition of harrats provide useful information about the time scale of dynamic support. $^{40}Ar/^{39}Ar$ and K-Ar age measurements from basalts are shown as a function of latitude in Figure 1d. The temporal and spatial distribution suggests a northward younging trend from Afar to Syria with two main phases of volcanism [*Camp and Roobol*, 1992]. The older 32–18 Ma magmatic phase has a limited geographic distribution which is roughly parallel to the Red Sea. The younger post-14 Ma phase is more widely distributed along a north-south zone which marks the central axis of the Western Arabian swell (Figures 1 and 17). There are well-documented problems with the reliability of K-Ar dating and it is important to discriminate between K-Ar and $^{40}Ar/^{39}Ar$ ages. For example, differences between $^{40}Ar/^{39}Ar$ plateau mineral ages and whole rock K-Ar dates from Western Yemen are consistent with Ar loss [*Tabor et al*., 1985]. Despite these difficulties, the trend of age as a function of latitude appears to be robust (Figure 1; *Krienitz et al*., 2009; *Sebai et al*., 1991; *Coulié et al*., 2003].

Basaltic compositions resemble oceanic island basalts which indicates a sublithospheric source [*Camp and Roobol*, 1989; *Camp et al*., 1991, 1992; *Bertrand et al*., 2003; *Shaw et al*., 2003]. Since the composition of basic magmas is primarily controlled by that of their source regions, major, trace and rare earth elemental distributions can be inverted to obtain melt fraction as a function of depth [*McKenzie and O'Nions*, 1991; *Tainton and McKenzie*, 1994]. McKenzie and Priestley (submitted manuscript, 2014) showed that the composition of Jordanian alkali basalts are consistent with an asthenospheric temperature anomaly of $\sim 200^{\circ}$C. This anomaly is corroborated by mantle xenolithic thermobarometry [*Thornber and Pallister*, 1985; *McGuire*, 1988; *Henjes-Kunst et al*., 1990; *Nasir*, 1992]. It is also broadly consistent with a calibrated surface wave tomographic model [*Priestley et al*., 2012; McKenzie and Priestley, submitted manuscript, 2014].

The existence of an asthenospheric temperature anomaly implies a steep geothermal gradient for a typical stable continental shield. However, surface heat flow measurements from western Arabia are much lower than expected [*Gettings*, 1981; *Gettings et al*., 1986]. This discrepancy suggests that the emplacement age of the anomaly is much younger than the thermal time constant of the lithosphere (i.e., younger than 40–60 Ma).

5.4. Thermochronometry

Proterozoic rocks of Arabia were buried to depths of at least 3–4 km before Neogene times [*McGuire and Bohannon*, 1989]. Apatite fission track analyses of samples from the Red Sea coastline suggest that unroofing began in Early Oligocene ($\sim$ 34 Ma) times with increased erosion from $\sim$ 21–25 Ma [*Omar and Steckler*,

1995]. *Bohannon et al*. [1989] used fission track ages from southern Arabia to document $\geq$ 2.5−4.5 km of uplift and denudation which began at ∼20 Ma and accelerated after 14 Ma. These younger fission track ages are a result of samples having been only partially annealed prior to uplift or having been annealed and reset by nearby volcanic activity [*Ghebreab*, 1998]. In Yemen, basement amphibolites record rapid exhumational cooling by erosional unroofing that began at ∼ 25–20 Ma. This cooling marks the start of regional uplift [*Menzies et al*., 1997]. Estimates of $>$ 3 km uplift and denudation from western Yemen are consistent with 3.5–4 km of rock removal predicted for the Eritrean conjugate margin [*Menzies et al*., 1997; *Abbate et al*., 2002]. (U-Th)/He and fission track studies of eastern Yemen and of the Gulf of Aden suggest that basement rocks cooled by ∼ 80 °C within the last ∼ 40 Ma [*Pik et al*., 2013]. Further north, apatite fission track analyses from the Sinai peninsula suggest that up to 3 km of denudation occurred after 26 ±8 Ma [*Feinstein et al*., 2013]. The simplest thermal models show that cooling (i.e., denudation) was largely continuous from Oligocene times. Older studies suggest that there is evidence for a two stage history of denudation [*Omar and Steckler*, 1995]. *Kohn and Eyal* [1981] have argued that there is evidence for significant denudation after 9 Ma. This suite of thermochronometric analyses along the length of the peninsula is consistent with geologic and geomorphic evidence for post-Neogene cooling and denudation (Figure 10). 0.5–1 km of uplift occurred along the Western Arabian swell and there is some evidence, especially from the northern tip of the Gulf of Aqaba and from the Sinai Peninsula, that two phases of cooling and denudation occurred.

6. Discussion

Mechanisms of regional uplift must account for a suite of disparate observations (Figure 23). First, long wavelength free-air gravity anomalies of + 30 mGal that dominate the peninsula. Second, the distribution, age, and composition of magmatism along the western margin of the peninsula. Thirdly, crustal and lithospheric thickness variations and their isostatic consequences. Fourthly, geomorphic, stratigraphic and thermochronologic observations that are consistent with Neogene uplift and denudation. These observations are not easily accounted for by thermo-mechanical rift flank uplift models of Red Sea opening.

The small flexural rigidity suggests that topography, gravity anomalies, magmatism and the drainage pattern might collectively manifest the planform of sublithospheric convective circulation. Previously, northward migration of volcanism through time has been attributed to channeling of Afar plume material beneath Arabia [*Camp and Roobol*, 1992; *Ebinger and Sleep*, 1998]. This hypothesis is partly supported by seismic tomography models [*Hadiouche and Zurn*, 1992; *Debayle et al*., 2001; *Pasyanos and Nyblade*, 2007; *Park et al*., 2007; *Hansen et al*., 2007a; *Sicilia et al*., 2008]. *Chang and Van der Lee* [2011] carried out a combined surface and body wave study which images two quasi-cylindrical bodies with anomalously low velocities beneath Afar and Jordan. A plausible explanation is that a series of hot blobs have upwelled beneath the Lithospheric plate (Figure 24). These blobs generated topographic swells with approximately radial drainage patterns. Growth of these swells coincided with basaltic magmatism which migrated from south to north. There is some evidence from drainage patterns and stratigraphic constraints that topography grew in two phases.

Where have the erosional products of regional uplift and denudation gone? The disposition of the principal catchments suggests that the greatest volumes of clastic material were transported along the Tigris-Euphrates-Ghiran and Jordan paleo-drainage systems into the Persian Gulf and Levantine Sea, respectively. Surprisingly, there is little evidence for thick deposits of Neogene clastic sedimentary rocks in the gulf itself which suggest that much of this material has either been incorporated into the encroaching Zagros orogeny, transported into the Indian Ocean through the straits of Hormuz, or preserved along the western flank of the Persian Gulf. *Şengör* [2001] has suggested that eastward-directed drainage toward the Persian Gulf generated small paleo-deltas along the western edge of the gulf. Prior to Oligocene times, elevation of the Arabian Peninsula was minor and carbonate facies (e.g., the Umm er Radhuma Formation) have negligible terriginous content. During Oligo-Miocene times, clastic material was transported from west to east, when the Arabian Peninsula was uplifted. It is preserved within the Ahwaz Sandstone Member of the Asmari Formation and the Ghar Formation which consist of calcareous sandstones and pebbly sandstones, respectively. The sudden appearance of these facies and the lack of basaltic detritus suggests that regional uplift preceded basaltic volcanism. *Glennie* [2010] has suggested that fluvial products of erosion flowed eastward into Abu Dhabi along a paleo-drainage system. *Zilberman and Calvo* [2013] have used the erosional relics of

the Hazeva Formation, an Early Miocene fluvial sequence that crops out on the Jordanian Plateau and throughout southern Israel, to map out ancient drainage networks. Their reconstruction suggests that the northeastern flank of the Red Sea, including the Sinai Peninsula, drained into the Eastern Mediterranean Sea during Early Miocene times. Their inference is corroborated by the existence of large volumes of siliciclastic material that accumulated in the deep-water Levant Basin [*Steinberg et al.*, 2011]. Smaller catchments drain into the Gulf of Aden. For example, *Bache et al.* [2011] suggest that sedimentary deposition along the Dhofar margin was caused by Middle Miocene to Pliocene uplift and erosion of the Dhofar mountains.

7. Conclusions

We have calculated a smooth uplift rate history for the Arabian Peninsula by inverting a drainage inventory consisting of 225 river profiles. Our inverse strategy is predicated upon an empirical model which uses a nonlinear advective-diffusive formulation to match the shapes of river profiles. A trade-off relationship between the most important erosional parameters was determined using estimates of incision rate from Harrat Rahat, located half-way down the Red Sea's eastern flank. During optimization, χ^2 decreases from 24 to 5. Calculated uplift rate histories imply that the western half of the Arabian Peninsula was uplifted within the last $\sim$ 30 Ma. There is some evidence that this regional uplift occurred in two stages. The predicted uplift history across the peninsula agrees with the timing of regional Cenozoic volcanism, with stratigraphic constraints, and with thermochronometric measurements. Regional uplift appears to have been driven by a combination of convective upwelling and lithospheric thickness changes. We suggest that Arabia's eroding landscape contains useful quantitative information about the temporal and spatial evolution of regional uplift.

Appendix A: Drainage Inventory

Table A1 summarizes attributes of Arabian rivers, numbered anticlockwise from northwest quadrant (Figure 5). Latitude and longitude of river mouths/heads shown in decimal degrees. Maximum elevation, length, and area of drainage basins calculated from SRTM data set.

Table A1. Attributes of Arabian Rivers

River Mouth Name[a]	River Head Name	Number	Longitude[b] at Mouth	Latitude[b] at Mouth	Longitude[b] at Head	Latitude[b] at Head	Elevation[c] (m)	Length[d] (km)	Basin[e] (km^2)
Ceyhan Nehri	Ceyhan Nehri	1	36.054	38.244	35.341	36.608	1805	255	44,016
Ceyhan Nehri	Ceyhan Nehri	2	36.727	38.703	35.341	36.608	2150	485	44,016
Qarah Su Chay	Qarah Su Chay	3	36.717	37.206	35.964	36.046	745	185	46,506
Nahr as As	Nahr as As	4	37.640	36.624	35.964	36.046	556	411	46,506
Nahr as As	Nahr as As	5	37.483	34.786	35.964	36.046	869	402	46,506
Nahr as As	Nahr as As	6	36.281	34.020	35.964	36.046	1554	485	46,506
Nahr el Kebir	Nahr el Kebir	7	36.268	34.447	35.975	34.637	1663	92	1208
Nahr ak Litani	Nahr al Litani	8	36.385	34.012	35.246	33.337	2319	194	2342
Jordan River	Jordan River	9	36.542	33.854	35.033	32.810	1478	316	269,578
Jordan River	Jordan River	10	37.547	34.007	35.033	32.810	1080	458	269,578
Jordan River	Jordan River	11	38.416	33.138	35.033	32.810	795	487	269,578
Jordan River	Jordan River	12	39.274	32.222	35.033	32.810	926	627	269,578
Jordan River	Jordan River	13	38.523	31.248	35.033	32.810	893	636	269,578
Nahr az Zarga	Nahr az Zarga	14	39.626	31.051	35.033	32.810	850	758	269,578
Nahr az Zarga	Nahr az Zarga	15	40.468	30.123	35.033	32.810	702	865	269,578
Nahr az Zarga	Nahr az Zarga	16	39.774	28.490	35.033	32.810	938	967	269,578
Nahr az Zarga	Nahr az Zarga	17	39.905	26.897	35.033	32.810	1076	1172	269,578
Nahr az Zarga	Nahr az Zarga	18	39.088	26.192	35.033	32.810	1392	1359	269,578
Nahr az Zarga	Nahr az Zarga	19	38.482	26.966	35.033	32.810	1085	1195	269,578
Nahr az Zarga	Nahr az Zarga	20	37.622	28.084	35.033	32.810	1094	889	269,578
Nahr az Zarga	Nahr az Zarga	21	36.922	30.325	35.033	32.810	972	511	269,578
Wadi el Majib	Wadi el Majib	22	36.492	30.684	35.033	32.810	1020	373	269,578
Wadi el Girafi	Wadi el Girafi	23	34.496	29.605	35.033	32.810	942	529	269,578
Unnamed	Unnamed	24	35.346	32.105	34.772	32.100	641	85	1918
Wadi Ghazzah	Wadi Ghazzah	25	35.132	31.562	34.373	31.464	940	155	3884
Wadi Gohar	Wadi Gohar	26	34.619	30.347	33.809	31.146	732	224	25,380
Wadi Gera	Wadi Gera	27	33.953	29.064	33.809	31.146	1445	332	25,380
Wadi al Aghaydra	Wadi al Aghaydra	28	33.335	29.618	33.809	31.146	900	307	25,380
Unnamed	Unnamed	29	33.393	30.622	33.809	31.146	456	121	25,380

Table A1. (continued)

River Mouth Name[a]	River Head Name	Number	Longitude[b] at Mouth	Latitude[b] at Mouth	Longitude[b] at Head	Latitude[b] at Head	Elevation[c] (m)	Length[d] (km)	Basin[e] (km^2)
Unnamed	Unnamed	30	33.478	30.328	32.711	31.029	597	179	2273
Wadi Sudr	Wadi Sudr	31	33.183	29.729	32.691	29.613	661	77	648
Wadi Gharandal	Wadi Gharandal	32	33.424	29.238	32.904	29.223	1037	85	930
Wadi Seih	Wadi Seih	33	33.946	29.044	33.182	28.834	1331	119	1144
Unnamed	Unnamed	34	33.948	28.478	33.611	28.239	2147	63	2034
Wadi Kid	Wadi Kid	35	34.049	28.314	34.440	28.136	1308	70	1133
Wadi Dhahab	Wadi Dhahab	36	34.046	28.762	34.516	28.496	1309	92	2222
Wadi Watir	Wadi Watir	37	34.246	29.293	34.673	29.030	1214	117	3770
Unnamed	Unnamed	38	35.653	30.678	34.997	29.532	1492	334	60,390
Wadi ash Shawmari	Wadi ash Shawmari	39	36.665	30.477	34.997	29.532	932	283	60,390
Wadi Ratiya	Wadi Ratiya	40	37.092	29.109	34.997	29.532	1159	320	60,390
Wadi Saba	Wadi Saba	41	37.852	27.534	34.997	29.532	1012	484	60,390
Unnamed	Unnamed	42	36.474	27.790	34.997	29.532	1592	344	60,390
Wadi al Matakh	Wadi al Matakh	43	35.400	28.436	34.997	29.532	1332	351	60,390
Wadi Ifal	Wadi Ifal	44	35.384	28.573	35.040	28.106	1604	214	5252
Wadi Ash Sharmah	Wadi Ash Sharmah	45	36.379	27.801	35.207	28.022	1626	175	2044
Wadi Dama	Wadi Dama	46	36.738	27.377	35.801	27.123	1162	154	4569
Wadi Thalbah	Wadi Thalbah	47	37.192	26.757	36.186	26.667	1059	155	5341
Wadi al Hamd	Wadi al Hamd	48	37.193	26.471	36.706	26.013	1073	114	114,551
Wadi al Hamd	Wadi al Jizl	49	37.133	26.638	36.706	26.013	1174	501	114,551
Wadi al Hamd	Wadi al Jizl	50	36.760	27.533	36.706	26.013	1785	630	114,551
Wadi al Hamd	Wadi al Jizl	51	37.503	27.183	36.706	26.013	1553	544	114,551
Wadi al Hamd	Wadi al Ghamrah	52	38.936	26.294	36.706	26.013	1340	454	114,551
Wadi al Hamd	Wadi al' Lyaynah	53	39.491	26.477	36.706	26.013	1223	523	114,551
Wadi al Hamd	Wadi al' Lyaynah	54	39.947	25.823	36.706	26.013	1701	518	114,551
Wadi al Hamd	Wadi al' Lyaynah	55	39.994	25.494	36.706	26.013	1586	608	114,551
Wadi al Hamd	Wadi al Aqiq	56	40.055	25.477	36.706	26.013	1499	826	114,551
Wadi al Hamd	Wadi al Aqiq	57	41.341	24.663	36.706	26.013	1064	766	114,551
Wadi al Hamd	Wadi al Aqiq	58	41.553	24.494	36.706	26.013	1054	881	114,551
Wadi al Hamd	Wadi al Aqiq	59	42.233	23.545	36.706	26.013	1034	924	114,551
Wadi al Hamd	Wadi al Aqiq	60	41.321	23.270	36.706	26.013	1223	817	114,551
Wadi al Hamd	Wadi al Aqiq	61	40.120	23.596	36.706	26.013	1288	725	114,551
Wadi al Hamd	Wadi Malal	62	39.279	24.112	36.706	26.013	1109	539	114,551
Wadi al Hamd	Wadi al Ays	63	37.732	24.935	36.706	26.013	1097	409	114,551
Wadi Muraykhat	Wadi Muraykhat	64	37.730	25.351	37.171	25.250	794	85	914
Wadi Rashi	Wadi Rashi	65	38.610	24.928	38.187	23.978	888	202	6779
Unnamed	Unnamed	66	38.922	24.300	38.595	23.573	1169	164	2982
Wadi an Nahda	Wadi al Qaha	67	39.326	23.766	38.896	22.969	864	140	4919
Wadi Rabigh	Wadi Akhal	68	40.078	23.603	38.967	22.858	1326	226	5582
Wadi Rabigh	Wadi Rabigh	69	40.036	22.916	38.967	22.858	1493	188	5582
Wadi Arran	Wadi Murwani	70	40.083	22.791	39.078	22.252	1365	214	5537
Wadi Arran	Wadi Arran	71	40.220	22.265	39.078	22.252	1401	197	5537
Wadi Fatimah	Wadi Fatimah	72	40.301	21.308	39.172	21.194	1931	305	5824
Unnamed	Unnamed	73	40.408	21.048	39.746	20.384	1814	139	1825
Wadi ash Shagah al Yamaniyah	Wadi ash Shagah al Yamaniyah	74	41.131	20.402	40.718	19.791	1964	118	1664
Unnamed	Unnamed	75	41.831	19.845	41.069	19.142	1581	167	2471
Wadi Hali	Wadi Hali	76	42.370	18.315	41.330	18.584	2670	220	5518
Wadi Itwad	Wadi Itwad	77	42.491	18.189	42.133	17.604	1785	108	1762
Wadi Sabya	Wadi Sabya	78	42.728	17.989	42.456	17.048	1595	150	7692
Wadi Sabya	Wadi Sabya	79	43.175	18.032	42.456	17.048	2445	218	7692
Wadi Sabya	Wadi Sabya	80	43.343	17.309	42.456	17.048	2085	259	7692
Unnamed	Unnamed	81	43.432	16.706	42.740	16.503	1648	108	1501
Wadi Mawr	Wadi Mawr	82	43.532	16.931	42.779	15.822	2549	328	9134
Wadi Mawr	Wadi Mawr	83	43.934	16.426	42.779	15.822	1944	251	9134
Wadi Siham	Wadi Siham	84	43.978	15.257	42.967	14.687	3093	218	4946
Unnamed	Unnamed	85	44.443	14.427	43.108	14.080	2539	219	4903
Wadi Rasyan	Wadi Rasyan	86	44.039	13.849	43.280	13.573	1971	163	2116
Unnamed	Unnamed	87	43.808	13.095	43.894	12.649	753	66	274
Unnamed	Unnamed	88	44.137	13.299	45.084	12.916	1809	172	6479
Wadi Bana	Wadi Bana	89	44.265	14.157	45.387	13.064	2732	291	8193
Wadi Bana	Wadi Bana	90	44.787	14.332	45.387	13.064	2251	247	8193
Wadi Bana	Wadi Bana	91	45.409	14.124	45.387	13.064	1955	209	8193
Wadi Ahwar	Wadi Ahwar	92	46.257	14.108	46.682	13.426	1552	143	7613
Wadi Mayfa'ah	Wadi Mayfa'ah	93	46.828	14.259	47.806	13.933	1549	186	5647
Unnamed	Unnamed	94	47.183	15.024	48.696	14.050	1529	273	9858
Unnamed	Unnamed	95	47.948	14.959	48.696	14.050	1466	219	9858

Table A1. (continued)

River Mouth Name[a]	River Head Name	Number	Longitude[b] at Mouth	Latitude[b] at Mouth	Longitude[b] at Head	Latitude[b] at Head	Elevation[c] (m)	Length[d] (km)	Basin[e] (km^2)
Unnamed	Unnamed	96	48.591	14.833	48.696	14.050	1764	168	9858
Unnamed	Unnamed	97	49.306	15.185	49.631	14.760	1406	82	1179
Unnamed	Unnamed	98	49.930	15.344	50.284	14.918	1451	85	1393
Wadi Masilah	Wadi Masilah	99	49.899	15.335	51.131	15.184	1442	271	147,975
Wadi Masilah	Wadi Masilah	100	49.481	15.148	51.131	15.184	1755	439	147,975
Wadi Masilah	Wadi Masilah	101	48.739	14.959	51.131	15.184	1605	558	147,975
Wadi Masilah	Wadi Masilah	102	48.271	14.745	51.131	15.184	1809	628	147,975
Wadi Masilah	Wadi Masilah	103	47.266	14.773	51.131	15.184	1468	851	147,975
Wadi Masilah	Wadi Masilah	104	45.783	13.953	51.131	15.184	2281	1002	147,975
Wadi Masilah	Wadi Masilah	105	44.938	14.362	51.131	15.184	2096	1237	147,975
Wadi Masilah	Wadi Masilah	106	44.287	14.990	51.131	15.184	2701	1247	147,975
Wadi Masilah	Wadi Masilah	107	44.185	15.179	51.131	15.184	2643	1310	147,975
Wadi Masilah	Wadi Masilah	108	43.803	15.624	51.131	15.184	2961	1277	147,975
Wadi Masilah	Wadi Masilah	109	43.764	16.771	51.131	15.184	2043	1269	147,975
Wadi Masilah	Wadi Masilah	110	45.934	16.437	51.131	15.184	1058	919	147,975
Wadi Masilah	Wadi Masilah	111	47.264	16.323	51.131	15.184	1120	687	147,975
Wadi Masilah	Wadi Masilah	112	48.064	16.262	51.131	15.184	1072	534	147,975
Wadi Masilah	Wadi Masilah	113	49.071	16.560	51.131	15.184	961	430	147,975
Wadi Masilah	Wadi Masilah	114	50.070	16.648	51.131	15.184	1051	402	147,975
Wadi Masilah	Wadi Masilah	115	50.304	16.282	51.131	15.184	840	282	147,975
Unnamed	Unnamed	116	50.855	15.847	51.704	15.423	1079	166	3195
Wadi al Jiz	Wadi al Jiz	117	50.268	16.534	52.237	16.201	1030	300	19,195
Wadi al Jiz	Wadi Kidyut	118	51.622	17.061	52.237	16.201	959	297	19,195
Unnamed	Unnamed	119	52.564	16.694	52.836	16.565	1004	53	529
Unnamed	Unnamed	120	53.568	17.071	53.776	16.879	977	53	648
Unnamed	Unnamed	121	54.959	17.205	55.120	17.094	792	26	174
Wadi Ghadun	Wadi Ghadun	122	55.434	18.122	56.742	18.691	291	250	5823
Unnamed	Unnamed	123	55.953	18.973	56.939	18.816	200	218	10,117
Unnamed	Unnamed	124	57.356	19.573	57.343	18.928	179	94	969
Unnamed	Unnamed	125	56.621	19.776	57.994	20.432	157	362	30,286
Unnamed	Unnamed	126	57.321	22.339	57.994	20.432	392	409	30,286
Unnamed	Unnamed	127	57.575	23.153	58.215	20.610	2062	423	13,192
Unnamed	Unnamed	128	58.262	23.169	58.215	20.610	896	403	13,192
Wadi al Batha	Wadi al Batha	129	58.899	22.829	59.657	21.998	763	222	7166
Unnamed	Unnamed	130	59.220	22.511	59.486	22.598	1924	68	781
Unnamed	Unnamed	131	58.351	23.024	58.930	23.254	888	121	2177
Unnamed	Unnamed	132	57.889	23.076	58.178	23.686	781	107	1810
Unnamed	Unnamed	133	57.049	23.397	57.477	23.840	1030	119	815
Unnamed	Unnamed	134	56.309	23.861	56.839	24.241	922	104	926
Unnamed	Unnamed	135	56.004	24.774	56.450	24.804	537	64	594
Unnamed	Unnamed	136	56.311	25.955	55.966	25.781	1100	72	1683
Unnamed	Unnamed	137	56.161	25.086	55.736	25.647	587	108	2133
Unnamed	Unnamed	138	56.161	24.573	54.556	24.433	855	244	3346
Unnamed	Unnamed	139	56.330	23.997	54.010	24.120	926	334	20,435
Unnamed	Unnamed	140	53.480	23.329	52.686	24.144	148	187	2532
Unnamed	Unnamed	141	53.689	23.289	52.039	23.973	149	916	737,556
Unnamed	Unnamed	142	56.962	23.505	52.039	23.973	898	1782	737,556
Unnamed	Unnamed	143	57.195	23.245	52.039	23.973	1962	1377	737,556
Unnamed	Unnamed	144	56.739	21.361	52.039	23.973	125	1078	737,556
Unnamed	Unnamed	145	56.479	19.586	52.039	23.973	154	1267	737,556
Unnamed	Unnamed	146	55.761	18.804	52.039	23.973	225	1606	737,556
Unnamed	Unnamed	147	54.840	17.169	52.039	23.973	1527	1684	737,556
Unnamed	Unnamed	148	53.774	17.051	52.039	23.973	1126	1666	737,556
Unnamed	Unnamed	149	52.670	16.738	52.039	23.973	1210	1733	737,556
Unnamed	Unnamed	150	51.217	17.074	52.039	23.973	989	1824	737,556
Unnamed	Unnamed	151	49.306	16.547	52.039	23.973	1017	1538	737,556
Unnamed	Unnamed	152	47.731	16.080	52.039	23.973	1266	1704	737,556
Unnamed	Unnamed	153	47.238	16.380	52.039	23.973	1139	1722	737,556
Unnamed	Unnamed	154	44.531	16.496	52.039	23.973	2120	1810	737,556
Unnamed	Unnamed	155	43.432	17.677	52.039	23.973	2388	1965	737,556
Unnamed	Unnamed	156	45.176	18.958	52.039	23.973	1016	1244	737,556
Wadi Ghiran	Wadi ad Dawasir	157	44.164	18.191	51.821	23.993	1559	1518	460,530
Wadi Ghiran	Wadi Tathlith	158	43.414	17.799	51.821	23.993	2491	1800	460,530
Wadi Ghiran	Wadi Bishah	159	42.797	18.008	51.821	23.993	2422	2005	460,530
Wadi Ghiran	Wadi Subay	160	41.039	20.584	51.821	23.993	2094	2044	460,530
Wadi Ghiran	Wadi ad Dawasir	161	40.324	21.072	51.821	23.993	2222	2270	460,530
Wadi Ghiran	Wadi ad Dawasir	162	40.219	22.368	51.821	23.993	1393	2038	460,530

Table A1. (continued)

River Mouth Name[a]	River Head Name	Number	Longitude[b] at Mouth	Latitude[b] at Mouth	Longitude[b] at Head	Latitude[b] at Head	Elevation[c] (m)	Length[d] (km)	Basin[e] (km^2)
Wadi Ghiran	Wadi ad Dawasir	163	40.063	22.898	51.821	23.993	1485	2227	460,530
Wadi Ghiran	Wadi ad Dawasir	164	41.892	23.472	51.821	23.993	975	1854	460,530
Wadi Ghiran	Wadi ad Dawasir	165	43.596	22.755	51.821	23.993	1051	1731	460,530
Wadi Ghiran	Wadi ad Dawasir	166	44.213	21.882	51.821	23.993	1100	1419	460,530
Wadi Ghiran	Wadi Ghiran	167	45.704	21.758	51.821	23.993	965	1131	460,530
Wadi Ghiran	Wadi Ghiran	168	46.193	22.875	51.821	23.993	980	1088	460,530
Wadi Ghiran	Wadi Ghiran	169	47.434	23.648	51.821	23.993	583	993	460,530
Unnamed	Unnamed	170	43.948	22.041	51.712	24.211	1137	1305	143,160
Unnamed	Unnamed	171	42.980	23.917	51.712	24.211	1058	1396	143,160
Unnamed	Unnamed	172	44.413	23.980	51.712	24.211	1075	1313	143,160
Unnamed	Unnamed	173	44.531	24.329	51.712	24.211	986	1208	143,160
Unnamed	Unnamed	174	46.014	24.940	51.712	24.211	900	864	143,160
Unnamed	Unnamed	175	47.623	24.584	51.712	24.211	613	727	143,160
Unnamed	Unnamed	176	51.102	24.834	51.557	24.904	58	92	2204
Unnamed	Unnamed	177	51.234	25.222	50.826	25.466	47	63	1663
Unnamed	Unnamed	178	49.089	24.058	50.852	24.762	288	286	12,686
Unnamed	Unnamed	179	49.074	24.326	50.137	25.829	323	299	10,400
Unnamed	Unnamed	180	49.082	24.640	49.074	27.557	318	405	35,889
Unnamed	Unnamed	181	47.524	24.716	49.074	27.557	602	630	35,889
Unnamed	Unnamed	182	46.532	25.508	49.074	27.557	722	732	35,889
Unnamed	Unnamed	183	46.750	25.980	48.814	27.822	588	492	27,153
Unnamed	Unnamed	184	46.531	25.056	48.614	28.214	707	810	68,078
Unnamed	Unnamed	185	45.112	25.309	48.614	28.214	791	895	68,078
Unnamed	Unnamed	186	44.947	26.600	48.614	28.214	673	854	68,078
Unnamed	Unnamed	187	46.195	28.190	47.893	29.330	364	367	805
Karmat Khaykan	Wadi al Batin	188	45.080	25.902	48.691	30.013	801	1000	1,441,168
Karmat Khaykan	Wadi al Batin	189	43.916	23.976	48.691	30.013	991	1360	1,441,168
Karmat Khaykan	Wadi al Jarir	190	42.729	23.624	48.691	30.013	1008	1564	1,441,168
Karmat Khaykan	Wadi al Sahuq	191	40.747	25.329	48.691	30.013	1153	1535	1,441,168
Karmat Khaykan	Wadi ar Rummah	192	39.932	26.247	48.691	30.013	1395	1634	1,441,168
Karmat Khaykan	Wadi ar Rummah	193	40.654	26.836	48.691	30.013	1149	1576	1,441,168
Karmat Khaykan	Wadi al Batin	194	41.389	27.116	48.691	30.013	1241	1487	1,441,168
Karmat Khaykan	Wadi al Batin	195	39.831	26.284	48.691	30.013	1386	1795	1,441,168
Karmat Khaykan	Wadi al Batin	196	43.186	28.266	48.691	30.013	681	962	1,441,168
Karmat Khaykan	Karmat Khaykan	197	44.269	28.162	48.691	30.013	540	928	1,441,168
Karmat Khaykan	Karmat Khaykan	198	43.845	28.756	48.691	30.013	546	966	1,441,168
Karmat Khaykan	Euphrates	199	39.742	27.829	48.691	30.013	1016	1778	1,441,168
Karmat Khaykan	Wadi al Khirr	200	39.899	28.963	48.691	30.013	868	1465	1,441,168
Karmat Khaykan	Wadi al Ubayyid	201	40.211	30.493	48.691	30.013	784	1547	1,441,168
Karmat Khaykan	Euphrates	202	39.217	31.681	48.691	30.013	887	1594	1,441,168
Karmat Khaykan	Wadi Hawran	203	39.240	32.267	48.691	30.013	922	1673	1,441,168
Karmat Khaykan	Euphrates	204	39.176	32.408	48.691	30.013	896	1989	1,441,168
Karmat Khaykan	Euphrates	205	37.794	33.880	48.691	30.013	915	2020	1,441168
Karmat Khaykan	Euphrates	206	36.988	34.053	48.691	30.013	912	2010	1,441,168
Karmat Khaykan	Euphrates	207	37.793	35.319	48.691	30.013	547	1955	1,441,168
Karmat Khaykan	Euphrates	208	37.086	37.180	48.691	30.013	1108	2123	1,441,168
Karmat Khaykan	Euphrates	209	37.131	37.926	48.691	30.013	2223	2273	1,441,168
Karmat Khaykan	Ayvalitohma Cayi	210	36.875	39.102	48.691	30.013	1731	2653	1,441,168
Karmat Khaykan	Karasu	211	39.958	40.030	48.691	30.013	1982	2867	1,441,168
Karmat Khaykan	Perisuyu	212	41.242	39.563	48.691	30.013	2061	2853	1,441,168
Karmat Khaykan	Murat Nehri	213	43.104	39.985	48.691	30.013	2492	3135	1,441,168
Karmat Khaykan	Euphrates	214	38.849	37.452	48.691	30.013	829	1946	1,441,168
Karmat Khaykan	Nahr al Khabur	215	39.814	37.636	48.691	30.013	1632	2033	1,441,168
Karmat Khaykan	Wadi ath Tharthar	216	41.920	36.377	48.691	30.013	901	1345	1,441,168
Karmat Khaykan	Tigris	217	39.859	37.734	48.691	30.013	1694	1944	1,441,168
Karmat Khaykan	Bendimahi Cayi	218	44.203	39.109	48.691	30.013	2580	2069	1,441,168
Karmat Khaykan	Nahr az Zab al Kabir	219	44.488	38.342	48.691	30.013	2740	1799	1,441,168
Karmat Khaykan	Tigris	220	44.980	36.863	48.691	30.013	2605	1733	1,441,168
Karmat Khaykan	Nahr Diyala	221	46.528	35.702	48.691	30.013	2076	1206	1,441,168
Karmat Khaykan	Rudkhaeh-ye Karkheh	222	48.371	34.752	48.691	30.013	2562	1186	1,441,168
Karmat Khaykan	Rudkhaneh-ye Dez	223	49.464	33.800	48.691	30.013	2246	865	1,441,168
Karmat Khaykan	Rud-e Karun	224	51.903	31.308	48.691	30.013	2553	983	1,441,168
Karmat Khaykan	Rudkhaneh-ye Marun	225	51.119	30.798	48.691	30.013	2652	632	1,441,168

[a]Mouth of rivers marked "lake" do not drain into ocean directly but by interconnected lacustrine systems.
[b]Decimal degrees.
[c]Maximum elevation.
[d]Length from river head to coast.
[e]Drainage area calculated from SRTM data set.

Notation

z elevation of a river, L.
x distance along a river, L.
A upstream drainage area, L^2.
t time, T.
τ_G Landscape response time, T.
U Uplift rate, $L\,T^{-1}$.
E Erosion rate, $L\,T^{-1}$.
v advective coefficient of erosion, $L^{1-2m}\,T^{-1}$.
m area exponent, dimensionless.
n slope exponent, dimensionless.
κ diffusive coefficient of erosion, $L^2\,T^{-1}$.

Acknowledgments
JWPW was supported by Hess Corporation; GGR and MJH were supported by BP Exploration. We thank P. Bellingham, K. Czarnota, M. Falder, I. Frame, D. Lyness and D. McKenzie for their help. Figures were prepared using Inkscape and GMT4.2.0. Department of Earth Sciences contribution esc.309.

References

Abbate, E., M. L. Balestrieri, and G. Bigazzi (2002), Morphostructural development of the Eritrean rift flank (southern Red Sea) inferred from apatite fission track analysis, *J. Geophys. Res.*, *107*(B11), 2319, doi:10.1029/2001JB001009.
Abdulkader, M. A. (1979), Lower Jurassic Lateritic redbeds from central Arabia, *Sediment. Geol.*, *24*, 149–156.
Ahmed, A., C. Tiberi, S. Leroy, G. W. Stuart, D. Keir, J. Sholan, K. Khanbari, I. Al-Ganad, and C. Basuyay (2013), Crustal structure of the rifted volcanic margins and uplifted plateau of Western Yemen from receiver function analysis, *Geophys. J. Int.*, *193*, 1673–1690.
Al-Bassam, K. S. (2005), Mineralogy and geochemistry of the Hussainiyat karst bauxites and Zabira stratiform bauxite in northern Arabian Peninsula, *Iraqi Bull. Geol. Min.*, *1*(2), 15–44.
Al-Damegh, K., E. Sandoval and M. Brazangi (2005), Crustal structure of the Arabian plate: New constraints from the analysis of teleseismic receiver functions, *Earth Planet. Sci. Lett.*, *231*, 177–196.
Al-Hashmi, R. Gök, K. Al-Toubi, Y. Al-Shijbi, I. El-Hussain and A. J. Rodgers (2011), Seismic velocity structure at the southeastern margin of the Arabian Peninsula, *Geophys. J. Int.*, *186*, 782–792.
Al-Kwatil, M, A., P. Y. Gillot, H. Zeyen, A. Hildenbrand, and I. Al Gharib (2012), Volcano-tectonic evolution of the northern part of the Arabian plate in the light of new K-Ar ages and remote sensing: Harrat Ash Shaam volcanic province (Syria), *Tectonophysics*, *32*(580), 192–207.
Almazouri, M., M. N. Islam, H. Athar, P. D. Jones, and M. A. Rahman (2012), Recent climate change in the Arabian Peninsula: Annual rainfall and temperature analysis of Saudi Arabia for 1978–2009, *Int. J. Climatol.*, *32*, 953–966.
Almond, D. C. (1986), Geological evolution of the Afro-Arabian dome, *Tectonophysics*, *131*, 301–332.
Al-Qayim, B., J. Al-Sanabani, and A. K. Al-Subbary (2005), Paleoenvironmental implication of marine bioturbated horizons in the Majzir formation, Western Yemen, *Arabian J. Sci. Eng.*, *30*, 165–180.
Alsharhan, A. S., and S. J. Y. Nasir (1996), Sedimentological and geochemical interpretation of a transgressive sequence: The Late Cretaceous Qahlah Formation in the western Oman Mountains, United Arab Emirates, *Sediment. Geol.*, *101*, 227–242.
Al-Subbary, A. K., G. J. Nichols, D. W. J. Bosence, and M. Al-Kadasi (1998), Pre-rift doming, peneplanation or subsidence in the southern Red Sea? Evidence from the Medjzir Formation (Twailah Group) of western Yemen, in *Sedimentation and Tectonics in Rift Basins*, edited by B. H. Purser, and D. W. J. Bosence, pp. 119–133, Chapman and Hall, London, U. K.
Andrews, P., W. R. Hamilton, and P. J. Whybrow (1978), Dryopithecines from the Miocene of Saudi Arabia, *Nature*, *274*, 249–251, doi: 10.1038/274249a0.
Arno, V., et al. (1980), Recent volcanism along the Red Sea coast: The Al Birk lava field in Saudi Arabia, in *Geodynamic Evolution of the Afro-Arabian Rift System*, pp. 645–654, Accademia Nazionale dei Lincei, Consiglio nazionale delle ricerche (Italy), Rome.
Avni, Y., A. Segev, and H. Ginat (2012), Oligocene regional denudation of the northern Afar dome: Pre- and syn-breakup stages of the Afro-Arabian plate, *GSA Bull*, *124*(11/12), 1871–1879, doi:10.1130/B30634.1.
Babalola, L. O., M. Hussain, and M. H. Mustafa (2003), Origin of iron-rich beds in the basal Wajid sandstone, Abha–Khamis Mushayt area, southwest Saudi Arabia, *Arabian J. Sci. Eng.*, *28*, 3–24.
Bache, F., S. Leroy, C. Baurion, J. Robinet, C. Gorini, F. Lucazeau, P. Razin, E. d'Acremont, and K. Al-Toubi (2011), Post-rift uplift of the Dofar margin (Gulf of Aden), *Terra Nova*, *23*(1), 11–18.
Baker, J., L. Snee, and M. Menzies (1996), A brief Oligocene period of flood volcanism in Yemen: Implications for the duration and rate of continental flood volcanism at the Afro–Arabian triple junction, *Earth Planet. Sci. Lett.*, *138*, 39–55.
Barton, P. J., T. R. E. Owen, and R. S. White (1990), The deep structure of the east Oman continental margin: Preliminary results and interpretation, *Tectonophysics*, *173*, 319–331.
Becker, J. J. (2009), Global Bathymetry and elevation data at 30 arc seconds resolution: SRTM30_PLUS, *Mar. Geod.*, *32*(4), 355–371.
Behairy, A. K. A. (1983), Marine transgressions in the west coast of Saudi Arabia (Red Sea) between Mid-Pleistocene and present, *Mar. Geol.*, *52*, M25–M31.
Ben-Avraham, Z., A. Ginzburg, J. Makris, and L. Eppelbaum (2002), Crustal structure of the Levant Basin, eastern Mediterranean, *Tectonophysics*, *346*(4), 23–43.
Berlin, M. M., and R. S. Anderson (2007), Modeling of knickpoint retreat on the Roan Plateau, western Colorado, *J. Geophys. Res.*, *112*, F03S06, doi:10.1029/2006JF000553.
Bertrand, H., G. Chazot, J. Blickert-Toft, and S. Thoral (2003), Implications of widespread high-μ volcanism on the Arabian Plate for Afar mantle plume and lithospheric composition, *Chem. Geol.*, *198*, 47–61.
Bohannon, R. G. (1987), Tectonic configuration of the Western Arabian Continental Margin, Southern Red Sea, Kingdom of Saudi Arabia, *U.S. Geol. Surv. Open File Rep.*, *87*(512), 32 pp.
Bohannon, R. G., C. W. Naeser, D. L. Schmidt and R. A. Zimmermann (1989), The timing of uplift, volcanism and rifting peripheral to the Red Sea: A case for passive rifting, *J. Geophys. Res.*, *94*, 1683–1701.
Bosworth, W., and M. Taviani (1996), Late Quaternary reorientation of stress field and extension direction in the southern Gulf of Suez, Egypt: Evidence from uplifted coral terraces, mesoscopic fault arrays, and borehole breakouts, *Tectonics*, *15*(4), 791–802.

Brown, G. F. (1970), Margin of the Red Sea and the Coastal Structures in Saudi Arabia, *Philos. Trans. R. Soc. London A*, *267*, 75–87.
Brown, G. F. (1972), Tectonic map of the Arabian Peninsula, *Arabian Peninsula Map AP-2*, Saudi Arabian Dir. Gen. Miner. Resour., Jiddah, Saudi Arabia.
Brown, G. F., and R. O. Jackson (1960), The Arabian Shield, *Proc. Int. Geol. Congr.*, 21st, Sect. *9*, 69–77.
Brown, G. F., D. C. Schmidt, and C. Huffman (1989), Geology of the Arabian Peninsula Shield area of western Saudi Arabia, *U.S. Geol. Surv. Prof. Pap.*, *32*(560-A), 188 pp.
Buffler, R. T., J. H. Bruggemann, B. N. Ghebretensae, R. C. Walter, M. M. M. Guillaume, S. M. Berhe, W. McIntosh, and L. E. Park (2010), Geologic setting of the Abdur Archaeological site on the Red Sea coast of Eritrea Africa, *Global Planet. Change*, *72*, 429–450.
Burke, K. (1996), The African plate, *S. Afr. J. Geol.*, *56*(99), 339–410.
Burke, K., and Y. Gunnell (2008), The African Erosion Surface: A continental-scale synthesis of geomorphology, tectonics, and environmental change over the past 180 million years, *Mem. Geol. Soc. Am.*, *201*, 1–66.
Camp, V. E., and M. J. Roobol (1989), The Arabian continental alkali basalt province: Part I. Evolution of Harrat Rahat, Kingdom of Saudi Arabia, *Geol. Soc. Am. Bull.*, *56*(101), 71–95.
Camp, V. E., and M. J. Roobol (1992), Upwelling Asthenosphere Beneath Western Arabia and Its Regional Implications, *J. Geophys. Res.*, *97*, 15,255–15,271.
Camp, V. E., M. J. Roobol, and P. R. Hooper (1991), The Arabian continental basalt province: Part II. Evolution of Harrats Khaybar, Ithnayn, and Kura, Kingdom of Saudi Arabia, *Geol. Soc. Am. Bull.*, *103*, 363–391.
Camp, V. E., M. J. Roobol, and P. R. Hooper (1992), The Arabian continental basalt province: Part III. Evolution of Harrat Kishb, Kingdom of Saudi Arabia, *Geol. Soc. Am. Bull.*, *104*, 379–396.
Capaldi, G. P., G. Chiesa, G. Manetti, G. Orsi, and G. Poli (1987), Tertiary anorogenic granites of the western border of the Yemen Plateau, *Lithos*, *56*(20), 433–444.
Carbone, F., R. Matteucci, and A. Angelucci (1998), Present-day sedimentation on the carbonate platform of the Dhalak Islands, Eritrea, in *Sedimentation and Tectonics in Rift Basins*, pp. 523–536, Chapman and Hall, London, U. K.
Cerling, T. E., J. M. Harris, B. J. MacFadden, M. G. Leakey, J. Q. Quade, V. Eisenmann, and J. R. Ehleringer (1997), Global vegetation change through the Miocene/Pliocene boundary, *Nature*, *398*, 153–158.
Chang, S.-J., and S. Van der Lee (2011), Mantle plumes and associated flow beneath Arabia and East Africa, *Earth Planet. Sci. Lett.*, *302*, 448–454.
Chang, S-J., M. Merino, S. Van der Lee, S. Stein, and C. A. Stein (2011), Mantle flow beneath Arabia offset from the opening Red Sea, *Geophys. Res. Lett.*, *38*, L04301, doi:10.1029/2010GL045852.
Chapman, R. W. (1978), General information on the Arabian Peninsula: Geomorphology, in *Quaternary Period in Saudi Arabia*, vol. 1, edited by S. Al-Sayari, and J. G. Zötl, pp. 19–30, Springer, Vienna.
Chappell, J., and N. J. Shackleton (1986), Oxygen isotopes and sea level, *Nature*, *324*, 137–140.
Cheng, H., R. L. Edwards, W. S. Broecker, G. H. Denton, X. G. Kong, Y. J. Wang, R. Zhang, X. F. Wang (2009), Ice age terminations, *Science*, *326*, 248–252.
Chisea, S., L. Civetta, M. De Fino, L. La Volpe, and G. Orsi (1988), The Yemen trap series: Genesis and evolution of a continental flood basalt province, *J. Volcanol. Geotherm. Res.*, *56*(36), 337–350.
Civetta, L., M, De Fino, L. La Volpe, and L. Lirer (1978), K-Ar ages of the Yemen Plateau, *J. Volcanol. Geotherm. Res.*, *56*(4), 307–314.
Clemens, S. C., and W. L. Prell (2003), A 350,000 year summer-monsoon multi-proxy stack from the Owen Ridge, Northern Arabian Sea, *Mar. Geol.*, *201*, 35–51.
Coleman, R. G., R. T. Gregory, and G. F. Brown (1983), Cenozoic volcanic rocks of Saudi Arabia, *U.S. Geol. Surv. Open File Rep.*, *56*(03-93), 82 pp.
Collenette, P., and D. J. Grainger (1994), *Mineral Resources of Saudi Arabia Not Including Oil, Natural Gas, and Sulfur*, Directorate, Jiddah, Saudi Arabia.
Coulié, E., X. Quidelleur, P. -Y. Gillot, V. Courtillot, J. -C. Lefévre, and S. Chiesa (2003), Comparative K-Ar and Ar/Ar dating of Ethiopian and Yemenite Oligocene volcanism: Implications for timing and duration of the Ethiopian traps, *Earth. Planet. Sci. Lett.*, *56*(206), 477–492.
Craig, T. J., J. A. Jackson, K. Priestley, and D. McKenzie (2011), Earthquake distribution patterns in Africa: Their relationship to variations in lithospheric and geological structure, and their rheological implications, *Geophys. J. Int.*, (185), 403–434.
Crassard, R., et al. (2013), Middle Palaeolithic and Neolithic Occupations around Mundafan Palaeolake, Saudi Arabia: Implications for Climate Change and Human Dispersals, *PLoS ONE*, *8*(7), e69665, doi:10.1371/journal.pone.0069665.
Crosby, A. G., and K. Whipple (2006), Knickpoint initiation and distribution within fluvial networks: 236 waterfalls in the Waipaoa River, North Island, New Zealand, *Geomorphology*, *82*(1-2), 16–38.
Crosby, A. G., D. McKenzie, and J. G. Sclater (2006), The relationship between depth, age and gravity in the oceans, *Geophys. J. Int.*, *166*, 553–573.
Czarnota. K., G. G. Roberts, N. J. White and S. Fishwick (2013), Spatial and temporal patterns of Australian dynamic topography from River Profile Modeling, 119, 1384–1424, doi:10.1002/2013JB010436.
Dabbagh, A. E., K. G. Al-Hinai, and M. Asif Khan (1997), Detection of sand-covered geologic features in the Arabian Peninsula using SIR-C/X-SAR data, *Remote Sens. Environ.*, *59*, 375–382.
Dabbagh, A. E., K. G. Al-Hinai, and M. Asif Khan (1998), Evaluation of the Shuttle Imaging Radar (SIR-C/X-SAR) data for mapping paleodrainage systems in the Kingdom of Saudi Arabia, in *Quaternary Deserts and Climatic Change*, edited by A. S. Alsharhan, et al., pp. 483–493, Taylor & Francis, USA.
Dawood, Y. H., M. A. Aref, M. H. Mandurah, A. Hakami, and M. Gameil (2013), Isotope geochemistry of the Miocene and Quaternary carbonate rocks in Rabigh area, Red Sea coast, Saudi Arabia, *J. Asian Earth. Sci.*, *77*, 151–162.
Debayle, E., J. -J. Leveque, and M. Cara (2001), Seismic evidence for a deeply rooted low-velocity anomaly in the upper mantle beneath the northeast Afro/Arabian continent, *Earth Planet. Sci. Lett.*, *193*, 423–436, doi:10.1016/S0012-821X(01)00509-X.
Demenocal, P. B. (2004), African climate change and faunal evolution during the Pliocene-Pleistocene, southeast Turkey, *Earth Planet. Sci. Lett.*, *220*, 3–24, doi:10.1016/S0012-821X(04)00003-2.
Demir, T., A. Seyrek, R. Westaway, D. Bridgland, and A. Beck (2008), Late Cenozoic surface uplift revealed by incision by the River Euphrates at Birecik, southeast Turkey, *J. Quat. Int.*, *186*(1), 132–163, doi:10.1016/j.quaint.2007.08.010.
Divins, D. L. (2008), Total sediment thickness of the World's Oceans and Marginal Seas, Natl. Geophys. Data Cent., Boulder, Colo. [Available at http://www.ngdc.noaa.gov/mgg/sedthick.html.]
Drury, S. A., S. P. Kelly, S. M. Berhe, R. E. Ll. Collier, and M. Abraha (1994), Structures related to Red Sea evolution in northern Eritrea, *Tectonics*, *13*, 1371–1380.

du Bray, E. A., D. B Stoeser, and E. H. McKee (1991), Age and petrology of the tertiary as Sarat volcanic field, southwest Saudi Arabia, *Tectonophysics*, *198*(2-4), 155–180.
Dullo, W. C. (1990), Facies, fossil record and age of Pleistocene reefs from the Red Sea (Saudi Arabia), *Facies*, *22*(1), 1–45.
Dullo, W. C., and L. Montaggioni (1998), Modern Red Sea coral reefs: A review of their morpologies and zonation, in *Sedimentation and Tectonics in Rift Basins*, edited by B. H. Purser, and D. W. J. Bosence, pp. 583–594, Chapman and Hall, London, U. K.
Dziewonski, A. M., T.-A. Chou, and J. H. Woodland (1981), Determination of earthquake source parameters from waveform data for studies of global and regional seismicity, *J. Geophys. Res.*, *56*, 2825–2852.
Ebinger, C. J., N. H. Sleep (1998), Cenozoic magmatism throughout east Africa resulting from the impact of a single plume, *Nature*, *395*, 788–791.
Edgell, H. S. (2005), *Arabian Deserts: Nature, Origin and Evolution*, Springer, N. Y.
Egloff, F., R. Rhim, J. Makris, Y. A. Izzeldin, M. Bobsien, K. Meier, P. Junge, T. Noman, and W. Warsi (1991), Contrasting structural styles of the eastern and western margins of the southern Red Sea: The 1988 SONNE experiment, *Tectonophysics*, *198*, 329–353.
Ekström, G., M. Nettles, and A. M. Dziewonski (2012), The global CMT project 2004–2010: Centroid-moment tensors for 13,017 earthquakes, *Phys. Earth Planet. Inter.*, *200–201*, 1–9.
El Asmar, H. M. (1997), Quaternary isotope stratigrahpy and paleoclimate of coral reef terraces, Gulf of Aqaba, South Sinai, Egypt, *Quat. Sci. Rev.*, *16*, 911–924.
El Moursi, M., C. T. Hoang, I. F. El Fayoumy, O. Hegab, and H. Faure (1994), Pleistocene evolution of the Red Sea coastal plain, Egypt: Evidence from Uranium-series dating of emerged reef terraces, *Quat. Sci. Rev.*, *13*, 345–359.
Engdahl, E. R., R. D. Van de Hilst, and R. P. Buland (1998), Global teleseismic earthquake relocation with improved travel times and procedures for depth determination, *Bull. Seismol. Soc. Am.*, *88*, 722–743.
Farouk, S., and M. Faris (2012), Late Cretaceous calcareous nannofossil and planktonic foraminiferal bioevents of the shallow-marine carbonate platform in the Mitla Pass, west central Sinai, Egypt, *Cretaceous Res.*, *33*, 50–65.
Farr, T. G., et al. (2007), The Shuttle Radar Topographic Mission, *Rev. Geophys.*, *45*, RG2004, doi:10.1029/2005RG000183.
Feakins, S., and P. Demenocal (2008), Global and African regional climate during the Cenozoic, in *Cenozoic Mammals of Africa*, edited by L. Weredelin, and B. Sanders, pp. 45–55, Univ. of Calif. Press, USA.
Feinstein, S., M. Eyal, B. P. Kohn, M. S. Steckler, K. M. Ibrahim, B. K. Mod'd and Y. Tain (2013), Uplift and denudation history of the eastern Dead Sea rift flank, SW Jordan: Evidence from apatite fission track thermochronometry, *Tectonics*, *32*, 1513–1528, doi:10.1002/tect.20082.
Fishwick, S. (2010), Surface wave tomography: Imaging of the lithosphere-asthenosphere boundary beneath central and southern Africa?, *Lithos*, *12*(1–2), 63–73.
Fleitmann, D., S. J. Burns, M. Pekala, A. Mangini, A. Al-Subbary, M. Al-Aowah, J. Kramers, and A. Matter (2011), Holocene and Pleistocene pluvial periods in Yemen, southern Arabia, *Quat. Sci. Rev.*, *30*(7–8), 783–787.
Förste, C., et al. (2013), EIGEN-6C3stat—the newest High Resolution Global Combined Gravity Field Model based on the 4th Release of the GOCE Direct Approach. [Available at http://icgem.gfz-potsdam.de/ICGEM/documents/Foerste-et-al-EIGEN-6C3stat.pdf.]
Garfunkel, Z. (1988), Relation between continental rifting and uplifting evidence from the Suez rift and northern Red Sea, *Tectonophysics*, *150*, 33–49.
Garzanti, E., P. Vermeesch, S. Ando, G. Vezzoli, M. Valagussa, K. Allen, K. A. Kadi, and A. A. I. Al-Juboury (2013), Provenance and recycling of Arabian desert sand, *Earth Sci. Rev.*, *120*, 1–19.
Gettings, M. E. (1981), A heat flow profile across the Arabian Shield and Red Sea, *Eos. Trans. AGU*, *62*, 407.
Gettings, M. E., H. R. Blank, W. D. Mooney, and J. H. Healey (1986), Crustal structure of southwestern Saudi Arabia, *J. Geophys. Res.*, *91*, 6491–6521.
Glennie, K. W. (2010), Structural and stratigraphic evolution of Abu Dhabi in the context of Arabia, *Arabian J. Geosci.*, *3*, 331–349.
Goldberg, M., and F. Yaron (1978), The Th^{230}/U^{234} ages of raised Pleistocene marine terraces on the Island of Tiran and the southeast coast of Sinai with some tectonic implications, *Int. Cong. Sed.*, *1*(9–14), 258–259.
Gök, R., H. Mahdi, H. Al–Shukri, and A. J. Rodgers (2008), Crustal structure of Iraq from receiver functions and surface wave dispersion; implications for understanding the deformation history of the Arabian–Eurasian collision, *Geophys. J. Int.*, *172*, 1179–1187.
Gow, N. N., and G. P. Lozej (1993), Bauxite, *Geosci. Can.*, *20*(1), 9–16.
Ghebreab, W. (1998), Tectonics of the Red Sea region reassessed, *Earth Sci. Rev.*, *45*. 1–44.
Greenwood, W. R. (1973), The Ha'il arch—A key to the deformation of the Arabian Shield during evolution of the Red Sea rift, *Saudi Arabian Dir. Gen. Miner. Resour. Bull.*, *7*(5), 1–4.
Gvirtzman, G., J. Kronfeld, and B. Buchbinder (1992), Dated coral reefs of southern Sinai (Red Sea) and their implication to late Quaternary sea levels, *Mar. Geol.*, *108*, 29–37.
Hack, J. T. (1957), Studies of longitudinal stream profiles in Virginia and Maryland, *US. Geol. Surv. Prof. Pap.*, *294B*, 45–80.
Hadiouche, O, and W. Zurn (1992), Structure of the crust and upper mantle beneath the Afro-Arabian region from surface wave dispersion, *Tectonophysics*, *209*, 179–196, doi:10.1016/0040-1951(92)90022X.
Hadley, D. G., and R. J. Fleck (1980), Reconnaissance geologic map of Jabal Afaf quadrangle, *Geol. Map GM–33*, 10 p., sheet 20/40D, scale 1: 100,000, Saudi Arabian Dir. Gen of Miner. Resour., Jiddah, Saudi Arabia.
Hamilton, W. R., P. J. Whybrow, and H. A. McClure (1978), Fauna of fossil mammals from the Miocene of Saudi Arabia, *Nature*, *274*, 248–249, doi:10.1038/274248a0.
Hancock, G. R., C. Martinez, K. G. Evans, and D. R. Moliere (2006), A comparison of SRTM and high-resolution digital elevation models and their use in catchment geomorphology and hydrology: Australian examples, *Earth. Surf. Processes Landforms*, (31), 1394–1412.
Hansen, S., S. Schwartz, A. Al-Amri, and A. Rodgers (2007a), Combined plate motion and density-driven flow in the asthenosphere beneath Saudi Arabia: Evidence from shear-wave splitting and seismic anisotropy, *Geology*, *34*, 869–872, doi:10.1130/G22713.1.
Hansen, S., A. J. Rodgers S. Y. Schwartz, and A. M. S. Al-Amri (2007b), Imaging ruptured lithosphere beneath the Red Sea and Arabian Peninsula, *Earth Planet. Sci. Lett.*, *259*, 256–265.
Hartley, R. A., G. G. Roberts, N. White, and C. Richardson (2011), Transient convective uplift of an ancient buried landscape, *Nat. Geosci.*, *4*, 562–565. doi:10.1038/ngeo1191.
Henjes-Kunst, F., R. Altherr, and A. Baumann (1990), Evolution and composition of the lithospheric mantle underneath the western Arabian peninsula: Constraints from Sr-Nd isotope systematics of mantle xenoliths, *Contrib. Mineral. Petrol.*, *105*, 460–472.
Hoang, C. T., and M. Taviani (1991), Stratigraphic and tectonic implication of Uranium-series-dated coral reefs from uplifted Red Sea islands, *Quat. Res.*, *35*, 264–273.
Hoang, C. T., R. Dalongeville, and P. Sanlaville (1996), Stratigraphy, tectonics and palaeoclimatic implications of Uranuium-series dated coral reefs from the sudanese coast of the Red Sea, *Quat. Int.*, *31*, 47–51.

Holmes, A. (1944), *Principals of Physical Geology*, Thomas Nelson, Edinburgh, U. K.
Höltz, H., V. Maurin, and J. G. Zölt (1978), Geologic history of the Al Hasa area since the Pliocene, in *Quaternary Period in Saudi Arabia*, edited by S. S. Al-Sayari, and J. G. Zölt, pp. 230–239, Springer, Vienna, Austria.
Hoorn, C., and M. Cremaschi (2004), Late Holocene palaeoenvironmental history of Khawr Rawri and Khawr Al Balid (Dhofar, Sultanate of Oman), *Palaeogeogr. Palaeoclimatol. Palaeoecol.*, *213*, 1–36.
Hopson, C. A., R. G. Coleman, R. T. Gregory, J. S. Pallister, and E. H. Bailey (1981), Geologic section through the Samail Ophiolite and associated rocks along a Muscat–Ibra Transect, Southeastern Oman Mountains, *J. Geophys. Res.*, *86*, 2527–2544.
Hussain, A. G., and A. R. Bakor (1989), Petrography and palaeomagnetism of the basalts, southwest Harrat Rahat, Saudi Arabia, *Geophys. J. Int.*, *56*(99), 687–698.
Izzeldin, A. Y. (1987), Seismic, gravity and magnetic surveys in the central part of the Red Sea: Their interpretation and implications for the structure and evolution of the Red Sea, *Tectonophysics*, *143*(4), 269–306.
Kluyver, H. M., V. B. Bege, G. H. Smith, J. M. Ryder, M. Van Eck (1981), Sirhan-Turayf phosphate project: Results of work carried out under the phosphate agreement, *Tech. Record* RF-TR-01-05, 77 pp., Saudi Arabian Deputy Minist. for Miner. Resour., Saudi Arabia.
Kohn, B. P., and M. Eyal (1981), History of uplift of the crystalline basement of Sinai and its relation to opening of the Red Sea as revealed by fission track dating of apatites, *Earth. Planet. Sci. Lett.*, *52*, 129–141.
Kraus, M. J., and T. M. Brown (1986), Paleosols and time resolution in fluvial stratigraphy, in *Paleosols, Their Recognition and Interpretation*, edited by V. P. Weight, pp. 180–207, Blackwell, Oxford, U. K.
Krienitz, M.-S., K. M. Hasse, K. Mezger, P. van den Bogaard, V. Thiemann, and M. A. Shaikh-Mashail (2009), Tectonic events, continental intraplate volcanism, and mantle plume activity in northern Arabia: Constraints from geochemistry and Ar-Ar dating of Syrian lavas, *Geochem. Geophys. Geosyst.*, *10*, Q04008, doi:10.1029/2008GC002254.
Lambeck, K., and J. Chappell (2001), Sea level change through the last glacial cycle, *Science.*, *292*, 697–686.
Lambeck, K., A. Purcell, N. C. Flemming, C. Vita-Finzi, A. M. Alsharekh, and G. N. Bailey (2011), Sea level and shoreline reconstructions for the Red Sea: Isostatic and tectonic considerations and implications for hominid migration out of Africa, *Quat. Sci. Rev.*, *30*, 3542–3574.
Laughton, A. S., and C. Tramontini (1969), Recent studies of the crustal structure in the Gulf of Aden, *Tectonophysics*, *8*, 359–375.
Leroy, S., et al. (2010), Contrasted styles of rifting in the eastern Gulf of Aden: A combined wide-angle, multichannel seismic, and heat flow survey, *Geochem. Geophys. Geosyst.*, *11*, Q07004, doi:10.1029/2009GC002963.
Leroy, S., et al. (2012), From rifting to oceanic spreading in the Gulf of Aden: A synthesis, *Arabian J. Geosci.*, *5*, 859–901, doi:10.1007/s12517-011-0475-4.
Ligi, M., E. Bonatti, G. Bortoluzzi, A. Cipriani, L. Cocchi, F. C. Tontini, E. Carminati, L. Ottolini, A. Schettino (2012), Birth of an ocean in the Red Sea: Initial pangs, *Geochem. Geophys. Geosyst.*, *13*, Q08009, doi:10.1029/2012GC004155.
Lucazeau, F., et al. (2008), Persistent thermal activity at the Eastern Gulf of Aden after continental break-up, *Nat. Geosci.*, *1*, 854–858, doi:10.1038/ngeo359.
Madden, C. T., I. M. Naqvi, F. C. Whitmore, D. L. Schmidt and R. C. Wood (1980), Paleocene vertebrates from coastal deposits in Harrat Hadan area, at Taif region, Kingdom of Saudi Arabia, *U.S. Geol. Surv. Open File Rep., 80-0227*, 1–29.
Madden, C. T., F. C. Whitmore, D. L. Schmidt, and I. M. Naqvi (1995), The Umm Himar formation (Paleocene) of Saudi Arabia and associated strata: Stratigraphy, vertebrate fauna, and paleoenvironment, *U.S. Geol. Surv. Bull.*, *2093–A*.
Maley, J. (1996), The African rain forest—Main characteristics of changes in vegetation and climate from the Upper Cretaceous to the Quaternary, *Proc. R. Soc. Edinburgh*, *104B*, 31–73.
McClure, H. A., and C. Vita-Finzi (1982), Holocene shorelines and tectonic movements in eastern Saudi Arabia, *Tectonophysics*, *85*, T37–T43.
McGuire, A. V. (1988), Mantle xenoliths from Harrat al Kishb: The mantle beneath western Saudi Arabia, *J. Petrol.*, *29*, 73–92.
McGuire, A. V., and R. G. Bohannon (1989), Timing of mantle upwelling. Evidence for a passive margin for the Red Sea Rift, *J. Geophys. Res*, *94*, 1677–1682.
McKenzie, D. (1977), Surface deformation, gravity anomalies and convection, *Geophys. J. R. Astron. Soc.*, *48*, 211–238.
McKenzie, D. (1994), The Relationship between Topography and Gravity on Earth and Venus, *Icarus*, *112*(1), 55–88.
McKenzie, D. (2003), Estimating T_e in the presence of internal loads, *J. Geophys. Res.*, *109*(B9), 2348, doi:10.1029/2002JB001766.
McKenzie, D., and D. Fairhead (1997), Estimates of the elastic thickness of the continental lithosphere from Bouger and free air gravity anomalies, *J. Geophys. Res.*, *102*, 27,523–27,552.
McKenzie, D., and R. K. O'Nions (1991), Partial melt distribution from inversion of rare earth element concentrations, *J. Petrol.*, *32*, 1021–1091.
Menzies, M., G. Gallagher, A. Yelland, and A. J. Hurford (1997), Volcanic and nonvolcanic rifted margins of the Red Sea and Gulf of Aden: Crustal cooling and margin evolution in Yemen, *Geochim. Cosmochim. Acta*, (61), 2511–2527.
Milliman, J. D., and K. Farnsworth (2011), *River Discharge to the Coastal Ocean: A Global Synthesis*, Cambridge Univ. Press, Cambridge, U. K.
Moufti, M. R., A. M. Moghazi, and K. A. Ali (2013), $^{40}Ar/^{39}Ar$ geochronology of the Neogene-Quaternary Harrat Al-Madinah intercontinental volcanic field, Saudi Arabia: Implications for duration and migration of volcanic activity, *J. Asian Earth. Sci.*, *62*, 253–268.
Muller, R. D., M. Sdrolias, C. Gaina, and W. R. Roest (2008), Age, spreading rates, and spreading asymmetry of the world's ocean crust, *Geochem. Geophys. Geosyst.*, *9*, Q04006, doi:10.1029/2007GC001743.
Nasir, S. (1992), The lithosphere beneath the northwestern part of the Arabian plate (Jordan): Evidence from xenoliths and geophysics, *Tectonophysics*, *418*, 167–188.
Netzeband, G. L., K. Gohl, C. P. Hübscher, Z. Ben-Avraham, G. A. Dehghani, D. Gajewski, P. Liersch (2006), The Levantine basin–crustal structure and origin, *Tectonophysics*, *201*, 357–370.
Omar, G. I., and M. S. Steckler (1995), Fission track evidence on the initial rifting of the Red Sea: Two pulses, no propagation, *Science*, *270*, 1341–1344.
Pallister, J. S. (1987), Magmatic history of Red Sea rifting: Perspective from the central Saudi Arabian coastal plain, *Geol. Soc. Am. Bull.*, *98*, 400–417.
Parish, J. T., A. M. Ziegler, and C. R. Scotese (1982), Rainfall patterns and the distribution of coals and evaporites in the Mesozoic and Cenozoic, *Palaeogeogr. Palaeoclimatol. Palaeocol.*, *40*, 67–101.
Park, Y., A. A. Nyblade, A. J. Rodgers, and A. Al-Almri (2007), Upper mantle structure beneath the Arabian Peninsula and northern Red Sea from teleseismic body wave tomography: Implications for the origin of Cenozoic uplift and volcanism in the Arabian Shield, *Geochem. Geophys. Geosyst.*, *8*, Q06021, doi:10.1029/2006GC001566.
Pasyanos, M. E., and A. A. Nyblade (2007), A top to bottom lithospheric study of Africa and Arabia, *Tectonophysics*, *444*, 27–44, doi:10.1016/j.tecto.2007.07.008.
Paul, J. D. P., G. G. Roberts, and N. White (2014), The African landscape through space and time, *Tectonics*, *32*, 898–935, doi:10.1002/2013TC003479.

Pik, R., N. Bellahsen, S. Leroy, Y. Denéle, P. Razin, A. Ahmed, and K. Khanbari (2013), Structural control of basement denudation during rifting revealed by low-temperature (U-Th-Sm)/He thermochronology of the Socotra Island basement-Southern Gulf of Aden margin, *Geol. Soc. Am. Bull.*, *607*, 17–31.

Pirazzoli, P. A., J. L. Reyss, M. Fontugne, A. Haghipour, A. Hilgers, H. U. Kasper, H. Nazari, F. Preusser, and U. Radtke (2004), Quaternary coral-reef terraces from Kish and Qeshm Islands, Persian Gulf: New radiometric ages and tectonic implications, *Quat. Int.*, *120*, 15–27.

Plaziat, J. P., F. Baltzer, A. Choukri, O. Conchon, P. Freytet, F. Orszag-Sperber, B. Purser, A. Raguideau, and J. L. Reyss (1995), Quaternary changes in the Egyptian shoreline of the northwestern Red Sea and Gulf of Suez, *Quat. Int.*, *29/30*, 11–22.

Plaziat, J. P., J. L. Reyss, A. Choukri, and C. Cazala (2008), Diagenetic rejuvenation of raised coral reefs and precision of dating. The contribution of Red Sea reefs to the question of reliability of the Uranium-series datings of middle to late Pleistocene key reef-terraces of the world, *Notebooks Geol.*, *04*, 1–35.

Pollastro, R. M., A. S. Karshbaum, and R. J. Viger (1998), Maps showing geology, oil and gas fields and geologic provinces of the Arabian Peninsula, *U. S. Geol. Surv. Open File Rep.*, *97-470A*, 1–14.

Priestley, K., D. McKenzie, J. Barron, M. Tatar, and E. Debayle (2012), The Zagros core: Deformation of the continental lithospheric mantle, *Geochem. Geophys. Geosyst.*, *13*, Q11014, doi:10.1029/2012GC004435.

Pritchard, D., G. G. Roberts, N. J. White, and C. N. Richardson (2009), Uplift histories from river profiles, *Geophys. Res. Lett.*, *36*, L24301, doi:10.1029/2009GL040928.

Purser, B. H., and H. Höltz (1988), The sedimentary evolution of the Red Sea rift: A comparison of the northwest (Egyptian) and northeast (Saudi Arabian) margins, *Tectonophysics*, *153*, 193–208.

Quennell, A. M. (1959), The structure and geomorphic evolution of the Dead Sea rift, *Q. J. Geol. Soc. London*, *114*, 1–24, doi:10.1144/gsjgs.114.1.0001.

Ridley, A. P., and M. W. Seeley (1979), Evidence for recent coastal uplift near Al Jubail, Saudi Arabia, *Tectonophysics*, *52*, 319–327.

Riisager, P., K. B. Knight, J. A. Baker, I. U. Peate, M. Al–Kadasi, A. Al–Subbary, and P. R. Reeley (2005), Paleomagnetism and $^{40}Ar/^{39}Ar$ Geochronology of Yemeni Oligocene volcanics: Implications for timing and duration of Afro–Arabian traps and geometry of the Oligocene paleomagnetic field, *Earth Planet. Sci. Lett.*, *237*, 647–672.

Roberts, G., and N. White (2010), Estimating uplift rate histories from river profiles using African examples, *J. Geophys. Res.*, *115*, B02406, doi:10.1029/2009JB006692.

Roberts, G., J. D. Paul, N. White, and J. Winterbourne (2012a), Temporal and spatial evolution of dynamic support from river profiles: A framework for Madagascar, *Geochem. Geophys. Geosyst.*, *13*, Q04004, doi:10.1029/2012GC004040.

Roberts, G., N. White, G. L. Martin-Brandis, and A. G. Crosby (2012b), An uplift history of the Colorado Plateau and its surroundings from inverse modeling of longitudinal river profiles, *Tectonics*, *31*, TC4022, doi:10.1029/2012TC003107.

Roe, G., D. Montgomery, and B. Hallet (2002), Effects of orographic precipitation variations on the concavity of steady-state river profiles, *Geology*, *30*, 143–146.

Roger, J., J-P. Platel, C. Cavelier, and C. Bourdillon-De-Grissac (1989), New data on the stratigraphy and geological history of Dhofar (Sultanate of Oman), *Bull. Soc. Geol. Fr.*, *8*(2), 265–277.

Rosenbloom, N. A., and R. S. Anderson (1994), Hillslope and channel evolution in a marine terraced landscape, Santa Cruz, California, *J. Geophys. Res.*, *99*, 14,013–14,029.

Salpeteur, I., and H. Sebir (1989), Orientation studies for gold in the central pediplain of the Saudi Arabian shield, *J. Geochem. Exp.*, *34*, 189–215.

Sarnthein (1972), Sediments and history of the postglacial transgression in the Persian Gulf and northwest Gulf of Oman, *Mar. Geol.*, *12*, 245–266.

Schmidt, D. L., D. G. Hadley, and G. F. Brown (1983), Middle Tertiary continental rift and evolution of the Red Sea in southwestern Saudi Arabia, *U.S. Geol. Surv. Open File Rep*, 83–641, 1–60.

Schoenbohm, L. M., K. X. Whipple, B. C. Burchfiel, and L. Chen (2004), Geomorphic constraints on surface uplift, exhumation, and plateau growth in the Red River region, Yunnan Province, China, *Geol. Soc. Am. Bull.*, *116*(7–8), 895–909.

Schwarz, T., and K. Germann (1999), Weathering surfaces, laterite-derived sediments and associated mineral deposits in north-east Africa, *Spec. Publ. Int. Assoc. Sedimentol.*, *27*, 367–390.

Searle, M. P., A. G. Cherry, M. Y. Ali, and D. J. W. Cooper (2014), Tectonics of the Musandam Peninsula and northern Oman Mountains: From ophiolite obduction to continental collision, *GeoArabia*, *19*, 135–174.

Sebai, A., V. Zumbo, G. Feraud, H. Bertrand, A. G. Hussain, G. Giannerini, and R. Campredon (1991), $^{40}Ar/^{39}Ar$ dating of alkaline and tholeiitic magmatism of Saudi Arabia related to early Red Sea Rifting, *Earth. Planet. Sci. Lett.*, *104*, 473–487.

Şengör, A. M. (2001), Elevation as an indicator of mantle-plume activity, *Geol. Soc. Am. Spec. Pap.*, *352*, 183–225.

Sepulchre, P., G. Ramstein, F. Fluteau, M. Schuster, J-J. Tiercelin, and M. Brunet (2006), Tectonic uplift and eastern Africa aridification, *Science*, *313*, 1419–1423.

Shackleton, N. J., M. F. Sánchez-Goñi, D. Pallierm, and Y. Lancelot (2003), Marine isotope substage 5e and the Eemian interglacial, *Global Planet. Change*, *36*, 151–155.

Shaw, J. E., J. A. Baker, M. A. Menzies, M. F. Thirwall and K. M. Ibrahim (2003), Petrogenesis of the largest intraplate volcanic field on the Arabian Plate (Jordan): A mixed lithosphere–asthenosphere source activated by lithospheric extension, *J. Petrol.*, *44*, 1657–1679.

Sicilia, D., et al. (2008), Upper mantle structure of shear-waves velocities and stratification of anisotropy in the Afar hotspot region, *Tectonophysics*, *462*, 164–177, doi:10.1016/j.tecto.2008.02.016.

Sklar, L. S., and W. E. Dietrich (2001), Sediment and rock strength controls on river incision into bedrock, *Geology*, *29*(12), 1087–1090.

Smith, W. H. F., and P. Wessel (1990), Gridding with continuous curvature splines in tension, *Geophysics*, *55*, 293–305.

Steinberg, J., Z. Gvirtzman, Y. Folkman, and Z. Garfunkel (2011), Origin and nature of the rapid late Tertiary filling of the Levant Basin, *Geology*, *39*(4), 355–358, doi:10.1130/G31615.1.

Tabor, R. W., R. K. Mark, and R. H. Wilson (1985), Reproducibility of the K-Ar ages of rocks and minerals: An empirical approach, *U.S. Geol. Surv. Bull.*, *1654*, 5.

Tainton, K. M., and McKenzie (1994), The generation of kimberlites, lamproites and their source rocks, *J. Petrol.*, *35*, 787–817.

Taj, R. J. (2013), Microfacies, diagenesis and depositional environments of the Tertiary carbonates of Usfan Formation in Haddat As Sham area, Western Arabian Shield, Saudi Arabia, *Arabian J. Geosci.*, *6*, 1011–1031.

Tapley, B. (2005), GGM02—An improved Earth gravity field model from GRACE, *J. Geodyn.*, *79*(8), 467–478.

Tarboton, D. A. (1997), A new method for the determination of flow directions and upslope areas in grid digital elevation models, *Water Resour. Res.*, *32*, 309–319.

Tardy, Y., B. Kobilisek, and H. Paquet (1991), Mineralogical composition and geographical distribution of African and Brazilian periatlantic laterites. The influence of continental drift and tropical paleoclimates during the last 150 million years and implications for India and Australia, *J. Afr. Earth Sci.*, *12*, 283–295.

Thornber, C. R., and J. S. Pallister (1985), Mantle xenoliths from northern Saudi Arabia, *Eos Trans. AGU*, *66*, 393.

Tiberi, C., S. Leroy, E. d'Acremont, N. Bellahsen, C. Ebinger, A. Al–Lazik, and A. Pointu (2007), Crustal geometry of the northeastern Gulf of Aden passive margin: Localization of the deformation inferred from receiver function analysis, *Geophys. J. Int.*, *168*, 1247–1260.

Trifonov, V. G., et al. (2010), New data on the Late Cenozoic basaltic volcanism in Syria, applied to its origin, *J. Volcanol. Geotherm. Res.*, *85*, 173–210.

Tucker, G. E., and K. X. Whipple (2002), Topographic outcomes predicted by stream erosion models: Sensitivity analysis and intermodal comparison, *J. Geophys. Res.*, *107*(B9), 2179, doi:10.1029/2001JB000162.

Uchupi, E., S. A. Swift, and D. A. Ross (1999), Late Quaternary stratigraphy, paleoclimate and neotectonism of the Persian (Arabian) Gulf region, *Mar. Geol.*, *160*, 1–23.

Vita-Finzi, C. (2001), Neotectonics at the Arabian plate margins, *J. Struct. Geol.*, *23*, 521–530.

Walter, C. R., et al. (2000), Early human occupation of the Red Sea coast of Eritrea during the last interglacial, *Nature*, *405*, 65–69.

Watremez, L., S. Leroy, S. Rouzo. E. d'Acremont, P. Unternehr, C. Ebinger, F. Lucazeau, and A. Al-Lazki (2011), The crustal structure of the north-eastern Gulf of Aden continental margin: Insights from wide-angle seismic data, *Geophys. J. Int.*, *184*, 575–594, doi:10.1111/j.1365-246X.2010.04881.x.

Whipple, K. X., and G. E. Tucker (1999), Dynamics of the stream-power river incision model: Implications for height limits of mountain ranges, landscape response timescales, and research needs, *J. Geophys. Res.*, *104*, 17,661–17,674.

Whipple, K. X., and G. E. Tucker (2002), Implications of sediment-flux-dependent river incision models for landscape evolution, *J. Geophys. Res.*, *107*(B2), 2039, doi:10.1029/2000JB000044.

Whybrow, P. J. (1987), Miocene geology and palaeontology of Ad Dabtiyah, Saudi Arabia, *Bull. Br. Mus. Nat. Hist.*, *41*(4), 365–457.

Whybrow, P. J., and A. P. Hill (1999), *Fossil Vertebrates of Arabia, With Emphasis on the Late Miocene Faunas, Geology, and Palaeoenvironments of the Emirate of Abu Dhabi, United Arab Emirates*, Yale Univ. Press, New Haven, Conn.

Whybrow, P. J., and H. A. McClure (1981), Fossil mangrove roots and palaeoenvironments of the Miocene of the eastern Arabian Peninsula, *Palaeogeogr. Palaeoclimatol. Palaeoecol*, *32*, 213–225.

Winterbourne, J., A. G. Crosby, and N. White (2009), Depth, age and dynamic topography of oceanic lithosphere beneath heavily sedimented Atlantic margins, *Earth Planet. Sci. Lett.*, *287*, 137–151.

Winterbourne, J., N. White and A. G. Crosby (2014), Accurate measurements of residual topography from the oceanic realm, *Tectonics*, *33*, 982–1015, doi:10.1002/2013TC003372.

Wood, W. W., R. M. Bailey, B. A. Hampton, T. F. Kraemer, Z. Lu, D. W. Clark, R. H. R. James, and K. Al Ramadan (2012), Rapid late Pleistocene/Holocene uplift and coastal evolution of the southern Arabian (Persian) Gulf, *Quat. Res.*, *77*, 215–220.

Wright, V. P. (1994), Losses and gains in weathering profiles and duripans, in *Quantitative Diagenesis: Recent Developments and Applications to Reservoir Geology*, edited by A. Parker and B. W. Sellwood, pp. 95–123, Kluwer Acad., Dordrecht, Netherlands.

Wu, S., R. Bras, and A. Barros (2006), Sensitivity of channel profiles to precipitation properties in mountain ranges, *J. Geophys. Res.*, *111*, F01024, doi:10.1029/2004JF000164.

Zhu, L., K. H. Wyrwoll, L. B. Collins, J. H. Chen, G. J. Wasserburg, and A. Eisenhauer (1993), High-precision U-series dating of Last Interglacial events by mass spectrometry: Houtman Abrolhos Islands, western Australia, *Earth Planet. Sci. Lett.*, *118*, 281–293.

Zilberman, E., and R. Calvo (2013), Remnants of Miocene fluvial sediments in the Negev Desert, Israel, and the Jordanian Plateau: Evidence for an extensive subsiding basin in the northwest margins of the Arabian plate, *J. Afr. Earth Sci.*, *82*, 33–53.

Zor, E., E. Sandvol, C. Gürbüz, N. Türkelli, D. Seber, and M. Barazangi (2003), The crustal structure of the East Anatolian plateau (Turkey) from receiver functions, *Geophys. Res. Lett.*, *30*(24), 8044, doi:10.1029/2003GL018192.